Suitability of microcrystalline cellulose as an ion exchanger

A radiochemical approach to the determination of ion exchange properties of AaltoCell™ materials

Master's thesis
Jenna Järvenpää
Radiochemistry
Department of Chemistry
University of Helsinki
December 2019

HELSINGIN YLIOPISTO
HELSINGFORS UNIVERSITET
UNIVERSITY OF HELSINKI
MATEMAATTIS-LUONNONTIETEELLINEN TIEDEKUNTA
MATEMATISK-NATURVETENSKAPLIGA FAKULTETEN
FACULTY OF SCIENCE

Tiedekunta – Fakultet – Faculty	Koulutusohjelma – Utbildningsprogram – Degree programme
Faculty of Science	Degree Programme in Chemistry

Tekijä – Författare – Author
Jenna Jade-Pepita Järvenpää

Työn nimi – Arbetets titel – Title
Suitability of microcrystalline cellulose as an ion exchanger; a radiochemical approach to the determination of ion exchange properties of AaltoCell^{TM}-materials

Työn laji – Arbetets art – Level	Aika – Datum – Month and year	Sivumäärä – Sidoantal – Number of pages
Master's thesis	12/2019	8 + 111 + 36

Tiivistelmä – Referat – Abstract

The suitability of AaltoCell^{TM} materials as ion exchangers to the purification of radioactive waste waters is researched through structural studies and batch sorption experiments. The aim of these experiments is to determine if AaltoCell^{TM} materials are suitable for sorption of ^{57}Co, ^{85}Sr and ^{134}Cs in $NaNO_3$ (aq), $NaClO_4$ (aq) or phosphate buffer solutions. Three different AaltoCell^{TM} materials are produced from bleached sulfate (MCC1), unbleached oxygen delignified (MCC2) and unbleached pulps (MCC3) given by a Finnish kraft pulp mill. Their morphology, specific surface area, particle size and molecular distributions, carbohydrate and lignin content as well as surface lignin coverage are measured. The batch sorption experiments are focused on kinetics, sorption as a function of pH and ionic strength and the electrolyte exclusion by the Donnan potential.

The experimental work revealed the order of the lignin content, MCC2 > MCC3 > MCC1, and the sorption order for ^{57}Co, MCC3 > MCC2 > MCC1. MCC2 had the highest total lignin, surface lignin coverage and the BET surface area of the AaltoCell^{TM} materials. MCC1 had the widest size range of particles and the lowest lignin contents, whereas MCC3 had the narrowest particle size distribution. The batch sorption experiments indicated the AaltoCell^{TM} materials, except MCC1, to be suitable for sorption of ^{57}Co in phosphate buffer solutions at pH ~ 7. Also, MCC2 was noticed to be suitable in solutions with inert electrolytes and low ionic strength, such as 0,01 M $NaClO_4$ (aq) at pH ~ 4,7 or in active electrolytes and high ionic strength, such as 1 M $NaNO_3$ (aq) at pH ~ 6,5. The sorption of ^{57}Co was discovered to be dependent on the solution, swelling and experiment method used. No sorption of ^{57}Co was detected in 10 mM $NaNO_3$ (aq) at any pH level tested, 0,1–1 M $NaClO_4$ (aq) at pH ~ 4,6 and 0,1 M $NaNO_3$ (aq) at pH ~ 4,8–4,9. On the other hand, MCC2 was found to be suitable for sorption of ^{85}Sr in 10 mM $NaNO_3$ (aq) at pH range of 1–9 and not consistently suitable for sorption of ^{134}Cs in 10 mM $NaNO_3$ (aq) at the same pH range due to the divergent results of two batch sorption experiments.

The performed experiments indicated that the AaltoCell^{TM} materials, except MCC1, could have a significant sorption of ^{57}Co in phosphate buffer solutions, especially in those without disturbing K^+ ions. Moreover, MCC2 was found to act as a pure cation exchanger with ^{85}Sr in 10 mM $NaNO_3$ (aq). Since the results were promising, the AaltoCell^{TM} materials containing lignin may be seen as inexpensive, non-toxic and environmentally friendly bases for chemical modifications to achieve better ion exchangers in the nuclear industry and to reduce the volume and the costs of their final disposal.

Avainsanat – Nyckelord – Keywords
ion exchanger, microcrystalline cellulose, AaltoCell^{TM} materials, lignin, cobalt, strontium, cesium

Säilytyspaikka – Förvaringställe – Where deposited
Kumpula Campus Library, the Helsinki University Archives, E-thesis service

Muita tietoja – Övriga uppgifter – Additional information

Acknowledgments

I would first like to thank my thesis advisors, Dr. Risto Koivula of the Department of Chemistry at the University of Helsinki and Dr. Kari Vanhatalo of the Department of Bioproducts and Biosystems at Aalto University for guiding my work through comprehensive experiments in two different laboratories.

I would also like to thank Prof. (Emeritus) Jukka Lehto of the Department of Chemistry at the University of Helsinki and Prof. Olli Dahl of the Department of Bioproducts and Biosystems at Aalto University for supporting my work and providing innovative aspects to it during the process. Moreover, I would like to thank Prof. Gareth Law of the Department of Chemistry at the University of Helsinki for examining my thesis thoroughly.

In addition, I would like to gratefully acknowledge the contributions of personnel of these departments as well as the talented scientists of research groups, Ion Exchange and Clean Technologies, who assisted me during my experiments. Also, I would like to specially thank Sr. Engineer Kerttuli Helariutta for boosting my writing process even during our hobbies.

Finally, I must express my profound gratitude to my family, especially to Heikki Hyyti, for encouraging me through the whole research and writing process. Thank you for always being there for me.

In addition, I will thank Microsoft Word for giving me experience to reconsider this product again when doing my next thesis.

Author

Jenna Järvenpää

Contents

List of tables

List of pictures

List of abbreviations

PWR	Pressurized water reactor
BWR	Boiling water reactor
NPP	Nuclear power plant
DVB	Divinylbenzene
EC	Electron capture
GMA	Glycidyl methacrylate
CM	Carboxymethyl
DEAE	Diethylaminoethyl
MCC	Microcrystalline cellulose
HCl	Hydrochloric acid
H_2SO_4	Sulfuric acid
CED	Cupriethylenediamine
DP	Degree of polymerization
BET	Brunauer, Emmet, Teller
SEM	Scanning electron microscopy
FEG	Field emission gun
SED	Secondary electron detector
ETSE	Everhart-Thornley secondary electron detector
BSE	Backscattered electron detector
VPSE	Variable pressure secondary electron detector
STEM	Scanning transmission electron microscopy
EDS	Energy dispersive x-ray spectrometry detector
EPMA	Electron probe micro-analyzer
CRT	Cathode ray tube
SEC	Size-exclusion chromatography
GFC	Gel filtration chromatography
GPC	Gel permeation chromatography
MALLS	Multi-angle laser light scattering
RALS	Right-angle light scattering
LALS	Low-angle light scattering
DMAc	N,N-dimethylacetamide
LiCl	Lithium chloride

THF	Tetrahydrofuran
MMD	Molar mass distribution
HPLC	High performance liquid chromatography
RE	Reversed phase chromatography
HIC	Hydrophilic interaction chromatography
HPAEC	High performance anion exchange chromatography
PAD	Pulsed amperometric detection
TAP	Tomographic atom probe
SIMS	Secondary ion mass spectrometry
SERS	Surface-enhanced Raman spectrometry
EDX	Energy-dispersive x-ray analysis
TXRF	Total reflection x-ray fluorescence
UPS	Ultraviolet photoelectron spectroscopy
AES	Auger electron spectroscopy
XPS	X-ray photoelectron spectroscopy
NaI(Tl)	Sodium iodide doped with thallium
PM	Photomultiplier
BF	Batch factor (ml/g)
NaOH	Sodium hydroxide
$(CH_3)_3COH$	Tert-butanol
$NaNO_3$	Sodium nitrate
$NaClO_4$	Sodium perchlorate
KH_2PO_4	Monopotassium phosphate
$Na_2HPO_4*H_2O$	Sodium phosphate dibasic hydrate
HNO_3	Nitric acid
H_3PO_4	Phosphoric acid
Klason	Insoluble lignin
ASL	Acid-soluble lignin
CH	Carbohydrate
$H_2PO_4^-$	Dihydrogen phosphate
HPO_4^{2-}	Hydrogen phosphate
FTIR	Fourier transform infrared spectrometer
XRD	X-ray diffraction

1 Introduction

Ion exchangers are an essential part of separation and purification treatments of radioactive waste waters in nuclear industry, as stated in Lehto (2000). They mainly consist of synthetic organic or inorganic ion exchangers, such as cross-linked polystyrene sulfonic acid, zeolites or sodium titanate (p. 3509, 3514). However, there are some challenges that arise from their usage, such as environmental discharges of radioactivity, final waste volumes and waste disposal costs (p. 3512). The disposal of spent ion exchangers can be done through immobilization, advanced oxidation processes, super-compaction, acid stripping, microbial conversion and using high integrity container as mentioned in Wang and Wan (2015).

On the other hand, cellulose provides an eco-friendly, inexpensive and easily available material for bio-adsorbents in wastewater treatments (Hokkanen, Bhatnagar, & Sillanpää, 2016). It can be chemically modified in various ways to improve its adsorption capacity for aquatic pollutants, such as metal ions. Thus, it could be used in, e.g., separation of uranium (Fischer & Lieser, 1993), purification of low-level radioactive waste (Othman, Sohsah, & Ghoneim, 2009) and recovering heavy metals (Grubhofer, 1991). Moreover, cellulose-based adsorbents could be disposed by, e.g., incineration, pyrolysis, wet oxidation and microbial conversion to reduce volume, weight and costs of final waste disposal if used as ion exchangers in nuclear industry (Wang & Wan, 2015).

Since no mention of cellulose-based ion exchangers was found from literature related to their use in nuclear industry, it was decided to study the ion exchange properties of novel AaltoCell^{TM} materials based on microcrystalline celluloses. Due to the potential of lignin-based adsorbents to replace commercial ion exchange resins (Liang, Song, Huang, Li, & Chen, 2013), two out of three AaltoCell^{TM} materials are made to contain lignin by choosing unbleached kraft and oxygen delignified pulp as starting materials.

The main objective of this work is to define the suitability of the AaltoCell^{TM} materials as ion exchangers in the purification of radioactive waste waters produced at nuclear power plants (NPPs). Since the objective is wide and requires profound and extensive understanding of the AaltoCell^{TM} materials regarding functional groups, morphology and ion exchange properties, it was decided to focus on the structural properties and sorption behavior of the AaltoCell^{TM} materials with the most important radionuclides, ^{137}Cs, ^{90}Sr and ^{60}Co, in $NaNO_3$ (aq), $NaClO_4$ (aq) and phosphate buffer solutions. These solutions were chosen because they

were used in the previous works, e.g., $NaNO_3$ (aq) in Lehto (2000, p. 3514), $NaClO_4$ (aq) in Virtanen et al., (2018) and phosphate buffer solution in Teshirogi and Ohtomo (1986). Specifically, the following research questions are studied with less hazardous radionuclides:

Q1: Are AaltoCell^{TM} materials suitable for sorption of ^{57}Co?

Q2: Are AaltoCell^{TM} materials suitable for sorption of ^{85}Sr?

Q3: Are AaltoCell^{TM} materials suitable for sorption of ^{134}Cs?

This work aims to answer to these questions and provide more detailed information on the circumstances where sorption for each selected radionuclide is significant and what are the phenomena affecting sorption in each experiment and AaltoCell^{TM} material.

The proceeding sections of the work are organized as follows. After a short review of ion exchangers, radionuclides and microcrystalline cellulose in the perspective of nuclear industry in Section 2, the analysis techniques used in the experiments are presented in Section 3. In Section 4 the experimental work conducted in two laboratories is described in detail. The results and discussion are presented in Section 5, where research questions Q1–Q3 are answered and analyzed in depth. Section 6 includes the conclusions of the work. Additional data on experimental results, determination of uncertainties and original results are presented in Appendices.

2 Background

According to Luca (2000, pp. 1617-1618), ion exchangers are based on solid, insoluble materials of which functional groups ionize and exchange counter-ions within aqueous media. This phenomenon called sorption has been utilized in wide technical applications, such as in purifying acid mine water from mining and mineral industry (Feng, Aldrich, & Tan, 2000), removing antibiotics from surface water (Adams, Asce, Wang, Loftin, & Meyer, 2002) and controlling the primary coolant water chemistry in nuclear industry (Lehto, 2000, p. 3509). Besides treating the primary coolant water in nuclear power plants, ion exchangers have other significant functions in nuclear industry, e.g., the removal of uranium from ore leach liquors and the solidification of low- and medium-active nuclear waste solutions. However, the main function of these ion exchangers is to remove aqueous radioactive fission and activation products, the most important of which are ^{137}Cs, ^{90}Sr and ^{60}Co (Lehto, 2000, p. 3511).

The variety of different ion exchangers ranges from organic to inorganic, from which organic ion exchangers can be further divided into chemically modified and synthetic ion exchangers as mentioned in Hokkanen et al. (2016) and Luca (2000, p. 1619). The insufficient studies on organic lignin-based materials as ion exchangers and their possible future replacements for existing resins (Demirbas, 2004) supported further investigations on these materials. Thus, the sorption of the most important fission and activation products on newly invented organic AaltoCell^{TM} materials were studied with less hazardous isotopes, ^{134}Cs, ^{85}Sr and ^{57}Co, to identify the suitability of microcrystalline cellulose as an ion exchanger with and without lignin.

2.1 Ion exchangers in nuclear industry

Nuclear industry uses ion exchange resins in multiple phases of the open and closed nuclear fuel cycles as stated in Lehto (2000). These phases include uranium ore treatment as well as ion exchange processes both at operating nuclear power plants (NPP) and at nuclear fuel reprocessing plants. Their major applications of ion exchange are separation of anionic complexes of uranium from leach liquor by strong basic anion exchange resins in the uranium ore treatment, purification of primary coolant water, condensate and spent fuel storage pond water at NPP and both secondary waste effluent treatment and separation streams at nuclear fuel reprocessing plants (pp. 3509-3514).

According to Lehto (2000, p. 3511) the use of other main applications such as control of primary coolant water chemistry, production of make-up water and treatment of waste solutions depends on the reactor type of the nuclear power plant. For example, the control of primary coolant chemistry is typical to some pressurized water reactors (PWR), but not for boiling water reactors (BWR) as mentioned in Teollisuuden Voima (TVO) (2013, p. 40). Mabrouk et. al. (2012) states that the applications of ion exchangers in nuclear power plants contribute to many aspects of NPP operation such as controlling feed system fouling, keeping material performance and reducing personnel radiation exposures as also mentioned in Neeb (1997, p. 341). Besides the mentioned applications, ion exchangers can be utilized in decontamination of military waste effluents originated from various nuclear weapons programmes (Lehto, 2000, p. 3515).

Ion exchange materials used in the nuclear industry can be divided into organic and inorganic ion exchangers depending on their structure. Organic ion exchangers are commonly prepared from cross-linking polystyrene with divinylbenzene (DVB) and adding either a sulfonic acid group or a quaternary ammonium ion to the benzene ring to form strong cation or anion exchanger (Lehto & Hou, 2011, pp. 64-65). With nuclear grade properties such as high purity and high levels of suitable ionic form as well as uniform particle size, they are mainly used as deep beds and as pre-coat filters in removing ionic and particulate contaminants from radioactive waters such as the primary circuit water, condensate and fuel storage pond water as stated in Lehto (2000, pp. 3509-3510).

On the other hand, inorganic ion exchangers can be produced from a wide selection of inorganic materials such as zeolites, sodium titanate and hexacyanoferrate to achieve superior selectivities to certain radionuclides compared to organic ion exchangers (Lehto, 2000, p. 3510, 3514). Moreover, they provide high resistance to radiation and to high temperatures as well as potential applications in nuclear industry through the development of their chemical stability and suitability for use in packed bed columns. Thus, inorganic ion exchangers have been used in different nuclear waste management processes such as in removal of specific radionuclides from reprocessing waste effluents, military waste effluents and spent fuel pond waters (pp. 3514-3515). They can also be used in the preconcentration of radionuclides from high water volumes as mentioned in Lehto and Hou (2011, p. 65).

By contrast, there are other methods used for purification of radioactive waste waters such as chemical precipitation, sedimentation, thermal evaporation and membrane permeation (Zakrzewska-Trznadel, Harasimowicz, & Chmielewski, 2001). Especially, simple, economical and environmentally friendly membrane processes based on reverse osmosis have already been utilized in nuclear power plants for cleaning up, e.g., laundry and laboratory wastes as well as boric acid solutions. These membranes are produced from a mixture of cellulose acetate polyamide and polyether amid polysulphone.

Other radioactive water treatment applications of cellulose are, e.g., a cloth filter incorporated with amidoxime/carboxyl groups for recovering of uranium from low concentrations (Badawy, Sokker, Othman, & Hashem, 2005), oxidized and mechanically treated ultrafine cellulose nanofibers to separate hexavalent uranyl ions from aqueous solutions (Ma, Hsiao, & Chu, 2011) and a highly hydrophilic water-insoluble nanofiber composite for rapid adsorption of Cs from radioactive waste waters (Bang, H. et al., 2014).

However, cellulose-based adsorbents are mainly used in non-radioactive conditions such as in removal of heavy metals from waste waters (O'Connell, Birkinshaw, & O'Dwyer, 2008), in purification of wastewater from dyeing and metalization (Wegscheider, Knapp, & Leyden, 1981) and in other water and wastewater treatments against different pollutants such as inorganic anions, organic compounds and micropollutants (Hokkanen et al., 2016).

In conclusion, nuclear industry has various use of ion exchange resins from uranium ore treatment, water purification processes in NPP to military waste effluents as well as to ensuring personnel safety, to controlling water chemistry and to maintaining material performance. These ion exchange processes are mainly conducted by synthetic organic ion exchange resins, although inorganic ion exchangers have proven to be useful for their superior selectivity. However, according to the present state of literature related to nuclear industry, cellulose-based applications are still lacking in the ion exchange processes of radioactive waste waters.

2.2 Relevant radionuclides in nuclear power plants

In this research the focus is on the three most important radionuclides, ^{137}Cs, ^{90}Sr and ^{60}Co, which represent the fission and activation products of the nuclear fuel and the activated corrosion products of the primary circuit materials as stated in Neeb (1997, pp. 163-164). These radionuclides are studied through less radioactively hazardous isotopes, ^{134}Cs, ^{85}Sr and ^{57}Co. From the viewpoint of ion exchange, ^{60}Co represents the major cause of the contamination buildup on the primary circuit surfaces as argued in Neeb (1997, p. 264), whereas the significance of ^{137}Cs and ^{90}Sr increases over time in radioactive waste waters due to the decay of short-lived radionuclides (Marinin & Brown, 2000). The formations of these radionuclides in the primary circuit of a nuclear power plant are discussed below, after which each element and its major radioactive isotopes are described in detail.

During normal operation of NPP the radionuclides present in the coolant can be divided into three categories by their formation media: to activation products of the coolant, to both fission and activation products of the nuclear fuel and to activated corrosion products traced to the primary circuit material (Neeb, 1997, pp. 163-164). From these three categories, the major radioactivity and radiotoxicity threat is caused by the fission and activation products from the nuclear fuel due to their excessive proportions compared to other activation products in the reactor.

On the other hand, the activation corrosion products are responsible for the contamination buildup of the primary circuit. Consequently, the buildup increases both radiation dose rates at the surfaces of the primary circuit as well as radiation risks to personnel carrying on operational procedures like repairing and inspection. By contrast, the activation products of the coolant, except ^{16}N, are only relevant in the case of off-gas or wastewater release.

Fission products of cesium such as ^{137}Cs and ^{135}Cs as mentioned in Lehto and Hou (2011, p. 92) are released only in small amounts from the failed fuel rod to the coolant under constant-load operating conditions (Neeb, 1997, pp. 194-195). Still, they and other fission products of the actinides, the alkaline earths, e.g., isotopes of strontium such as ^{90}Sr and the rare earth elements are frequently present in the coolant due to the transport processes occurring during changes in the reactor coolant system (U.S.NRC, 2017).

For instance, strontium and its isotopes originated from fission form a highly soluble oxide, SrO, and are dissolved into the coolant as cationic state (Neeb, 1997, p. 123, 237). Strontium may also exist as colloidal particles (Brey, Butikofer, McConnell, & Rogers, 1998) and form complexes with complexing agents such as oxalic acids and oxalates as mentioned in Marinin and Brown (2000). According to Neeb (1997, p. 195, 221), low decontamination factors of released cesium on the ion exchange resins and saturation of resins with LiOH cause cesium to accumulate in the coolant. Moreover, the characteristics of cesium in forming soluble compounds in the primary coolant prevents it from attaching on the primary circuit surfaces.

On the other hand, isotopes of cobalt such as ^{60}Co, ^{58}Co and ^{57}Co can be present in the coolant either as dissolved ions, suspended solids or as deposition in the oxide layer on the primary circuit surfaces (Neeb, 1997, p. 225). The main activation corrosion product of primary circuit materials like stainless steel and nickel-cobalt alloys is ^{60}Co, which is always present in the primary circuit. It is produced by neutron activation of corroded metal atoms in the reactor core, where it is released into the coolant. Its high gamma-radiation energies and buildup on surfaces are the main causes of high radiation dose rates of the primary circuit and its components (Neeb, 1997, p. 244, 265).

2.2.1 Chemistry of cobalt

The fourth period of the periodic table includes 3d-transition metals from scandium to zinc. These metals have in common full 3s, 3p and 4s shells with some exceptions as well as increasing filling of the 3d shell with atomic number as stated in Lehto and Hou (2011, pp. 123-125). They follow the electronic configuration of $[Ar]3d^x4s^y$, where x has values from 1 to 10 and y from 1 to 2. Cobalt´s (Z = 27) electronic structure is, for example, $[Ar]3d^74s^2$. Radiochemically important 3d-transition metals such as chromium, manganese, iron, nickel, copper, zinc and cobalt have typical oxidation states between + II to +VII. Greenwood and Earnshaw (1997, p. 1116) argue that there are four different oxidation states for cobalt, + II, + III, + IV and +V, from which +II is the most typical state as well as Co^{+2} is the major form in solutions as mentioned in Lehto and Hou (2011, p. 124).

The divalent 3d-transition metals such as cobalt, nickel, copper and zinc represent the most soluble metals of the fourth period as the solubility of these elements depends on the oxidation state (Lehto & Hou, 2011, p. 125). The divalent metals hydrolyze much less than tri- or

tetravalent metals, form sparingly soluble hydroxides, carbonates, oxalates and sulfides as well as form easily complexes. For example, cobalt occurs in arsenides and sulfides, e.g., CoAsS, $CoAs_2$ and Co_3S_4 in commercial ores in, e.g., Africa and Canada (Greenwood & Earnshaw, 1997, p. 1114).

Cobalt is mainly used in the production of chemicals needed in ceramic and paint industries, although some other applications are catalysts in organic reactions and manufacturing magnetic alloys (Greenwood & Earnshaw, 1997, p. 1115). According to Sonzogni (2005) it has one stable isotope, ^{59}Co , and several unstable isotopes, from which the most important are ^{58}Co and ^{60}Co as mentioned in Lehto and Hou (2011, p. 124). The radionuclides differ from each other by half-lives, decay modes and purposes of use, but not for gamma radiation: 811 keV (99 %, ^{58}Co), 1173 keV and 1333 keV (100 %, ^{60}Co) (The lund/LBNL nuclear data search.1999).

The nuclear reaction ^{58}Ni (n, p) ^{58}Co mentioned in Neeb (1997, p. 155) is used to produce ^{58}Co (71 d, EC) for, e.g., radiotracer purposes as in Jain, Siddiqui and Singh (1979) and in Rønnov-Jessen and Hansen (1965). By contrast, the nuclear reactions of ^{59}Co (n, γ) ^{60}Co, ^{60}Ni (n, p) ^{60}Co and ^{63}Cu (n, α) ^{60}Co producing β^--emitting ^{60}Co with half-life of 5,3 a take place in the primary circuit of a nuclear power plant and accumulate contamination from the activation of stainless steel (Neeb, 1997, p. 250). This buildup contamination caused by ^{60}Co is then responsible for larger radiation doses to NPP workers than other radionuclides as stated in Lehto and Hou (2011, p. 123). On the other hand, it can be used in various fields of research as a source of γ-radiation like in medical treatments of tumors as mentioned in Greenwood and Earnshaw (1997, p. 1115).

2.2.2 Chemistry of cesium

The first group of the periodic table consists of alkali metals from lithium to francium. They all have in common a half full s-orbital in the outer shell, M^{+1}-ions in aqueous solutions and oxidation state of +I as well as a strong electropositive character (Lehto & Hou, 2011, pp. 91-92). Moreover, their electropositive character increases with the atomic number, making cesium the second most electropositive element in the group. Due to their ionic behaviour, the alkali metals form soluble halides and aqua complexes, whereas hydroxyl and organic complex formations are rare and uncommon.

As being one of the alkali metals, cesium has an electronic structure of $[Xe]6s^1$, the atomic number of 55 and abundance of 2,6 ppm in crustal rocks, where it occurs mainly as the hydrated aluminosilicate as mentioned in Greenwood and Earnshaw (1997, pp. 69-71, 74-75). Due to its low abundance compared to other alkali metals like lithium (18 ppm) and sodium (22 700 ppm), there is only one commercial source of Cs available in the world. Thus, golden yellow Cs is mainly acquired by the Li industry as its byproduct. Cesium has applications in, e.g., atomic clocks (Giordano, 2013, p. 1011), solar cells (Kulbak et al., 2015) and alkali vapor laser (Zhdanov, Ehrenreich, & Knize, 2006).

According to Lehto and Hou (2011, pp. 91-92) radiochemically most important isotopes of cesium are ^{137}Cs, ^{134}Cs and ^{135}Cs, when the only naturally occurring isotope is ^{133}Cs (Sonzogni, 2005). These radionuclides have half-lives of 30 a (^{137}Cs), 2,1 a (^{134}Cs) and 2,3 $\times 10^6$ a (^{135}Cs). They decay by β^--emission, although ^{134}Cs has a minor decay mode of electron capture (EC). The main energies and intensities of their γ-radiation are 662 keV (85 %, ^{137}Cs), 605 keV (98 %, ^{134}Cs) and 796 keV (86 %, ^{134}Cs), whereas ^{135}Cs is pure β^--emitter (The lund/LBNL nuclear data search.1999). Radionuclides ^{137}Cs and ^{135}Cs are produced by fission of uranium and plutonium, while ^{134}Cs is formed by neutron activation reactions of ^{133}Cs in nuclear reactor.

From these three, ^{137}Cs is the main source of radioactive contamination passing to humans in food as emphasized in Lehto and Hou (2011, pp. 91-94). Its wide presence in in the environment is explained by atmospheric nuclear weapons testing in the 1950s to 1970s, the Chernobyl accident 1986 and the Fukushima accident in 2011 (Yasunari et al., 2011). On the other hand, its abundance in food and human tissue is due to its chemical behaviour similar to potassium. Moreover, the low boiling point of cesium (671 °C) causes it to evaporate in nuclear explosions and NPP accidents, thus spreading the fallout of radioactive cesium widely in the environment through atmospheric aerosol particles (Lehto & Hou, 2011, p. 95). After deposition to the ground, cesium tends to bind to clay minerals in soil, sediments and water.

2.2.3 Chemistry of strontium

The group 2 of the periodic table called the alkaline earth metals consists of metals from beryllium to radium. Characteristics to these metals are full s-orbital in the outer shell, oxidation state of +II and M^{+2}-ions in aqueous solutions (Lehto & Hou, 2011, pp. 99-101). Moreover, their electropositivity and ion size increases with the atomic number, whereas hydrated ion size is indirectly proportional to the atomic number. In addition, the alkaline earth metals mainly form ionic bonds with the exemption of beryllium, which prefers covalent bonds. The alkaline earth metals form, e.g., hydroxides, halides, carbonates, phosphates and chromates in various conditions, but are mostly not able to assemble coordination complexes with organic compounds.

On the other hand, strontium forms soluble hydroxides and insoluble carbonates, sulfates, oxalates, chromates, nitrates and phosphates as well complexes with crown ethers, uncommon to other alkaline earth metals than radium as stated in Lehto and Hou (2011, pp. 100-101). Moreover, strontium (Z = 38) with electronic configuration of $[Kr]5s^2$, occurs in crustal rock (384 ppm) as, e.g., insoluble carbonates, sulfates and silicates like other alkaline earth metals, magnesium, barium and calcium (Greenwood & Earnshaw, 1997, pp. 109-112). Strontium´s main minerals in crustal rock are celestite ($SrSO_4$) and strontianite ($SrCO_3$), which are produced from different locations around the world to be used in, e.g., glass production for television and computer monitors, pyrotechnic displays and magnetic materials.

According to Lehto and Hou (2011, p. 100, 106) the most important radionuclides of strontium are ^{85}Sr, ^{89}Sr and ^{90}Sr, of which only ^{85}Sr is used as a tracer and the others are fission products with high ^{235}U fission yields of 4,7 % and 5,8%. These fission products are released in the environment by nuclear weapon testing, nuclear waste and through the core melt-concrete interactions in NPP accidents (Neeb, 1997, p. 533). From these radionuclides, only ^{85}Sr has gamma emission of 514 keV with 96 % intensity (The lund/LBNL nuclear data search.1999). The other are pure β^- -emitters with maximum energies of 1,50 MeV (^{89}Sr) and 0,55 MeV (^{90}Sr). Their half-lives are 65 d (^{85}Sr), 51 d (^{89}Sr) and 29 a (^{90}Sr).

Besides ^{90}Sr having the longest half-life of the isotopes of strontium, it is also the most significant fission product of uranium and plutonium with ^{137}Cs as emphasized in Lehto and Hou (2011, pp. 106-107). Although they occur in the same levels in the nuclear fuel and cause the major activity of it for some hundred years, they will decay before causing long-

term major radiation hazard in the final disposal of spent nuclear fuel. On the other hand, there are higher amounts of ^{137}Cs compared to ^{90}Sr in low and medium active NPP waste such as, e.g., in spent organic resins and waste effluents due to their differences in solubility and volatility (Greenwood & Earnshaw, 1997, p. 75, 112).

2.3 Organic ion exchangers

The technical application of organic ion exchangers, generally noted as ion-exchange resins, originate from the development of sulfonated coal during the 1930s (Luca, 2000, pp. 1617-1618) Since, organic ion exchangers have been synthesized of various materials such as wood, paper, cotton and lignin by different chemical methods, e.g., sulfonation and phosphorylation. As mentioned in Hokkanen et. al. (2016), other direct chemical modification methods can be, e.g., esterification, halogenation, oxidation, etherification, alkaline treatment and silynation, whereas indirect methods are based on monomer-grafting through photografting, high energy radiation grafting or chemical initiation grafting. An example of suitable functional groups on grafted cellulose with desirable adsorption properties is presented on Figure 1.

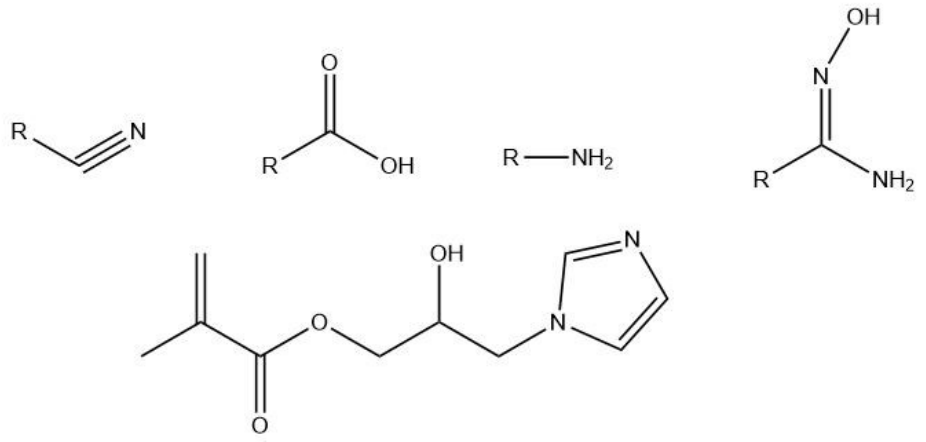

Figure 1: Nitrile (left), carboxyl, amine, amidoxime and GMA-imidazole (below).

On the other hand, the development of synthetic organic ion exchangers has overridden chemically modified organic resins by providing wider technical applications through greater chemical stability, mechanical strength and suitable physical structures as argued in

Luca (2000, p. 1618). These favourable properties can be achieved through two main reactions: polycondensation and addition polymerization, from which polymerization processes produce the majority of commercially used ion exchangers.

These ion exchangers have higher cross-linking, better defined physical features and preferable oxidative stabilities than polycondensation exchangers due to their different production methods. In polycondensation a trifunctional co-monomer is incorporated with a cross-linking agent, e.g., formaldehyde, whereas in polymerization a bifunctional monovinylic monomer is combined with a divinylic monomer such as divinylbenzene. They both form gel-type resins with three-dimensional hydrocarbon matrix, in which exchangeable solutes are associated with fixed acid or basic groups as stated in Luca (2000, p. 1617).

The development of polymerization ion exchangers has led to the invention of macroporous resins, in which monovinylic monomer, styrene, is combined with divinylbenzene in the presence of suitable inert compound (Luca, 2000, p. 1618). The main compounds and the macroporous cross-linking structure are presented in Figure 2 and Figure 3. *R* represents ion-exchange sites in Figure 3. The process produces resins with significant physical porosity and higher sorption rates of ions and non-electrolytes than the previous conventional methods. The macroporous resins can even be used with non-aqueous solvents, which are not suitable for other organic resins.

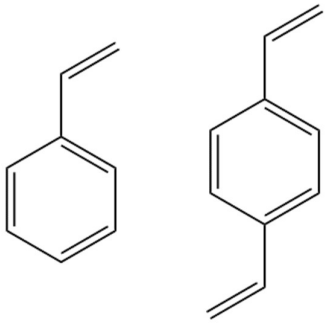

Figure 2: Macroporous resins consist of styrene (left) and divinylbenzene (right).

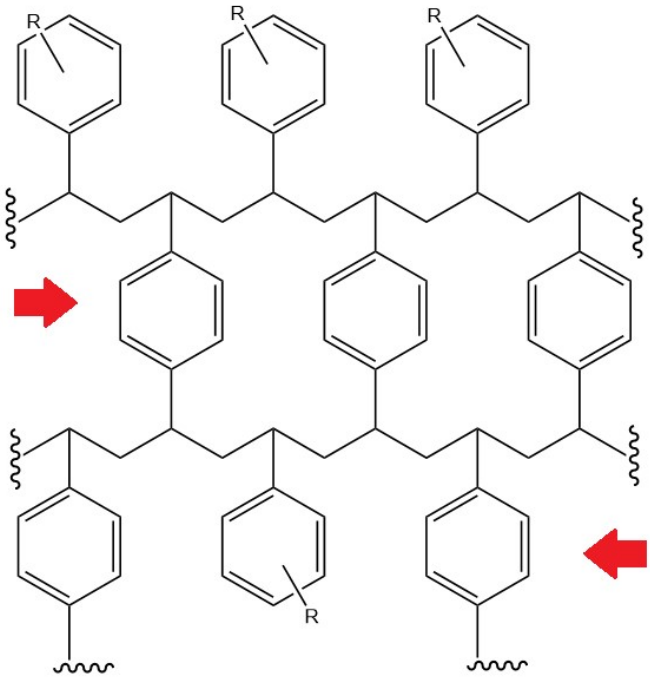

Figure 3: Cross-linking shown in red in macroporous resin.

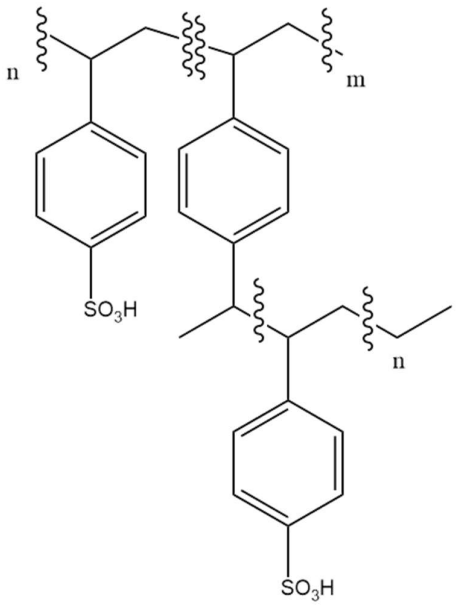

Figure 4: An example of cross-linked polystyrene sulfonic acid.

Synthetic organic ion exchangers can be produced in various forms such as beads, granules and fibres depending on their production method (Luca, 2000, p. 1618-1619). In addition, synthetic organic ion exchangers can be divided to cation and anion exchangers and subdivided to strong and weak exchangers according to the properties of their functional groups and exchangeable ions. As an example, cross-linked polystyrene sulfonic acid commonly represents a strong acidic cation exchanger (Lehto & Hou, 2011, pp. 64-65) as shown in Figure 4, where the *m*- and *n*-labels represent monomers of divinylbenzene and styrene. By contrast, ion exchangers may also be amphoteric having both anion and basic groups in their matrix. The electrolyte sorption then depends on the relatively strength of these anion and basic groups allowing separation of different solutes (Luca, 2000, p. 1628)

2.3.1 Cellulose-based organic ion exchangers

As mentioned in Wegscheider et al. (1981) unmodified cellulose has a very low adsorption capacity and the majority of this capacity is due to the acidic functional groups such as carboxyl groups either attached directly to cellulose or to materials associated with it like lignin or hemicelluloses. Chemical modifications of cellulose improve its adsorption capacity as stated in Hokkanen et al. (2016) and produce cellulose products, which don´t dissolve or swell excessively in dilute acid or base solutions according to Wegscheider et al. (1981).

The main benefits of these cellulose products such as cellulose-based organic ion exchangers are their large surface area, fine particle size and porous structure, the latter of which permits the adsorption of larger molecules than other ion exchange resins. For example, large molecules such as proteins, nucleic acids and lipids can be separated through different cellulose ion exchangers such as carboxymethyl cellulose (CM) and diethylaminoethyl cellulose (DEAE) as mentioned in Grubhofer (1991, pp. 445-447). According to Wegscheider et al. (1981) other benefits of cellulose-based organic ion exchangers are their fast rate of exchange, high purity and adjustable chemical and mechanical stability. Moreover, their hydrophilic character, variation in quality and cross-linking possibilities can be taken as an advantage.

On the other hand, their major general limitations besides low capacities are the loss of original physical properties with increase of substitution and swelling, all of which can be avoided through appropriate introduction of cross-linking and suitable ionic groups as argued in Wegscheider et al. (1981). Moreover, the low selectivity of cellulose ion exchangers

was mentioned as the major cause limiting their applications in cases where preconcentration and separation of trace ions from excess amount of concomitant material were needed. On the other hand, the low selectivity can be avoided by immobilizing suitable chelating agents into cellulose. These chelating agents could be, e.g., glycine, phosphate ester and dithiocarbamate as mentioned in Garg, Sharma, Bhojak and Mittal (1999) or amidoxime, hydrazine or malonic acid groups among others as in Fischer and Lieser (1993). Chelating celluloses can be used for different applications such as selective separation of uranium (Fischer & Lieser, 1993), low-level radioactive waste treatments (Othman et al., 2009) and for recovery of heavy metals (Grubhofer, 1991).

2.3.2 Lignin-based organic ion exchangers

In addition to cellulose, organic ion exchangers or biosorbents can be made from lignin by, e.g., isolating lignin directly from black liquor (e.g., Guo, Zhang, & Shan, 2008; Kamel, 2005; Mohan, Pittman, & Steele, 2006; Srivastava, Singh, & Sharma, 1994), by condensation polymerization of sodium lignosulfonate (Liang et al., 2013), by alkali glycerol delignification of wood (Demirbas, 2004) or by the whole kraft process (e.g., Crist, Martin, & Crist, 2002; Zoumpoulakis & Simitzis, 2001). The capabilities of lignin-based materials to remove heavy metals from waste waters or industrial effluents have been studied multiple times (e.g., Crist et al., 2002; Demirbas, 2004; Guo et al., 2008; Mohan et al., 2006; Wu, Y., Zhang, Guo, & Huang, 2008). As a result, it has been found that lignin has a high adsorption capacity on certain heavy metals, e.g., lead and zinc, partially due to its surface functional groups such as polyhydric phenols (Srivastava et al., 1994). Moreover, the adsorption capacity on other heavy metals, such as copper and cadmium, has been shown to be better with lignin extracted from black liquor than with other biosorbents, carbons or adsorbents as mentioned in Mohan et al. (2006).

Studies on lignin-based materials may offer new applications for lignin as ion exchangers (e.g., Kamel, 2005; Liang et al., 2013) as well as possible future replacements for existing commercial resins as mentioned in both Demirbas (2004) and Liang et al. (2013). According to Mohan et al. (2006), lignins are inexpensive and environmentally friendly materials for water treatment; most of which are nontoxic and produced in large quantities , e.g., as black liquor as the main by-product from the kraft process. On the other hand, the markets of lignin-based products are restricted and limited to low value commodities, since they have not yet achieved commercial breakthrough as ion exchange resins (Liang et al., 2013).

2.4 Microcrystalline cellulose

Microcrystalline cellulose (MCC) is almost white and odorless purified cellulose produced from different lignocellulose sources by various techniques such as acid hydrolysis (Vanhatalo, 2017, p. 14-20). It can be produced from different raw materials such as waste biomasses, annual plants and wooden materials as well as turn to different final products depending on the modification process. For example, it can be dried to different powder products as seen in Figure 5, turned into redispersible gels and combined with water-soluble polymers such as cellulose gum to gain colloidal properties of MCC as mentioned in Tuason, Krawczyk and Buliga (2010, p. 218). These unique colloidal properties of MCC have led to the development of its application technology as well as to the extensive research on its functional properties like texture modification, foam stability and fat replacement.

Figure 5: Different MCC powders with and without lignin.

Microcrystalline cellulose is defined by The Food and Agriculture Organization of the United Nations Document Repository (FAO 1996) as “purified, partially depolymerized cellulose prepared by treating alpha-cellulose, obtained as a pulp from fibrous plant material, with mineral acids. The degree of polymerization is typically less than 400. Not more than 10 % of the material has a particle size of less than 5 μm”. It can also be defined by Battista and Smith (1962) as “a mechanically disintegrated level-off degree of polymerization cellulose, which is a product resulting from, or equivalent to, the hydrolysis of purified cellulose after 15 minutes in 2,5 N HCl at 105 ± 1 ºC”.

As stated in Battista (1971), the commercially suitable properties of microcrystalline cellulose were discovered in the 1950s. Since, its production has been based on different modifications of chemical processes (Battista & Smith, 1962), enzymatic hydrolysis (Braunstein et al., 1994), hydrothermal processes (Chornet, Cloutier, & Jollez, 2003) and on a combination of these techniques (Dobashi, Uchida, & Ohara, 1992). Moreover, some new production methods are even based on implementations of mild kraft pulp hydrolysis (Vanhatalo & Dahl, 2014). From all these processes, mineral acid hydrolysis with hydrochloric acid (HCl) or sulfuric acid (H_2SO_4) covers most of the microcrystalline production in the world, as mentioned in Vanhatalo, Parviainen and Dahl (2014).

Moreover, microcrystalline cellulose has a huge variety of industrial applications due to its suitable physical and chemical properties. As mentioned in Vasiliu-Oprea and Nicoleanu (1993), these properties can be high thermostability, heat resistance and opaque character of the material. Other favorable properties of microcrystalline cellulose are high specific surface area and porosity, rigid structure, noncaloric character, formation of colloids, powders and gels as well as a good workability of the material. Thus, the utilization of MCC covers wide areas of different industries such as pharmaceuticals, cosmetics and food industry.

In addition, there has been studies on other industrial applications of MCC such as flame-retardant composites, e.g., epoxy/microcrystalline cellulose composite (Wu, K., Shen, Hu, Xing, & Wang, 2011) and polypropylene/MCC composite containing $Al(OH)_3$-nanoparticles (Samat, Zulkapli, Halim, Ahmad, & Habibah, 2015), hybrids, e.g., microcrystalline cellulose-SiO_2 hybrids as tire tread compounds (Sun, Liu, Liang, Wang, & Liu, 2017) as well as polymer nanocomposites such as composite of MCC and polyurethane (Wu, Q., Henriksson, Liu, & Berglund, 2007). Even its ion exchange properties have been investigated, e.g., by comparing bovine serum albumin adsorption capacity of modified MCC to commercial DEAE -cellulose with weak results (Teshirogi & Ohtomo, 1986) and by separating successfully free nucleotides with polyethyleneimine-microcrystalline cellulose (Christianson, Paulis, & Wall, 1968).

2.4.1 Cellulose

The world´s most significant biopolymer, cellulose, has estimated yearly grow of 10^{11} tons, part of which comes from different wood species. According to Alén (2000b, pp. 28-29, 34), cellulose typically makes up 45 % of wood, whereas other constituents, e.g., lignin and hemicelluloses only 25-35 %. The rest of wood is then composed of extractives, organic and inorganic compounds, pectin, starch and protein. On the other hand, the lignin content of different tree species may range from 15 % up to 40 % depending on, e.g., the gravitropic stimulation and mechanical stress as stated in Novaes, Kirst, Winter-Sederoff and Sederoff (2010). Also, the cellulose and hemicellulose contents depend on the wood types, softwood and hardwood, varying from 40 % to 45 % and 25 % to 35 % (Alén, 2000b, p. 28).

Cellulose has a linear, unbranched and polydispersed homopolysaccharide structure, in which β-D-glucopyranose units in $^4C_1$ conformation are linked together by β(1-4) bonds (Alén, 2000b, p. 34). In this conformation, all functional groups, e.g., C_1-OR, C_2-OH and C_5-CH_2OH of the β-D-glucopyranose units orientate equatorially, which stabilizes the chain structure and decreases the interactions between functional groups of the pyranose ring. Aliphatic hydrogen atoms in axial positions along with equatorial substituents result high interchain hydrogen bonding between neighboring cellulose chains and less strong hydrophobic interactions between layers of cellulose as mentioned in Himmel et al. (2007). The former interactions cause cellulose to resist enzymatic hydrolysis, whereas the latter interactions resist acid hydrolysis. Due to its linear structure, it has also both reducing (C_1-OH) and nonreducing ends (C_4-OH) (Alén, 2000b, p. 34). The molecular structure of cellulose as well as the numbering of carbon atoms is shown in Figure 6.

In addition, cellulose has a high tendency for inter- and intramolecular hydrogen bonds, which causes it to aggregate to microfibrils in plant cell walls as mentioned in Alén (2000b, p. 24, 35). The further aggregation of these microfibrils forms firstly highly organized (crystalline) and less ordered (amorphous) regions and secondly special cellulose structure with high degree of crystallinity. This special structure called fiber wall cellulose results in cellulose to be soluble only in a couple solvents, e.g., cupriethylenediamine (CED), cadmiumethylenediamine (Cadoxen) and *N*-methylmorpholine *N*-oxide. In the crystalline regions, chains of short fragments cleaved from cellulose, cellodextrins, are highly organized and provide cellulose high resistance to chemical and biological hydrolysis, whereas amorphous regions do not (Himmel et al., 2007).

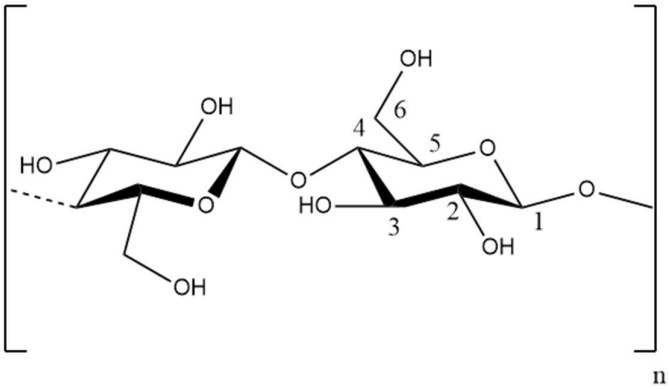

Figure 6: Stereochemical structure of cellulose.

The degree of polymerization (DP) is defined by IUPAC Gold book (1996) as "the number of monomeric units in a macromolecule or oligomer molecule, a block or a chain." According to Zhang and Lynd (2005) DP is "an important property of cellulosic materials for functionally based models of enzymatic cellulose hydrolysis, as well as for paper-making and other applications." It can be determined by dissoluting cellulose, e.g., in metal complex solutions, inorganic acids and ionic solutions and measuring the DP by, e.g., size-exclusion chromatography, membrane osmometry or cryoscopy as listed in Zhang and Lynd (2005).

For native wood cellulose, the degree of polymerization is of the order of 10 000, whereas the DP of cotton cellulose is approximately 15 000 as stated in Alén (2000b, p. 34). These DP values correspond to 1,6 and 2,4 million Da and lengths of 5,2 and 7,7 µm, which can be reduced by chemical and physical modifications of cellulose. For example, the degree of polymerization of cellulose reaches values of 500 to 2000 in chemical pulping and even below 500 in further processing like producing microcrystalline cellulose (e.g., Shlieout, Arnold, & Müller, 2002). Even smaller values can be achieved in crystalline regions, where the DP of soluble cellodextrins can range from 2 to 12 (Zhang & Lynd, 2005).

2.4.2 AaltoCell™

Microcrystalline cellulose has traditionally been produced by different methods using chemical-, hydrothermal- and enzymatical processing or combinations of these techniques with long retention times, moderate chemical usage and high amounts of waste waters (Husgafvel, Vanhatalo, Rodriguez-Chiang, Linkosalmi, & Dahl, 2016). A new, environmentally cleaner method to produce microcrystalline cellulose from chemical pulp was introduced in 2011 by Aalto University (Dahl, Vanhatalo, & Parviainen, 2011a; Dahl, Vanhatalo,

Parviainen, & Svedman, 2011b). This new method, AaltoCell^{TM}-process, is based on integrating the production of MCC to a chemical pulp mill, which provides, e.g., better economical assets and operational savings compared to non-integrated process (Vanhatalo & Dahl, 2014). Moreover, the process makes possible large production capacity and production of MCC with controlled concentrations of lignin by taking less chemicals in shorter retention times and producing less wastewater than in conventional methods as stated in Husgafvel et al. (2016). It was even awarded in the Ministry of Employment and the Economy international biorefinery competition on 2015 (Dahl, 2017).

According to the patent (Dahl et al., 2011b), this new method is based on mild acid hydrolysis with minimum of 8 % consistency on dry weight of used fibrous cellulosic material and minimum constant temperature of 140 °C. Added acid concentration should be between 0,2 -2 % on dry weight of used material. On the other hand, after the second patent (Dahl et al., 2011a) even temperatures as low as 80 °C may be adequate for sufficient acid hydrolysis if even a part of the manufacturing process is integrated with a kraft pulp mill. After the latter patent, acid concentrations up to 10 % on dry weight of the cellulose are acceptable. The microcrystalline cellulose produced by these methods is defined as AaltoCell^{TM} (Vanhatalo, 2017, p. 10).

AaltoCell^{TM} materials were used in this research as sample materials for various structural and ion exchange measurements to determine their capability to sorb chosen radionuclides. AaltoCell^{TM} materials were made from bleached softwood kraft pulp, oxygen delignified softwood pulp and unbleached softwood kraft pulp according to the procedures stated in the patents Dahl et al. (2011a) and Dahl et al. (2011b).

2.4.3 Lignin

Lignin is the second most abundant terrestrial biopolymer after cellulose, consisting of ~ 30 % of the organic carbon in the biosphere (Boerjan, Ralph, & Baucher, 2003). Its high abundance is mainly due to its critical functions in stiffening and strengthening the stem and forming structural consistency of the cell wall, which all have developed during the evolution of terrestrial plants. Other favorable properties of lignin are its ability to waterproof the cell walls, protect the plant against pathogens and support transportation of water and dissolved minerals through vascular system.

According to Alén (2000b, p. 39) lignin differs distinctly from the other macromolecules of wood due to its irregular and amorphous chemical structure, where no systematical order in links between different building units can be observed. Neither is its real molecular mass known when lignin is attached to wood (p. 41). It is mainly formed by enzymic dehydrogenative polymerization of three *p*-hydroxycinnamyl alcohols as shown in Figure 7. On the other hand, there are also other building units in native lignin, e.g., γ-acetate, ferulates and dihydroconiferyl alcohol, which derive from acylation of monolignols, incomplete monolignol biosynthesis or other reactions related to the biosynthesis (Boerjan et al., 2003).

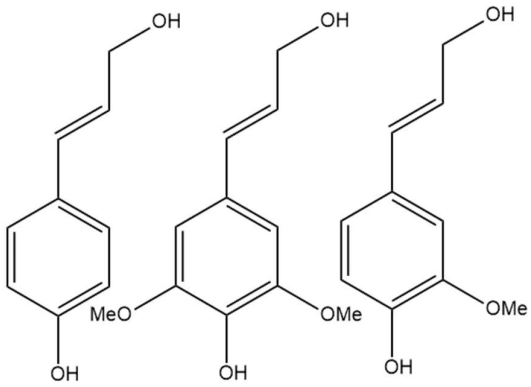

Figure 7: From the left: *trans-p*-Coumaryl alcohol, *trans*-Sinapyl alcohol and *trans*-Coniferyl alcohol.

According to Alén (2000b, p. 39) the disorganized structure of lignin arises from numerous oxidative coupling reactions of the resonance-stabilized phenoxy radicals formed from the α,β-unsaturated basic units of lignin in Figure 7. Boerjan et al. (2003) states that, during this lignification process, a basic monolignol unit couples to the accreting polymer at its *β*-position forming *β*-linked β-aryl ethers, phenylcoumarans and dibenzodioxocins as seen in Figure 8. In Figure 9, structures like biphenyl and biphenyl ether are derived from coupling of these preformed lignin oligomers. Exceptionally two basic monolignol units couple and form structures such as resinol and cinnamyl alcohol end groups. These two processes, lignification and dimerization of monolignols produce different outcomes: the first mainly 5-5 (biphenyl) and 5-O-4 (biphenyl ether) units and the second *β*-linked dimers. The major interconnection unit is still *β*-O-4 (β-aryl ethers) linkage, which is easier chemically cleaved than other linkages. This character of the linkage is widely utilized in chemical pulping and analytical methods as mentioned in Boerjan et al. (2003).

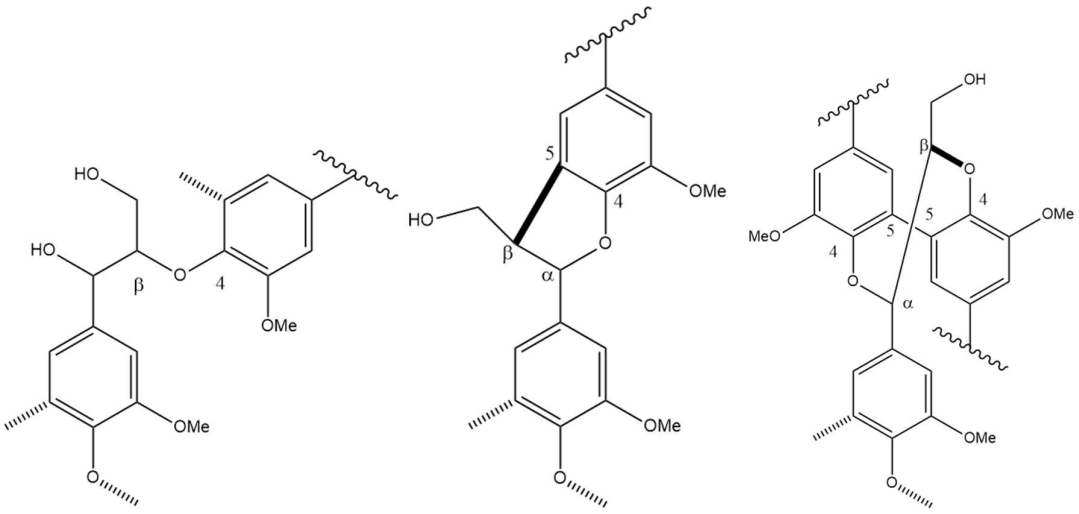

Figure 8: From the left: β-aryl ether (β-O-4), phenylcoumaran [β-5 (α-O-4)] and dibenzodioxocin [5-5/β-O (α-O-4)].

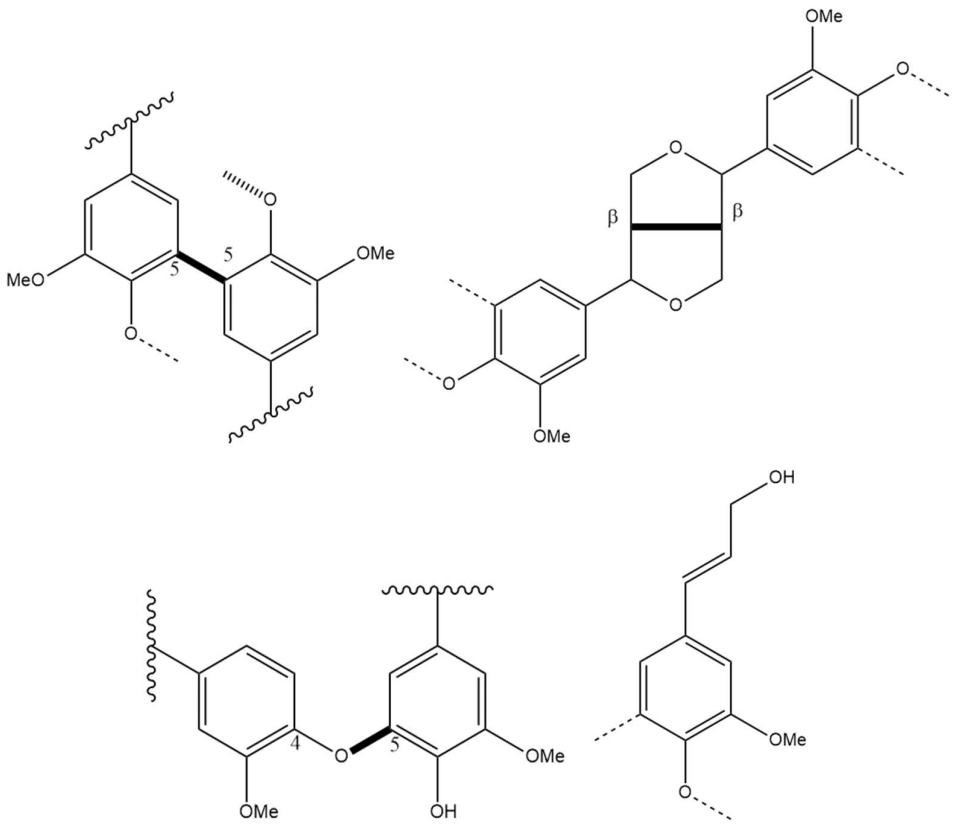

Figure 9: From the top left: biphenyl [5-5] and resinol [β-β (γ-O-α)] and from the bottom left: biphenyl ether [5-O-4] and cinnamyl alcohol end group.

Lignin can be classified into three major types of the native lignin, softwood, hardwood and grass lignin, and into several minor types of industrially produced lignin (Alén, 2000b, p. 39). Originating from the by-production of chemical pulping, these minor types of lignin can be kraft lignin, alkali lignin and lignosulfonates derived from kraft, soda-AQ (anthraquinone) and sulfite pulping. Moreover, there are also wood-based organosolv lignins derived from the organic solvent pulping and acid hydrolysis lignins from acid hydrolysis processes.

During kraft pulping native lignin goes through different degradation reactions, which are either facilitated by nucleophilic hydrogen sulfide ions or hydroxyl ions as discussed in Alén (2000a, pp. 63-65). These reactions produce a complex mixture of the degradation products with a wide spectrum of molecular masses. The liberation of phenolic hydroxyl groups in the presence of hydrogen sulfide ions results in increased hydrophilicity and water-solubility of the lignin fragments, from which the soluble products are referred to as kraft lignin. Other products can be elemental sulfur and unsaturated styrene-type structures (p. 67).

These reactions are mainly based on the cleavage of α- and β- aryl ether linkages, which form the majority of the different linkages in both softwood and hardwood lignins (p. 66). On the other hand, delignification gives rise to condensation reactions, which lead to more insoluble and larger fragments and to demethylation reactions, which produce toxic methyl mercaptan and dimethyl sulfide gases (p. 68). Moreover, unsaturated and highly conjugated lignin structures, such as chromophores and leucochromophores, are formed during kraft process causing the dark brown color of the pulp as mentioned in Alén (2000a, p. 68)

The botanical origin, the major type of lignin, the cell type, the cell wall layer among other factors determine the proportions of lignins´ basic units as mentioned in Alén (2000b, p. 31, 40). For example, softwood lignins are sometimes called “guaiacyl lignins” due to the high content of *trans*-coniferyl alcohol (90%) in the structure. On the other hand, hardwood lignins and grass lignins are referred to as “guaiacyl-syringyl lignins” for their high content of both *trans*-coniferyl alcohol and *trans*-sinapyl alcohol. When incorporated into the lignin polymer, these three *p*-hydroxycinnamyl alcohols form *p*-hydroxyphenyl, guaiacyl and syringyl phenylpropanoid units seen on Figure 10.

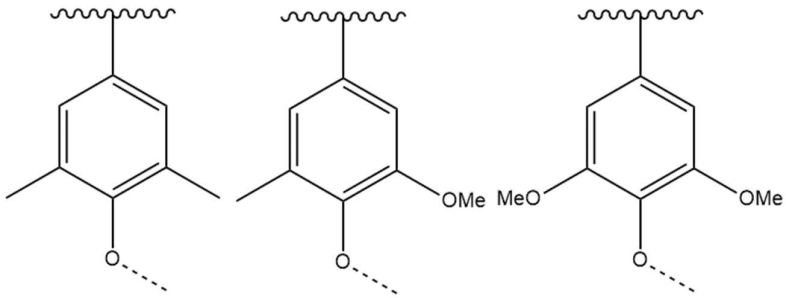

Figure 10: General p-hydroxyphenyl, guaiacyl and syringyl units.

3 Analysis techniques

AaltoCell^{TM} materials were analyzed by their structural and ion exchange properties through different analysis techniques from BET (Brunauer, Emmet, Teller) to gamma spectroscopy. The research was conducted in both the Aalto University and the University of Helsinki. The structural properties were measured through BET, SEM (Scanning Electron Microscopy), GPC (Gel Permeation Chromatography), HPAEC (High Performance Anion Exchange Chromatography) and XPS (X-ray Photoelectron Spectroscopy) in the Department of Bioproducts and Biosystems in the Aalto University, whereas gamma radiation spectroscopy as well as different batch sorption techniques were executed in the Department of Chemistry in the University of Helsinki. The analysis techniques were chosen according to the literature and to the common practices of laboratories of both departments as well as to available instruments fit for the research purpose. Each analysis technique is described in detail and their significance to the research on the suitability of MCC as an ion exchanger is emphasized.

3.1 BET surface area analysis

Determination of specific surface area and porosity of solid samples, like cellulose, pigment surfaces or microcrystalline cellulose, can be conducted by measuring the adsorption of gases on the surface of the sample (Stenius, 2000, pp. 194-197). Adsorption of adsorbate such as certain gas can be modeled with, e.g., the Langmuir isotherm, the BET isotherm and other models like pseudo first order model and Crank model as mentioned in Largitte and Pasquier (2016). According to Stenius (2000, p. 194, 196) the Langmuir adsorption isotherm describes chemisorption and strong site-bound adsorption between solution and solid, where a specific plateau level is reached after occupation of all surface sites of the solid. According to the Langmuir isotherm, adsorption only occurs independently on each site in a monolayer

of the surface of the solid. This isotherm is suitable for characterizing catalyst, whereas the BET isotherm fits better for physical adsorption of gases.

Although the adsorption is assumed to take place on the first layer as in the Langmuir isotherm, the BET isotherm (Brunauer, Emmet, Teller) takes also other layers of the solid into consideration as stated in Stenius (2000, p. 196). The BET isotherm can be used to determine specific surface area and porosity and their parameters, e.g., a pore size distribution, a total volume of the pores and a mean pore radius of a solid sample with certain gases, such as N_2 and Kr (Dollimore, Spooner, & Turner, 1976). With microporous samples like MCC or cellulose, the BET model gives higher specific surface area values than the adsorption of solutes due to the sizes of gaseous adsorbates (Stenius, 2000, p. 197). One of the processes of determining the BET specific surface area is shown in Figure 11.

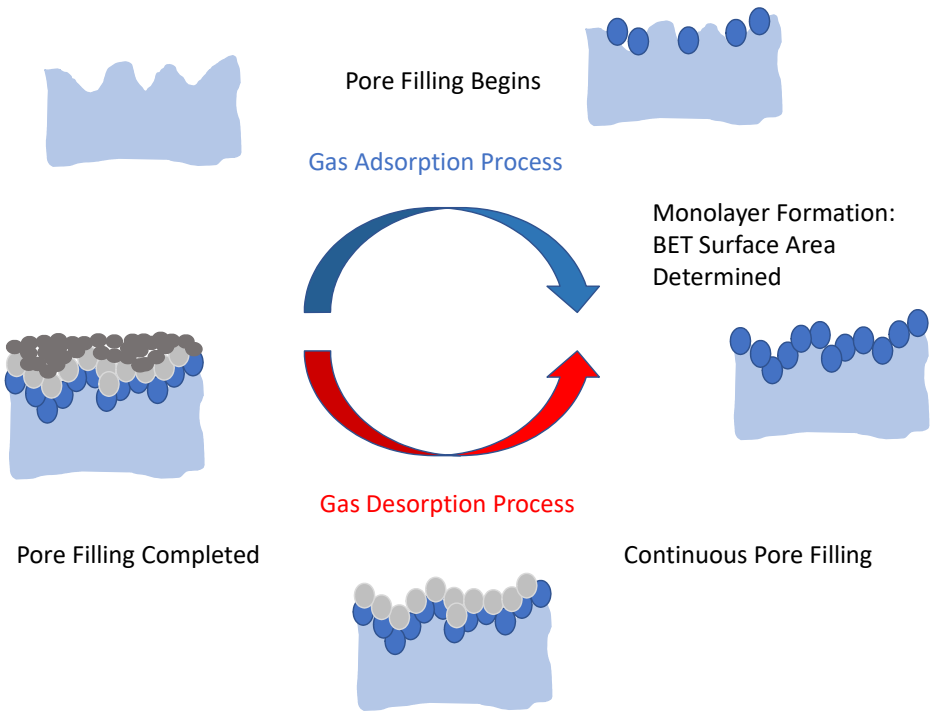

Figure 11: The process of the BET surface area analysis adapted from Particle Technology Labs (2018).

Figure 11 shows the four major steps of the BET process; the beginning of pore filling, the formation of monolayer, the pore filling and the completion of pore filling. In this volumetric method, the solid sample is first preconditioned at elevated temperature in vacuum or in inert gas flow to remove contaminants from the surface of the sample before beginning of pore filling. Then the sample is placed on the BET equipment as shown in Figure 12, where the adsorption of the chosen gas is measured according to both adsorption and desorption processes shown in Figure 11. The measurement of the absorbed gas can also be made gravimetrically (Dollimore et al., 1976) or using continues gas flow (Lowell, Shields, Thomas, & Thommes, 2004, pp. 260-261).

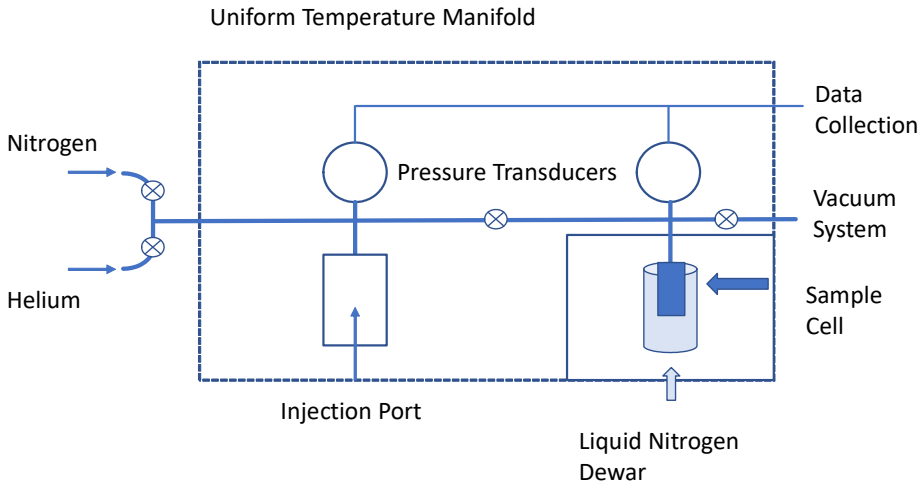

Figure 12: A schematic of the BET instrument adapted from Hwang and Barron (2011).

According to Dollimore et. al. (1976) the volumetric method, which was used in this research, is based on measuring the volume of gas adsorbed by using the perfect gas law. Measurements are done near or at the boiling point of the adsorbate gas, e.g., with N_2 at a temperature of – 195 ºC. The volumetric method fits only for gases obeying ideal gas laws, e.g., N_2, Ar and Kr, whereas gravimetric method favors other gases and vapors, e.g., water, benzene and alcohols. Moreover, the latter ones are easier to measure with scales and balances as noted in Dollimore (1976). Third way of measuring adsorbed gas is using dynamic flow method, in which nitrogen is adsorbed on the sample surface through continues flow of gas mixture of nitrogen and helium as mentioned in Lowell et al. (2004, p. 260). The change in gas pressure in constant volume is then directly proportional to moles of adsorbed gas.

3.2 Scanning electron microscopy

A SEM microscope provides detailed three-dimensional images of the surface topography of the sample even in nanometer scale (Webb & Holgate, 2003, p. 3922). According to Mehta (2012, p. 17), it allows producing magnified images of objects with higher resolutions than it is possible to achieve with optical microscope due to the limitation of diffraction effects on visible light. A scanning electron microscope reduces these diffraction effects by using focused electron beams of energy in keV with smaller wavelengths and dependence on diffraction than it is possible with visible light. Other factors affecting resolution of SEM are, e.g., the detector, the level of high vacuum, the energy of the electron beam type, its geometry and atomic numbers of the atoms in the sample as listed in Mehta (2012, p. 21).

The inner compartments of SEM are shown in Figure 13, where the main part is an electric gun such as the thermionic cathode, Schottky FEG or field-emission cathode (Reimer, 1998, p. 1). Electrons produced by the gun are further accelerated through voltage difference between anode and cathode as well as demagnified by the multiple stage electron lens system to form an electron probe with a suitable current at the specimen surface. This fine probe is then rastered over the sample surface as stated in Bindell (1992, p. 71). Besides the electromagnetic lenses and electron gun, the SEM instrument also includes electromagnetic deflection coils, the sample vacuum chamber, the stage region, the electronics console as well as the electronic power supply and the scanning modules as listed in Bindell (1992, p. 71, 76).

The SEM microscope used in this research, Zeiss Sigma VP, had several detectors to collect different fractions of emitted electrons or photons from the surface of the sample. These detectors were secondary electron detector (SED), Everhart-Thornley secondary electron detector (ETSE), backscattered electron detector with multi segment diode (BSE), variable pressure secondary electron detector (VPSE) and scanning transmission electron microscopy (STEM) (Zeiss sigma VP.2016). There are also other detectors available for SEM, e.g., energy dispersive x-ray spectrometry (EDS) detector, which, on the other hand, detects the elemental composition of the sample through the characteristics x-ray spectrum of the specimen (Kutchko & Kim, 2006).

Interactions between the electron beam and the target produce scattered electrons and photons, which provide information on, e.g., the target´s topography, elemental composition and crystalline lattice depending on certain parameters such as the beam energy, its intensity and

width as well as sample preparation as mentioned in Mehta (2012, p. 17, 20, 29). These interactions consist of interactions between the electron beam and an atom nucleus and between the electron beam and the electrons of the atom, where either coulomb attraction or repulsive forces are present. These interactions result in elastic and inelastic scattering for the electrons of the electron beam (pp. 18-19). In elastic scattering electrons don´t lose energy while hitting the target but produce measurable backscattered electrons (BSE) such as Auger electrons for imaging purposes (p. 72).

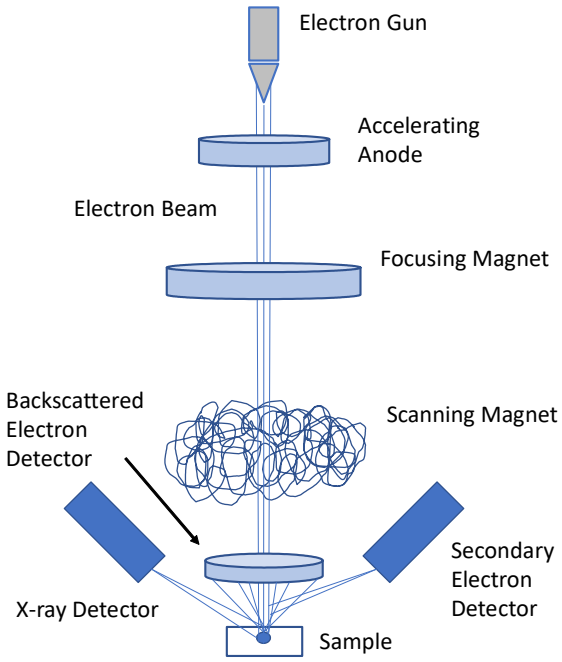

Figure 13: The schematic view of the inner compartments of SEM adapted from Havancsák (2017).

On the other hand, elastically scattered electrons with high energy (> 50 eV) such as BSEs can be called primary electrons, although they have lost some of their energy in previous inelastic scattering as mentioned in Bindell (1992, p. 72). Backscattering depends directly on the atomic number of the target material, so increasing high atomic number elements on the material, the signal due to the backscattering will increase and provide better image brightness and contrast due to the elemental differences. By contrast, in elastic scattering electrons lose some of their energy to, e.g., overall heating of the material, ionization and electronic rearrangement of the target atom as mentioned in Mehta (2012, p. 19).

Inelastic scattering results in larger scattering angles for electrons, which will affect image resolution and contrast. By Bindell (1992, p. 72) the electrons emitted from the target material by inelastic scattering can be referred to as secondary electrons (SE), if their energy is less than 50 eV. This phenomenon mainly happens within the first few nm of the surface of the material. Secondary electrons formed deeper in the sample go through various inelastic collisions which lower their energy and prevent them to exit the material. On the other hand, also secondary electrons can be used for imaging as mentioned in Mehta (2012, p. 21).

The third imaging method in SEM is elemental X-ray mapping, where an excited core electron is ejected from the atom by the primary electron and then decayed to its ground state by emitting either an Auger electron or a characteristic X-ray photon (Bindell, 1992, p. 73). These X-ray photons can be separated by energy in EDS or by wavelength with an electron probe micro-analyzer (EPMA). The SEM is able use the signals from the X-ray photons to create elemental images, X-ray maps, to present the spatial distribution of elements on the target material.

The collection of scattered electrons on detectors can be used to modify the brightness of a cathode ray tube (CRT), which produces the image of the target material on the CRT (Bindell, 1992, pp. 71-72). The *x*- and *y*- inputs on the screen are synchronized with the voltages on the *x*-*y*-coordination axes rastering the electron beam. Therefore, if the amplitude of the voltage applied to the *x*- and *y*-deflection amplifiers is reduced by factor *x* and the CRT voltage is kept constant, then magnification on the screen will increase by the same factor *x*. The CRT is included in the screen control in Figure 13.

According to Bindell (1992, pp. 78-80) SEM microscopy is a rather easy and simple method regarding sample preparation. It only needs samples, which are vacuum compatible, conductive, and fit onto both the stage and specimen chamber of SEM. There are various methods available to measure insulators, large forensic samples and metals with SEM, e.g., by using different coatings, adjusting accelerating voltages or producing larger scale stage-vacuum chamber combinations. Poorly conductive samples such as cellulose (Zhao et al., 2007) and microcrystalline cellulose (Tobyn, McCarthy, Staniforth, & Edge, 1998) can be coated with thin film of carbon, gold or other metals to increase the conductivity of their surfaces. On the other hand, uneven coating or agglomeration of the coating material may decrease the quality of the image and cause distortions and artifacts in it as mentioned in Bindell (1992, p. 78).

3.3 Particle size measurement

Particle size measurement plays an important role in two main fields: earth sciences and powder technologies, which include various specific areas of industries and researches such as petroleum industry, agriculture, chemical industry and biomedical research (Syvitski, 2007, p. 1). Other closely related fields are, e.g., military research, mining industry, paint industry and industrial incineration. Lee Black, McQuay and Bonin (1996) emphasizes also research and industry on combustion, medicine and pharmaceuticals as well as meteorology, powder metallurgy and pollution monitoring as primary users of particle sizing methods.

According to Matthews (2007, p. 34) particle size measurements focus on determining the particle size distribution of granular material to reveal the conditions, such as the chemical and physical conditions of erosion, affecting the material´s occurrence. Moreover, it provides a method to estimate granular material´s industrial utilization and development possibilities (Syvitski, 2007, p. 1). Lee Black et al. (1996) states that particle size measurements provide also information on number density, droplet evaporation rates and total particle burnout as well as on radiative heat transfer, particle dynamics and characterization of two-phase flows. Moreover, particle size measurements can be used in, e.g., quality control of medical fluids, studies of respiratory illnesses and quality assurance of industrial product streams.

As reported by McCave and Syvitski (2007, p. 4) particle size measurements can be conducted by classical methods, such as particle counting, sieving and settling, and by new methods including developed imaging and different spectroscopies, e.g., laser diffraction spectroscopy, photon correlation spectroscopy and acoustic techniques (Syvitski, 2007, p. 1). On the other hand, Lee Black et al. (1996) divides particle size methods to physical methods, e.g., sieving and sedimentation, imaging, e.g., holography and photography and to light scattering, e.g., single particle counting through polarization and dynamic light scattering.

Laser-based techniques are widely used in the research of microcrystalline cellulose (e.g., Vanhatalo & Dahl, 2014; Vanhatalo, Lundin, Koskimäki, Lillandt, & Dahl, 2016; Vanhatalo et al., 2016) as well as in industries (Lee Black et al., 1996).The laser diffraction technique used for particle-size measurements of MCC is able to measure particles of various shapes and sizes such as transparent particles, nonspherical particle and reacting particles and still have high accuracy and high size range (Lee Black et al., 1996, Table 4).

According to McCave and Syvitski (2007, p. 16), laser diffraction spectroscopy is based on the diffraction of applied light on the particle of certain size through a certain angle. This angle is inversely proportional to the size of the particle. The light source produces a beam of monochromatic light, which is directed to the sample cell with lenses. Particles in the sample cell scatter the light according to their particle size, regardless of their movement. The diffracted light is collected in a multielement ring detector, which measures the angular distribution of the light intensity and delivers the information of the stable diffraction patterns through receiver to processing system as mentioned in McCave and Syvitski (2007, pp. 16-17) (Figure 14).

Although the technique is rapid and accurate, it still has some disadvantages on giving incorrect modes in the frequency curve, indication of submicron materials and inaccurate polymodal distributions. As stated in Lee Black et al. (1996) laser-based methods share common issues in Gaussian intensity profile across the laser beam diameter, the scattering characteristics of the particle and measurement environment as well as in both accuracy and consistency of the measurement due to changes in particle type and flow conditions during measurements.

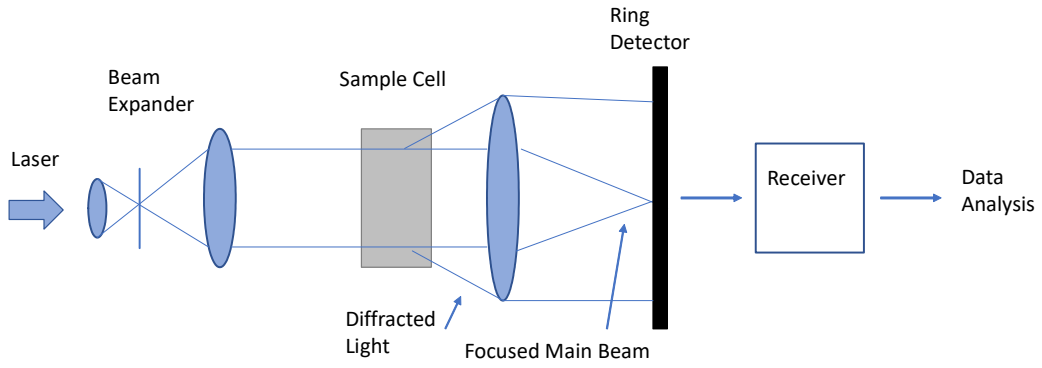

Figure 14: A basic model of laser particle analyzer adapted from McCave and Syvitski (2007, p. 17).

Laser-based particle sizing is based on several theories, e.g., Lorenz-Mie theory, generalized Lorenz-Mie theory, Fraunhofer theory and geometrical optics (Lee Black et al., 1996). These models describe the light-particle interactions giving explanations to scattering and diffraction behaviour of light and thus a physical basis for different methods. The Lorenz-Mie

theory connects particle scattering to its diameter forming the basis for measuring scattered light intensity through optical instruments. Its major assumption includes plain light waves and spherical particles as well as uniform illumination.

On the other hand, generalized Lorenz-Mie theory was created to overcome problems associated with the particle size reaching the same order as the light beam cross-section and thus causing errors in particle-size determination (Lee Black et al., 1996). Unlike in the Lorenz-Mie theory, its assumption is based on arbitrary beam intensity profile. This makes it possible to do measurements on changing intensity distribution across the laser beam. Compared to Lorenz-Mie theory, it gives more accurate results on particles approaching the diameter of the beam waist at the expense of time consuming calculations.

On the other hand, the Fraunhofer theory describes the scattering pattern of light produced by a large particle (Lee Black et al., 1996). This unique pattern is composed of a series of light and dark concentric bands that decline in intensity with rising radial position, which create individual functions of particle size and particle size distribution regardless of the optical properties of the measured material. Practically these functions can be measured by analyzing the scattered light intensity at numerous radial locations in the focal plane. Anomalous scattering due to transmitted light and its effect on the diffraction pattern need to be accounted for sizing significantly small particles with Fraunhofer diffraction.

The oldest theory of characterization of particle size with light is geometrical optics, which approximates previously mentioned exact theories (Lee Black et al., 1996). Like the Fraunhofer theory, it is suitable for large particles close to the size of the beam waist. Geometrical optics are fundamentally a simplified ray-tracing technique, in which light waves are seen as rays of light following the rules of reflection and refraction. Unlike the Lorenz-Mie and general Lorenz-Mie theories, this theory can be used in characterization of known shapes of nonspherical particles. Moreover, geometrical optics is used as complementary with the Fraunhofer theory to describe comprehensively and rather simply the light scattering behaviour by a particle.

3.4 Gel permeation chromatography

Modern size-exclusion chromatography (SEC) is based on liquid chromatography, where the size range of the solute molecules separated is determined by porous packing material and its pore size (Striegel, Yau, Kirkland, & Bly, 2009, p. 1). The liquid sample is placed on the column, where separation takes place as frequent exchange of the molecules between the mobile phase and liquid phase of the packing material. Traditionally SEC has been divided into gel filtration chromatography (GFC) and gel permeation chromatography (GPC) depending on the mobile phase and solvents used. Aqueous mobile phases and solvents have been previously used in GFC, whereas organic ones have been used in GPC. However, variations in column packing materials and use of mobile phases have been closing the gap between GPC and GFC.

Gel permeation chromatography was originally developed in 1964, when the separation properties of cross-linked polystyrene gels of synthetic polymers in organic solvents were revealed (Striegel et al., 2009, pp. 2-3). Since GPC has been used to determine molar mass and molar mass distribution of sample molecules with few limitations on low pressures, slow flow rates and retention time due to conventional fragile packing material. However, modern SEC has overcome these problems with development of more rigid porous packing materials from highly cross-linked polystyrene gel such as styrene-divinylbenzene copolymer (Potthast et al., 2015), porous silica and alumina.

GPC equipment has mainly three detection systems used: concentration-responsive detectors, structure-responsive detectors and molar mass-responsive detection systems as stated in Potthast et al. (2015). These detectors or detector systems include refractive detectors for determination of concentrations, UV-detectors to detect, e.g., residual lignin in unbleached cellulose, IR-detectors as well as fluorescence detectors, light scattering detectors, viscosity detectors etc. From these methods, the light scattering detection, especially multi-angle laser light scattering (MALLS) (Figure 15), right-angle light scattering (RALS), low-angle light scattering (LALS) and triple-angle light scattering are the prevailing techniques.

Cellulose GPC measurements have two principal approaches: derivatization of cellulose hydroxyl groups with phenylisocyanate to cellulose tricarbanilates and direct dissolution of the cellulose with N,N-dimethylacetamide (DMAc) consisting of small amounts of LiCl (8-9 %) (Potthast et al., 2015). The latter method was used in the GPC-measurements done in this

research. During the GPC analysis, cellulose molecules are separated by their hydrodynamic volume on a suitable gel. Other interactions affecting the separation are, e.g., adsorption, ion exchange, electrolyte effects, secondary effects and non-entropic interaction, especially in the DMAc/LiCl-system (0,5-0,9%).

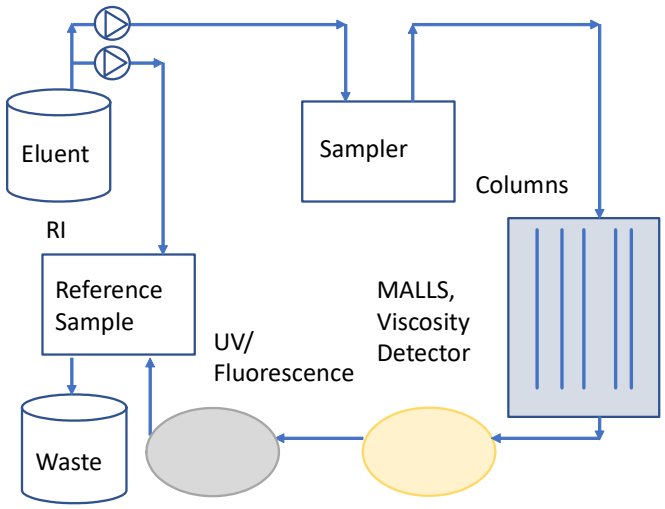

Figure 15: A GPC set-up with various detectors adapted from Potthast et al. (2015).

The use of DMAc/LiCl to dissolve polysaccharides was already invented in 1977 and ever since it has been the major system to analytical measurements in homogeneous solutions as stated in Potthast et al. (2015). This method needs an activation procedure, in which the cellulose goes through solvent exchange, freeze-drying or thermal treatment to transport DMAc or DMAc/LiCl inside to the cellulose structure by changing the morphology or the supermolecular structure of cellulose. Due to the modelled speciation of lithium and chloride, the Li^+ ion coordinates with the carbonyl oxygen of DMAc forming macrocations $[(DMAc)_xLi]^+$. The stability of these macrocations is thought to be essential to the dissolution of cellulose as mentioned in Potthast et al. (2015).

Characterization of cellulose and hemicelluloses as well as other polysaccharides is a noticeable commercial task as stated in Striegel et al. (2009, p. 326). Both Striegel et al. (2009, p. 326) and Potthast et al. (2015) emphasize the wide and complicated hydrogen bond network structure of cellulose limiting its solubility in standard solvents used in SEC. According to Potthast et al. (2015) the prevalent organic solvents used in GPC are, e.g., THF, toluene, acetone and DMAc/LiCl, in which the cellulose sample needs to be dissolved.

The network structure of cellulose also governs other properties of cellulose than its solubility as mentioned in Potthast et al. (2015). These other properties are, e.g., chain length, chemical behaviour and occurrence in certain polymorphs. Other factors affecting these characteristics of cellulose are natural origin, processing history and provenance, all which affect the parameter of MMD. MMD stands for a molar mass distribution function, which is one of most important parameters describing chain length of cellulose in SEC methods.

Typical parameters used in SEC to determine MMD are the number average molar mass (M_n), the weight-average molar mass (M_w) and the z- and (z+1)-average molar masses (M_z, M_{z+1}) as shown in Eq. 1 to 4 (Potthast et al., 2015), where n_i describes the number of each molar mass M_i:

$$M_n = \frac{\sum(n_i M_i)}{\sum n_i}, \quad 1.$$

$$M_w = \frac{\sum(n_i M_i^2)}{\sum(n_i M_i)}, \quad 2.$$

$$M_z = \frac{\sum(n_i M_i^3)}{\sum(n_i M_i^2)}, \quad 3.$$

$$M_{z+1} = \frac{\sum(n_i M_i^4)}{\sum(n_i M_i^3)}. \quad 4.$$

The first describes directly the degree of polymerization of the polymer as well as the separation efficiency of the column and the presence of low molar mass material (Potthast et al., 2015). It depends also on the baseline and the peak limit settings in the original chromatograms. By contrast, the second parameter is less dependent on those settings and reflects high molar mass parts. On the other hand, the last two parameters underline changes in the highest molar mass region as seen in Eq. 3 and 20.

Moreover, the dispersity index ($Đ_M$) describes the weight-average molar mass (M_w) divided by the number average molar mass (M_n) as shown in Eq. 5:

$$Đ_M = \frac{M_w}{M_n}. \qquad 5.$$

The dispersity index measures the non-uniformity of the sample, since the closer its value comes to 1, the narrower MMD is. High numbers of $Đ_M$ then reflect broader MMD and higher non-uniformity of the sample as stated in Potthast et al. (2015).

3.5 High performance anion exchange chromatography

The complex structure and heterogeneity of carbohydrates, such as cellulose and its conjugates, presents challenges for the analysis on high performance liquid chromatography (HPLC) as mentioned in Yan (2014, p. 1). Fortunately, several operational modes of HPLC have been invented to overcome these problems, e.g., reversed phase chromatography (RE), hydrophilic interaction chromatography (HIC) and high performance anion exchange chromatography (HPAEC). On the other, traditional HPLC is based on the separation of compounds by their different partition properties, which can be modified by changing the composition of the mobile phase or the stationary phase (pp. 6-7). Its major benefits are high resolution, fast analysis, simple automation as well as easy sample injection (Corradini, Cavazza, & Bignardi, 2012).

On the other hand, HPLC has some drawbacks on stability, lifetime of the bonded phases, selectivity and efficiency of the column as well as suitability of the RI- and UV-detection of carbohydrates after HPLC separation (Corradini et al., 2012). These disadvantages have raised interest in HPAEC, which is able to separate all classes of alditols, aminosugars, mono-, oligo- and polysaccharides by their structural properties such as size, composition, anomericity and linkage isomerism as specified in Corradini et al. (2012). HPAEC was first mentioned in Rocklin and Pohl (1983), who invented an alternative method to used chromatography techniques such as gas chromatography and acidic cation exchange.

High-performance anion-exchange chromatography is able to separate neutral carbohydrates by using their properties as weak acids with pK_a values between 12-14 (Corradini et al., 2012). At high pH values the hydroxyl groups of carbohydrates turn partially, e.g., <5 %

(Rohrer, Basumallick, & Hurum, 2013), or fully into oxyanions, which can be selectively eluted in a single run in HPAEC using quaternary-ammonium-bonded pellicular anion-exchange columns as specified in Corradini et al. (2012). Characteristics to these columns is the retention being indirectly proportional to pK_a values.

HPAEC is commonly used with pulsed amperometric detection (PAD), in which the detection takes place at a solid anode, e.g., gold or platinum under alternated positive and negative potential pulses (Corradini et al., 2012). This alternation of pulses reactivates the used electrodes that have adsorpted oxidation reaction products on their surfaces by a repetitive three-step waveform as shown in Figure 16. This waveform allows electrodes to be purified by oxidative (E_{oxd}) and reductive (E_{red}) cleaning of adsorbed products to maintain reproducible detection of polar aliphatic compounds. The actual detection (E_{det}) occurs when analyte carbohydrates oxidize on the surface of the working electrode in highly alkaline solution generating a current to be measured according to Rohrer et al. (2013). This analyte integration current results measured charge which is directly proportional to the rate of the oxidation reaction as stated in Corradini et al. (2012).

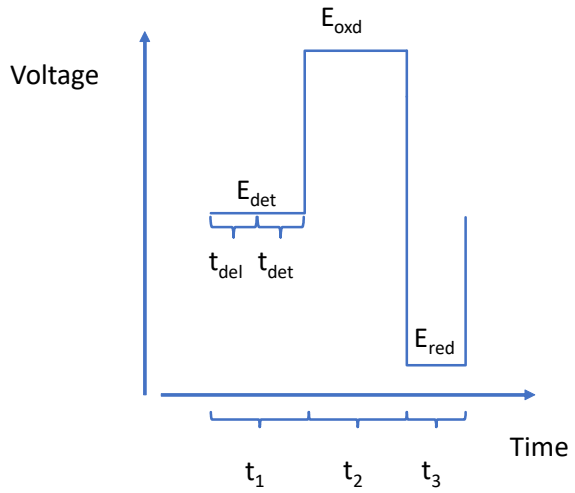

Figure 16: A three-step waveform in PAD adapted from Corradini et al. (2012).

On the other hand, the disadvantages of this method such as electrode corrosion and long-term reproducibility has been overcome with a quadruple-potential waveform, in which the negative and positive cleaning of the electrode happens without electrode corrosion

(Corradini et al., 2012). It causes decreased transport of the analyte to the electrode and reduces electrode response. Other advantages of this new waveform are greater signal-to-noise ratio and long-term reproducibility than in the three-step waveform. Other improvement of the HPAEC technique are the evolution of the disposable gold electrodes, development of waveforms and introduction of faster separations (Rohrer et al., 2013) as well as the use of parallel on-line detection methods as shown in Figure 17.

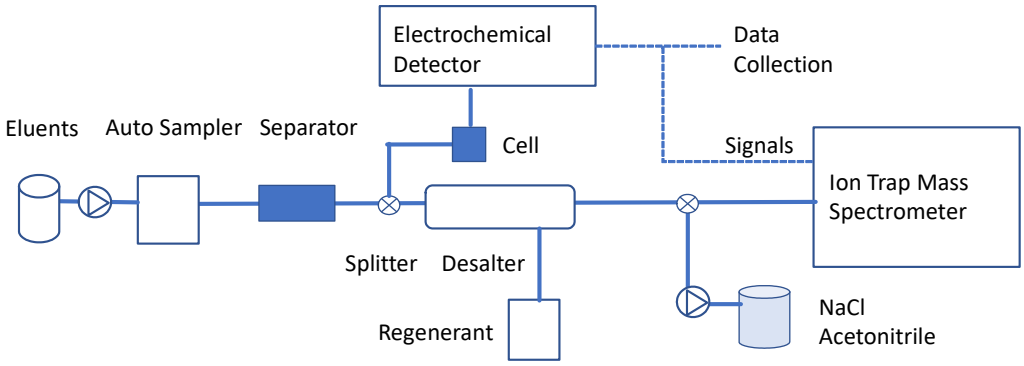

Figure 17: An example of capillary HPAEC combined with parallel PAD and MS adapted from Bruggink et al. (2005).

Moreover, the combination of HPAEC-PAD is used in the analysis of, e.g., glycoproteins in biopharmaceutical industry (e.g., Rohrer et al., 2013), mixtures of sugars, oligo- and polysaccharides in food industry (e.g., Corradini et al., 2012; Mechelke et al., 2017) as well as in the analysis of carbohydrate and lignin content of microcrystalline cellulose (e.g. Vanhatalo et al., 2016) and in the characterization of SEC fractions in biopolymer industry (e.g., Griebl, Lange, Weber, Milacher, & Sixta, 2005), all without any analyte derivatization according to Rohrer (2013).

Besides pK_a values, other important parameters in HPAEC separation are the number of hydroxyl groups, anomerism, positional isomerism and the DP (Corradini et al., 2012). The characteristics of applied mobile phase and used detectors have major effects on the method as well. There are two common mobile phases in HPAEC-PAD; sodium or potassium hydroxide and sodium acetate, which are either used separately (only hydroxides) or mixed (Rohrer et al., 2013). Combinations of these mobile phases make separations of large and charged carbohydrates possible, whereas hydroxides are only suitable for separation of monosaccharides up to tetrasaccharides and their sugar alcohols.

3.6 X-ray photoelectron spectroscopy

In various industries, e.g., energy-, medical- and automotive industries, as well as in different fields of research, e.g., biosciences, adhesion research and polymer research, characterization of the surface composition and speciation of matter enables tailoring the properties of the matter and developing new technical inventions (Van der Heide, 2012, p. 3). There are few techniques capable of defining the chemical composition over the outermost surface of a solid such as, e.g., tomographic atom probe (TAP), secondary ion mass spectrometry (SIMS), surface-enhanced Raman spectroscopy (SERS), energy-dispersive X-ray analysis (EDX), total reflection X-ray fluorescence (TXRF), ultraviolet photoelectron spectroscopy (UPS), Auger electron spectroscopy (AES) and X-ray photoelectron spectroscopy (XPS) (pp. 189-190).

Of the few available, XPS, originated from Hertz (1887), is the most used electron spectroscopy for determining the elemental composition of the solid´s surface within the first 10 nm or less as stated in Van der Heide (2012, pp. 5-6). It is capable of identifying and quantifying elements from Li-U, revealing the speciation of the observed elements as well as obtaining information with simple and easy sample preparation. However, the development of XPS as a surface analytical technique did not begin until late 1960s, when the first instrument to carry out speciation analysis by analyzing core photoelectron emissions was constructed by Siegbahn and Nordling (1967) (as cited in Van der Heide, 2012, p. 7). Since then, the main challenge has been the development of necessary vacuum conditions mandatory for surface region analyses in XPS.

The physical basis of XPS comprises photoelectron production, in which an electron is ejected from an atom/ion by a massless photon through a complete energy transfer (Van der Heide, 2012, p. 7). If the energy of the photon is sufficient, the electron is emitted during the annihilation of the photon (Figure 18). The kinetic energy of the emitted electrons is assumed to be close to 100 eV in the illustration. The kinetic energy of the emitted electron is of a discrete nature and reveals the specific element and environment of the electron by being a function of the electron binding energy (Van der Heide, 2012, p. 7).

On the other hand, the photoelectron emission includes two de-excitation processes, Auger emission and fluorescence, which cause dissipation of the formed core hole by emission of Auger electrons and/or photons by fluorescence. The photoelectron and the Auger electron

emissions and the basic model of XPS are shown in Figure 19 and Figure 20. The three most common data formats shown in Figure 20 include energy distributions, spatial distributions and depth distributions of certain electron emissions (p. 9). Practically, the analysis is performed by collecting energy spectra over all available energies and then focusing on certain photoelectron signals. The technique can identify and analyze elements if their abundance is > 0,05 atomic % (p. 10).

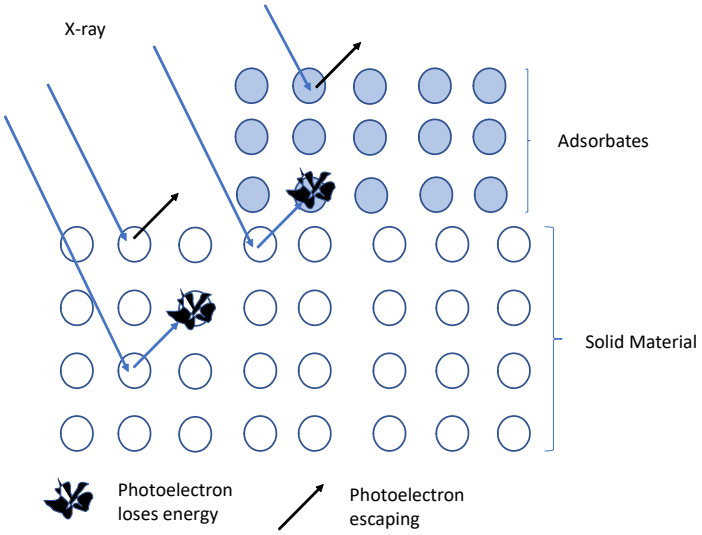

Figure 18: An illustration of photoelectron emission from a solid sample adapted from Van der Heide (2012, p. 11).

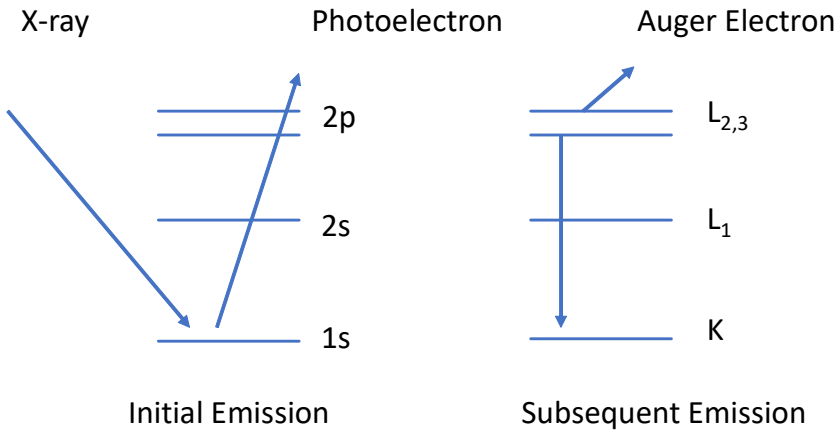

Figure 19: The photoelectron and Auger emission process adapted from Van der Heide (2012, p. 8).

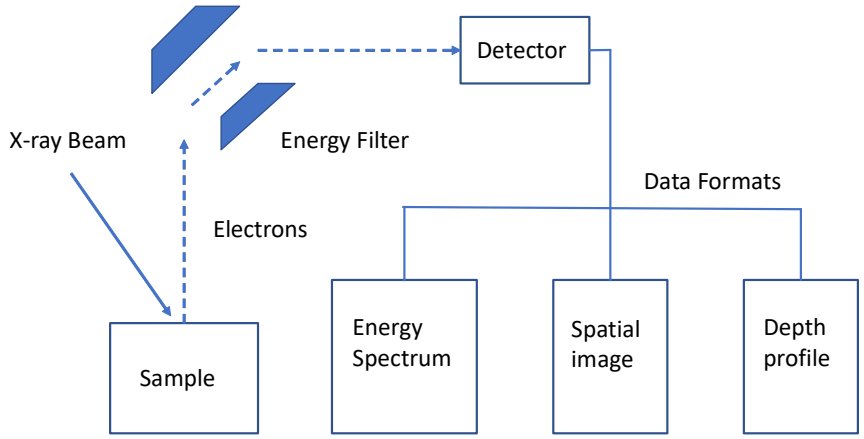

Figure 20: The schematic example of XPS instrumentation and data presentations adapted from Van der Heide (2012, p. 8).

The main parameters of XPS are surface specificity and sensitivity as mentioned in Van Der Heide (2012, pp. 10-11). Surface specificity describes the ability to separate the signal of a photoelectron from a certain region related to the spectral background, which depends on the flight path of the photoelectron in a solid. On the contrary, sensitivity describes the relations between photoelectron cross section and spectral background level. Moreover, the photoelectron cross section is determined by the yield of electrons produced as a function of collided photon energy as described in Van Der Heide (2012, p. 11). As a result, these parameters are dependent on the applied vacuum, which can alter the flight paths of photoelectrons migrating from the surface of the solid and cause contaminant overlays with high pressure.

3.7 Gamma radiation spectroscopy

Gamma radiation is electromagnetic radiation emitted by either de-excitation of nuclei reflecting the energy levels of the daughter nucleus, annihilation of positron and electron or by nuclear reactions such as combining α-emitter with the appropriate target or the absorption of thermal neutrons by suitable nuclei (Knoll, 2010, pp. 10-13). The main interaction mechanisms of gamma radiation from the viewpoint of radiation measurements are photoelectric absorption, Compton scattering and pair production (Knoll, 2010, p.47).

Generally, gamma radiation has neither charge nor it creates direct ionization or excitation path passing through a material (Knoll, 2010, pp. 321-322). Thus, the measuring of gamma-ray photon is based on the partial or full energy transfer of the photon to an electron in the conversion medium. This fast electron created loses its energy by ionization and excitation of atoms and through bremsstrahlung emission, which can be then measured with a conventional detector via complete electron absorption.

For example, the main interaction in a NaI(Tl) scintillation crystal for low-energy gamma radiation is photoelectric absorption, e.g., ^{57}Co with 122 keV γ-photon with intensity of 86 % (The lund/LBNL nuclear data search.1999). This mechanism is based on liberation of photoelectron from the absorber atom´s electron shell by full energy-transfer of the γ-photon as stated in Knoll (2010, pp. 322-323). The relatively high atomic number of iodine (Z = 53) makes possible high the probability of photoelectron absorption corresponding to high intrinsic detection efficiency and large photofraction as mentioned in Knoll (2010, p. 338).

On the other hand, the Compton scattering takes place in gamma ray energies between several hundred keV and below 5-10 MeV, between prevailing photoelectron absorption and pair production energy areas (Knoll, 2010, p. 322, 48). Compton scattering is relevant for, e.g., ^{134}Cs with γ-photon energies of 605 keV and 796 keV with intensities of 98 % and 86 % as well as for ^{85}Sr with 514 keV γ-photon with intensity of 96 % (The lund/LBNL nuclear data search.1999). Compared to photoelectron absorption, Compton scattering produces a recoil electron and scattered gamma-ray photon (Knoll, 2010, pp. 323-324). The energy division of these two depends on the scattering angle, creating a continuum of the electron´s energies in normal conditions, where all scattering angles occur in the detector.

Besides NaI(Tl) scintillation crystal, other suitable detectors for measuring gamma radiation are semiconductor detectors and high-pressure gas-filled detectors (Knoll, 2010, pp. 321-322). There are also newer and more efficient scintillators available like BGO and $LaBr_3$(Ce) (Knoll, 2010, p. 338). From these detectors, NaI(Tl) remains still commonly used, although it has some drawbacks on the light yield, the nonlinearity of energy, the energy resolution and the decay time. On the other hand, it offers high efficiency detection for γ-radiation and adequate energy resolution for separating different energies from polyenergetic samples. Moreover, it is seen as a rather inexpensive detector with a good alteration of size and widespread availability (Knoll, 2010, p. 338).

The mechanism of NaI(Tl) scintillator as well as other inorganic scintillators is based on producing light through de-excitation of electrons. This process depends on the crystal lattice of the scintillation material, especially on the band gap between excited electrons in the conduction band and lattice bound electrons in the valence band. Electrons excited by the absorption of a gamma-ray return to the valence band by emitting a photon. Added activators like thallium modify the crystal lattice and produce recombination centers from which electrons produce visible photon through de-excitation back to valence band (Knoll, 2010, pp. 235-236).

A schematic picture of a solid NaI(Tl) scintillator is shown in Figure 21. According to the schematics, the scintillator´s main components are a scintillation crystal and a photomultiplier tube. The scintillation crystal converts the energy of a gamma-ray photon into visible light through de-excitation process (Knoll, 2010, p. 236). The light is then further directed into the photocathode, where photoemission takes place by producing photoelectrons to the photomultiplier (PM) tube (p. 276). Moreover, the PM tube accelerates the photoelectrons against dynodes, where electrons are multiplied through secondary electron emissions until the amplified charge is collected on an anode and further analyzed by pulse-processing chain (Knoll, 2010, p. 280, 285, 336).

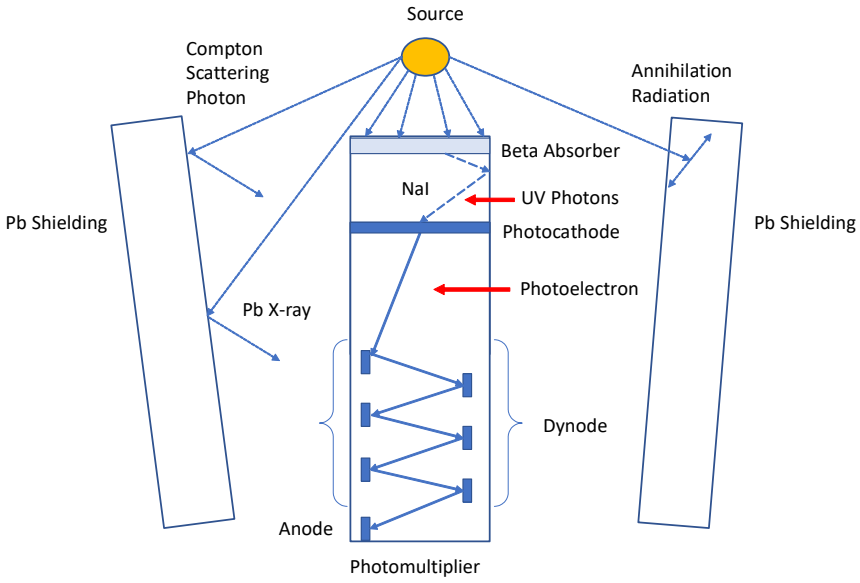

Figure 21: A schematics of a solid NaI(Tl) scintillator adapted from Photonuclear (2017).

3.8 Batch sorption method

The basic mechanism of ion exchange is uptake of solutes called sorption (Helfferich, 1962, p. 7). It describes the distribution of the solute between the pore liquid of the ion exchange material and the solution outside of it. Sorption is mainly a reversible phenomenon, which behavior depends on the solute type, e.g., strong electrolytes may cause a Donnan-type sorption equilibrium, whereas weak and nonelectrolytes aren´t prone to electrostatic forces within the sorption (Helfferich, 1962, p. 125). This sorption equilibria can be described by the distribution coefficient K_d of a solute as in Eq. 6:

$$K_d = \frac{C_s}{C_e}, \qquad 6.$$

where C_s (mol/kg) stands for the concentration of sorbed radionuclide on the solid absorbent and C_e (mol/m^3) for the equilibrium concentration in the solution (Akiba, Hashimoto, & Kanno, 1989). From Eq. 6 the distribution coefficient can be derived to a more practical form as

$$K_d = \frac{R_{std0} - R_{s0}}{R_{s0}} \cdot \frac{V_s}{m_s}, \qquad 7.$$

where R_{std} and R_{s0} (cpm/ml) are the net counting rates of a standard sample and a sample obtained from gamma radiation measurements. Background counting rates are subtracted from the gross counting rates. Other parameters are: V_s describes the volume of the sample (ml) and m_s the dry mass of MCC or other absorbent material (g) added into the sample volume. The quotient of $\frac{V}{m}$ is referred as the batch factor (BF) (Vlasselaer, D'Olieslager, & D'Hont, 1976). Individual gross (g) counting rates of different samples (std = standard, s = sample, b = background) are calculated as

$$R_g = \frac{N_g}{t_g V_g}, \ g \in \{std, s, b\}, \qquad 8.$$

where N represents the counts, t time (s) and V the volume of the sample solution (ml) measured in gamma radiation spectroscopy.

As stated in Helfferich (1962, p. 125-127) the distribution coefficient corresponds to one point on the sorption isotherm, which, on the other hand, describes the dependence of the equilibrium concentration of the solute between the sorbent and the solution. It can also be defined by Brown et al. (1996) as an equilibrium measure of the ability of the solid phase sorbent to remove solute from the solution in certain circumstances and contact time. To measure sorption as a function of pH, some pH adjustments are needed to stabilize the pH to desired value. Taylor (1997, p. 50) states that, for any measurement x, …, z, the sum q and its uncertainty δq are defined as

$$\begin{aligned} q &= x + \cdots + z \\ \delta q &= \delta x + \cdots + \delta z, \end{aligned} \qquad 9.$$

where δx and δz represent the uncertainties of parameters x and z. In addition, the added volume of the pH adjustments, V_{added}, and the uncertainty of each added volume, δ_{V_i}, by pipetting are determined as

$$\begin{aligned} V_{added} &= \sum_{i=1}^{N} V_i\,, \\ \delta_{V_i} &= a_i \cdot V_i, \end{aligned} \qquad 10.$$

where V_i describes the volume added and a_i its fractional uncertainty. Thus, the uncertainty of the added volume is defined as

$$\delta_{V_{added}} = \sum_{i=1}^{N} \delta V_i = \sum_{i=1}^{N} (a_i V_i). \qquad 11.$$

Since $a_i \leq 0{,}14$ (Appendix 1), Eq. 11 may be simplified using $a_i = 0{,}14$ as followed

$$\delta_{V_{added}} \leq \sum_{i=1}^{N} (a_i V_i) = a_i \sum_{i=1}^{N} V_i = a_i V_{added} = 0{,}14 \cdot V_{added}. \qquad 12.$$

According to Taylor (1997, p. 75) the rule of propagation of errors is stated as

$$\delta_U = \sqrt{(\frac{\partial U}{\partial x}\delta_x)^2 + \cdots + (\frac{\partial U}{\partial o}\delta_o)^2}, \qquad 13.$$

where independent random variables x and o are measured with independent and random uncertainties of δ_x and δ_o to define the function $U(x, \dots, o)$ and the uncertainty of U. The uncertainty of the distribution coefficient (Eq. 7) can be then derived to Eq. 14:

$$\begin{aligned}\delta_{K_d} &= \sqrt{(\frac{\partial K_d}{\partial R_{std0}}\delta_{R_{std0}})^2 + (\frac{\partial K_d}{\partial R_{s0}}\delta_{R_{s0}})^2 + (\frac{\partial K_d}{\partial V_s}\delta_{V_s})^2 + (\frac{\partial K_d}{\partial m_s}\delta_{m_s})^2} \\ &= \sqrt{\begin{matrix}\left(\frac{V}{m_s R_{std0}}\delta_{R_{std0}}\right)^2 + ((\frac{V(R_{s0}-R_{std0})}{{R_{s0}}^2} - \frac{V_s}{R_{s0}m_s})\delta_{R_{s0}})^2 \\ +(\frac{R_{std0}-R_{s0}}{R_{s0}m_s}\delta_{V_s})^2 + (\frac{V(R_{s0}-R_{std0})}{R_{s0}{m_s}^2}\delta_{m_s})^2\end{matrix}}\end{aligned}, \qquad 14.$$

where variables, R_{std0}, R_{s0}, V_s and m_s, have uncertainties of $\delta_{R_{std0}}$, $\delta_{R_{s0}}$, δ_{V_s} and δ_{m_s}. The uncertainty of the mass (δ_{m_s}) is defined in Appendix 27 and Table 9 and δ_{V_s} in Appendix 1.

Using Eq. 13, the uncertainty for gross counting rates R_{std}, R_s or R_b from Eq. 8, can be defined as followed:

$$\begin{aligned}\delta_{R_g} &= V_g\sqrt{(\frac{\partial R_g}{\partial N_g}\delta_{N_g})^2 + (\frac{\partial R_g}{\partial t_g}\delta_{t_g})^2 + (\frac{\partial R_g}{\partial V_g}\delta_{V_g})^2} \\ &= V_g\sqrt{(\frac{\sqrt{N_g}}{t_g V_g})^2 + (\frac{-N_g}{t_g {V_g}^2}\delta_{V_g})^2}, \;\; g \in \{std, s, b\}.\end{aligned}, \qquad 15.$$

where δ_{t_g} is assumed to be zero and $\delta_{N_g} = \sqrt{N_g}$ (Taylor, 1997, p. 48). The used gamma counter measures only counts per time, t_g, and per certain given volume, V_g, due to which reason the results of the square root of Eq. 15 giving an uncertainty per milliliter is multiplied by volume of V_g.

The net counting rates for samples excluding background samples are defined as

$$R_{std0} = \widehat{R_{std}} - \widehat{R_b},$$
$$R_{s0} = R_s - \widehat{R_b}, \qquad 16.$$

where $\widehat{R_{std}}$ and $\widehat{R_b}$ are gross counting rate averages of two standard samples (N = 2) and three background samples (N = 3) and R_s is the gross counting rate of a sample. Moreover, these averages can be further determined as

$$\widehat{R_x} = \sum_{i=1}^{N} \frac{R_{x,i}}{N} \quad x \in \{std, b\}. \qquad 17.$$

The uncertainties of averages $\widehat{R_{std}}$ and $\widehat{R_b}$ can then be determined as followed

$$\delta_{\widehat{R_{std}}} = \sqrt{(\frac{\delta_{R_{std,1}}}{2})^2 + (\frac{\delta_{R_{std,2}}}{2})^2},$$
$$\delta_{\widehat{R_b}} = \sqrt{(\frac{\delta_{R_{b,1}}}{3})^2 + (\frac{\delta_{R_{b,2}}}{3})^2 + (\frac{\delta_{R_{b,3}}}{3})^2}, \qquad 18.$$

where $\delta_{R_{x,i}}$ ($i \in [1, N]$ and $x \in \{std, b\}$) stands for individual measurements of either standard or background samples. The uncertainties of net counting rates R_{std0} and R_{s0} can then be determined as followed

$$\delta_{R_{std0}} = \sqrt{(\delta_{\widehat{R_{std}}})^2 + (\delta_{\widehat{R_b}})^2},$$
$$\delta_{R_{s0}} = \sqrt{(\delta_{R_s})^2 + (\delta_{\widehat{R_b}})^2}. \qquad 19.$$

The distribution coefficient as well as the rates of ion exchange determined by diffusion processes can be measured through batch sorption method (Helfferich, 1962, p. 257, 309). In this method a sorbent is contacted with a solution of known volume and solute

concentration in a closed vessel. The ion exchange of solutes takes place during the contact time, in which it is enhanced through agitation such as shaking. Thus, the uptake of the solute is measured as a function of the contact duration, which depends on the purpose of the experiment. For that reason, the contact time may vary from minutes and hours (Loebenstein, 1962) to days (Kautenburger & Beck, 2010) and weeks (Akiba et al., 1989) and even longer. After the contact time, the sorbent is separated from the solution by filtration, after which the filtrated solutions are analyzed through suitable methods such as gamma counting in case of gamma-emitters (Brown et al., 1996).

According to Brown et al. (1996), the batch sorption method is a fast and economical technique, in which the distribution coefficient reflecting the selectivity, capacity and affinity of the solute for the sorbent can be determined under particular test conditions. On the other hand, these test conditions require identical parameters, such as ratio of volume and mass, temperature, duration for comparable results. The batch sorption method can also be used to exemplify the kinetics of the ion exchange by, e.g., providing the contact time needed to achieve equilibrium for further experiments.

3.8.1 The Donnan potential

As mentioned in Helfferich (1962, pp. 134-137) electrostatic forces between the ion exchanger and the solution cause counter-ions, co-ions and electrolytes to move according to the present electric charges. At first, the ion exchanger has a certain charge, opposite of which are the counter ions integrated in the matrix of the exchanger. The added solution has mobile electrolytes of the same charge as the counter ions and co-ions of the opposite charge. Migration of the first charged ions between these phases causes the electric charge of the ion exchanger and the solution to change to opposite as in the beginning. This movement also creates an electric phase boundary potential, the Donnan potential, between the ion exchanger and the solution. The Donnan potential draws the counter ions back to the ion exchanger and pulls co-ions back to the opposite charged solution. At the same time, it also excludes to some extent electrolytes by the ion exchanger since co-ion uptake and electrolyte sorption follow each other. Practically, the effect of this potential can be seen on the decrease of the sorption of the electrolytes.

Moreover, the Donnan potential effects on the distribution of co-ions, which, on the other hand, has an impact on the Donnan-type equilibria. The Donnan potential and the Donnan exclusion depend on the concentration difference between the ion exchanger and the solution, where higher differences and stronger potentials as well as exclusions can be achieved, e.g., by decreasing solution concentration. The Donnan-type equilibria is then achieved, when the Donnan potential balances between the tendency of the counter ions to migrate to the solution. The dependence of the solution concentration causes the distribution coefficient of the co-ions to increase with increasing concentration, creating a strong positive curvature for the sorption isotherms (p. 136).

4 Experimental Work

The purpose of the experimental work was to determine the capability of three different AaltoCell^{TM} materials to sorb the radionuclides of interest. These three different types of microcrystalline cellulose were first produced from bleached softwood kraft pulp, oxygen delignified softwood pulp and unbleached softwood kraft pulp according to the procedures stated in the patents Dahl et al. (2011a) and Dahl et al. (2011b) in the Department of Bioproducts and Biosystems in the Aalto University. The experimental work on AaltoCell^{TM} materials was then conducted in two different places, in the Department of Bioproducts and Biosystems in the Aalto University and in the Department of Chemistry in the University of Helsinki. Thus, the experimental work was divided into two different parts, structural studies and batch sorption experiments .

The structural studies focused on revealing the morphology of microcrystalline cellulose by SEM, the specific surface area by BET, the particle size distribution by laser diffraction, the molecular weight distribution by GPC, the carbohydrate and lignin content by HPAEC-PAD and the surface lignin coverage by XPS. By contrast, the batch sorption experiments focused on the kinetic sorption experiments with a 3-day, a 14-day and a 24-h batch experiments, the sorption as a function of pH and the effect of the ionic strength on the sorption and on the Donnan potential. Only gamma radiation spectroscopy was used in measuring the radionuclides, ^{134}Cs, ^{85}Sr and ^{57}Co, of interest. The methods were chosen to be complementary and mutually supportive.

4.1 Production of microcrystalline cellulose

Microcrystalline cellulose was produced according to the patents Dahl et al. (2011a) and Dahl et al. (2011b) from different softwood pulps received from a Finnish kraft pulp mill. Three different AaltoCell™ materials were made from bleached sulfate pulp (MCC1), unbleached oxygen delignified pulp (MCC2) and unbleached kraft pulp (MCC3), which was retrieved after sulfate cooking. The numbering of the MCC materials was made according to the order of the preparation. The main processes of kraft pulping are shown in Figure 22.

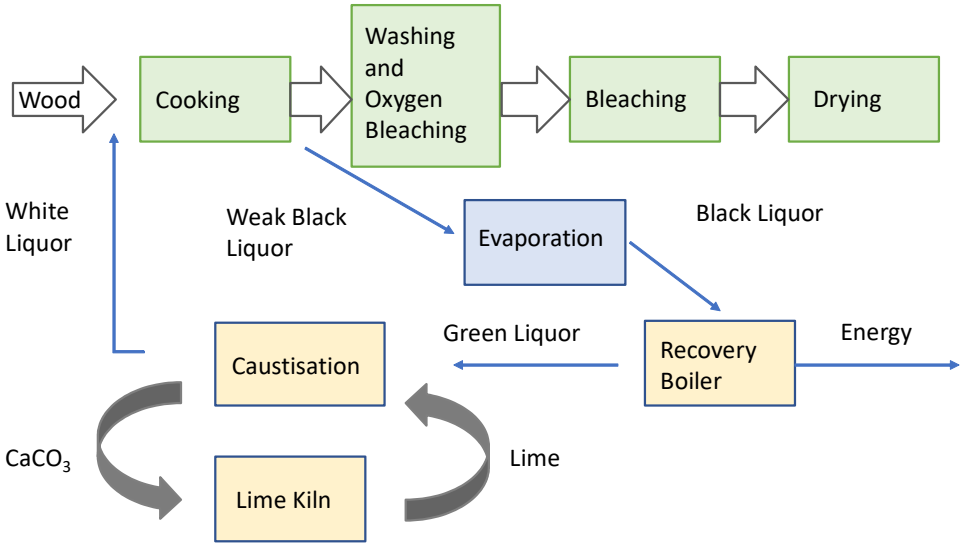

Figure 22: The overview of the kraft process adapted from Staffas et al. (2013, p. 26).

The first AaltoCell™ material (MCC3) was made from the pulp after cooking. Kraft cooking consists usually of NaOH and Na_2S, which cause degradation of almost half of the wood as stated in Alén (2000a, pp. 62-63). The second AaltoCell™ material (MCC2) was prepared from the oxygen delignified pulp, which had gone through cooking, washing and bleaching by oxygen and alkali (pp. 86-87). Oxygen delignification removes significant fraction of the residual lignin in the pulp, in consequence of producing whiter pulp than the cooking. The last AaltoCell™ material (MCC1) was produced from the fully bleached sulfate pulp gained after the bleaching step. The pulp had the highest brightness values compared to the other pulps, due to its lowest concentration of residual lignin (pp. 93-97).

The bleaching is usually performed in multiple stages, where different oxidizing, reducing and auxillary chemicals, washings and process conditions vary according to the delignifying process. From these three samples, only MCC1 was considered lignin-free microcrystalline cellulose, whereas the others had some content of lignin due to their brown color and less intense kraft process. Moreover, each sample had different dry masses due to the variation in structure and contents of lignin and water.

The lignin-free microcrystalline cellulose was prepared from sheets of pulp by cutting them into small pieces. For each reactor the pulp was measured (300 g dry mass) and 46 g 1 M H_2SO_4 (Merck) was added (Figure 23). Deionized water ~ 640 g was added to the reactor to gain consistency of 30 %. The hydrolysis of cellulose pulp was conducted by a made-to-order air bath digester holding six reactors. The air bath digester was pre-heated to 49 ^oC, from which the reactors were brought to the hydrolysis temperature 160 ^oC at a speed of 1 ^oC /min. The hydrolysis took 1 h 56 min, after which the reactors were cooled with a water bath for 20 min (Figure 24).

After cooling, the reactors were opened, and microcrystalline cellulose was poured into a fabric-lined tub. Excess water was centrifuged (10 min, 4500 rpm, Wärtsilä PEKO Centro 42) and the remains were homogenized via the so-called dough machine (12 min, Metos Karhu 93/RN20) (Figure 25). Microcrystalline cellulose was stored in a refrigerated container (+ 4 ^oC) for two days. Next it was washed by deionized water (~ 380 l) until the conductivity of wastewater was 2,1 µS (Orion Model 150) (Figure 26). Microcrystalline cellulose was centrifuged (10 min) and stored in the refrigerated container.

The other microcrystalline celluloses were prepared from brown softwood pulp. The pulp were measured (1,8 kg total dry mass) and pre-ground. 367 g 1 M H_2SO_4 (aq) (Merck) was added and grinding was continued for 5 min (Figure 27). Grinding was made in two lots due to the limited volume of the container. The mixture of pulp and sulfuric acid was poured into the reactors (650 g/each). The hydrolysis was conducted as before with run time of 1 h 58 min and start temperature of 50 ^oC. The consistency of the mixture was estimated to be 30,6 % (MCC2) and 25 % (MCC3). The reactors were cooled in the water bath and centrifuged as before. By contrast, the resulting mass was homogenized further for 2 min and more deionized water was used in washing to achieve conductivity below 5 µS.

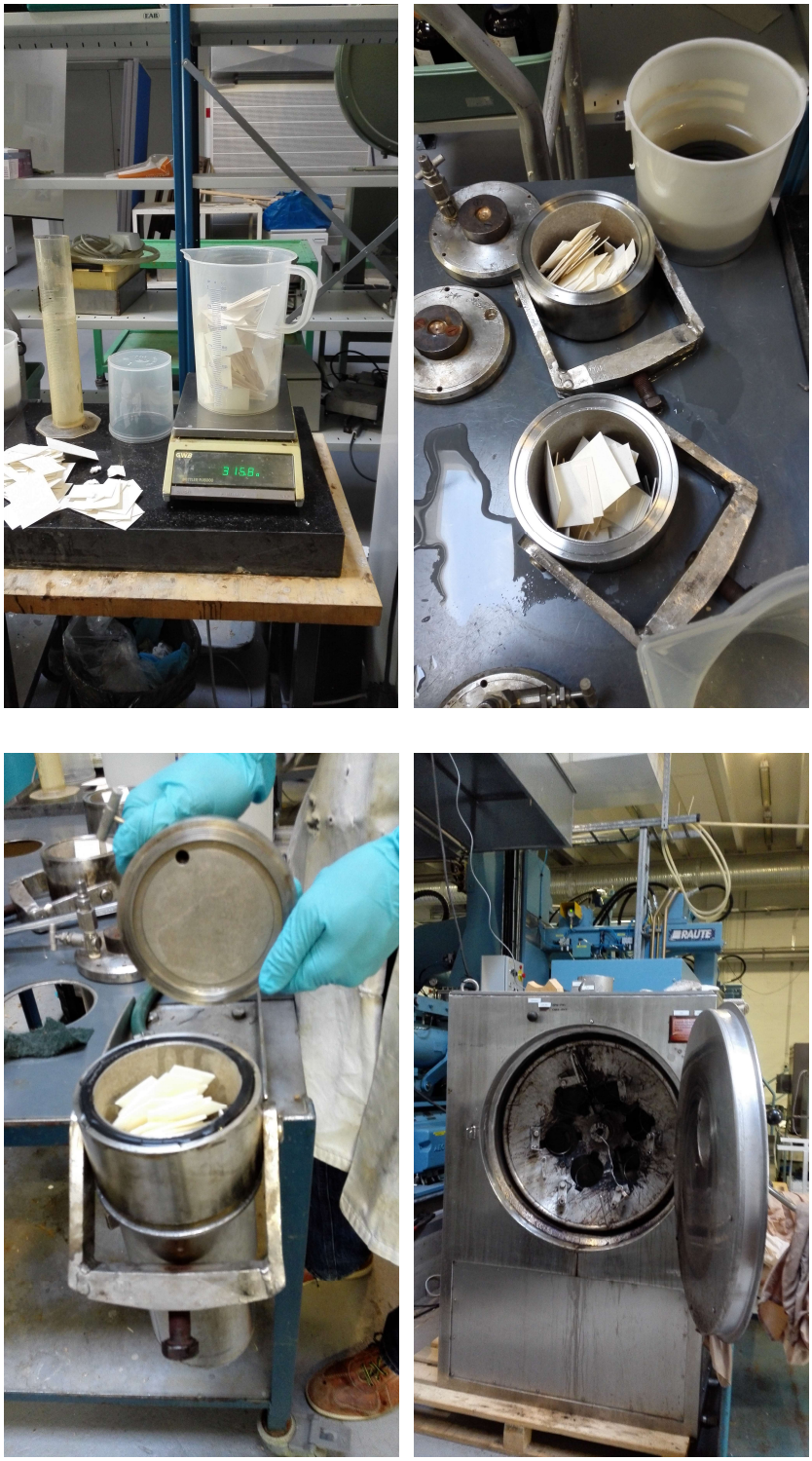

Figure 23: Preparing for hydrolysis of pulp with air bath digestor.

Figure 24: The water bath to cool the reactors after hydrolysis.

Figure 25: Remove of water and homogenization of MCC.

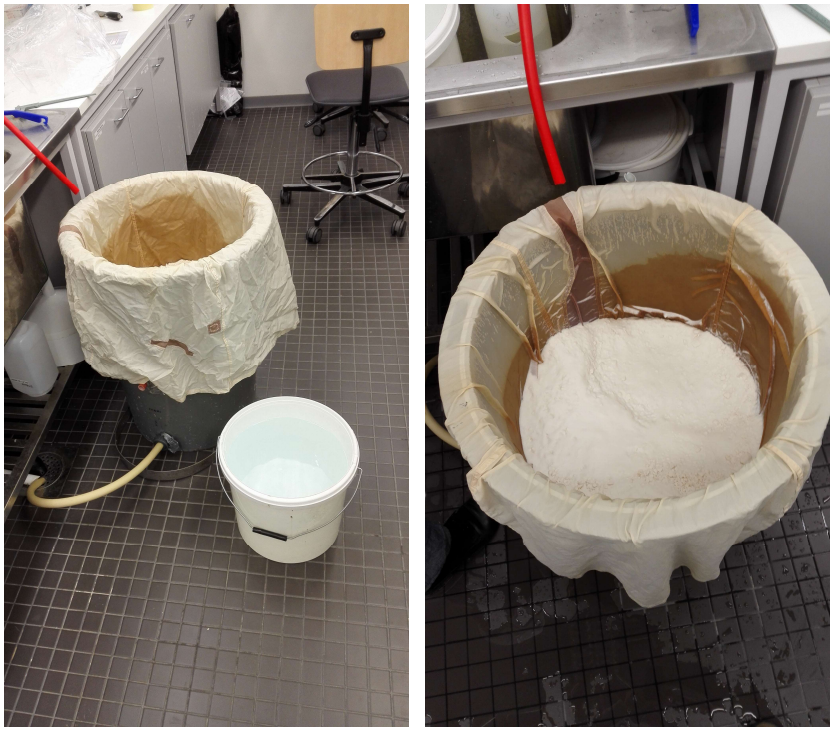

Figure 26: Washing the microcrystalline cellulose (MCC1).

Figure 27: Grinding of the oxygen delignified pulp and its hydrolysis product.

4.2 Morphology of microcrystalline cellulose

First, the dry masses of different MCC samples were determined after several dryings in an oven (105 °C, POL-EKO aparatura) and coolings in desiccators. Then the wet microcrystalline cellulose subsamples (1,5 g dry mass) were subjected to a two-step liquid-displacement using a water-soluble tert-butanol, $(CH_3)_3COH$ (aq), for 45 ml per centrifuge cycle (30 °C, 4000 rpm, 10 min with Centrifuge 5804 R, Eppendorf). After the subsamples were centrifuged 7 times, they were frozen for 3 hours and then allowed to sublimate in freeze-dry conditions for a day with LABCONCO, FreeZone$^{2.5}$ freeze-dryer. MCC samples were prepared to SEM imaging by cleaning the surfaces of the metallic stubs, numbering the sample stubs, adding double side tape to the cleaned surfaces of the stubs, adding small amount of the samples on the tapes and air blowing excess samples from the tapes as discussed in Mehta (2012). The samples were then coated with platinum (Pt) in vacuum (30 mA, 1 min, Emitech K100X, Figure 28) prior to attaching them to the sample plate and placing the plate into the SEM. The set-up for SEM imaging is shown in Figure 29.

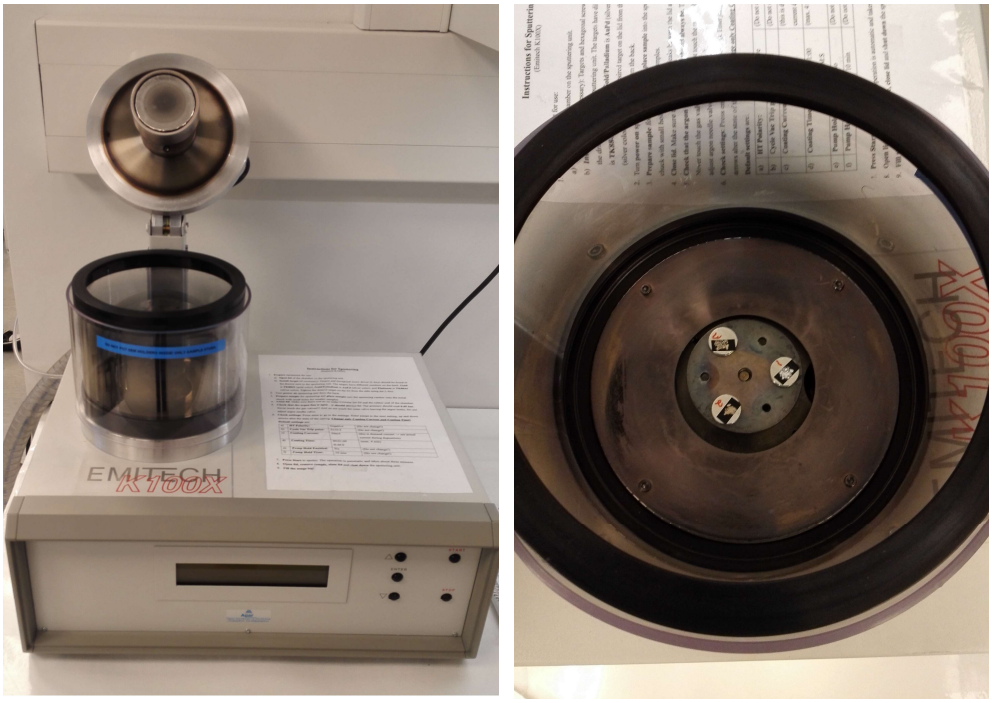

Figure 28: Emitech K100X used for coating the MCC samples.

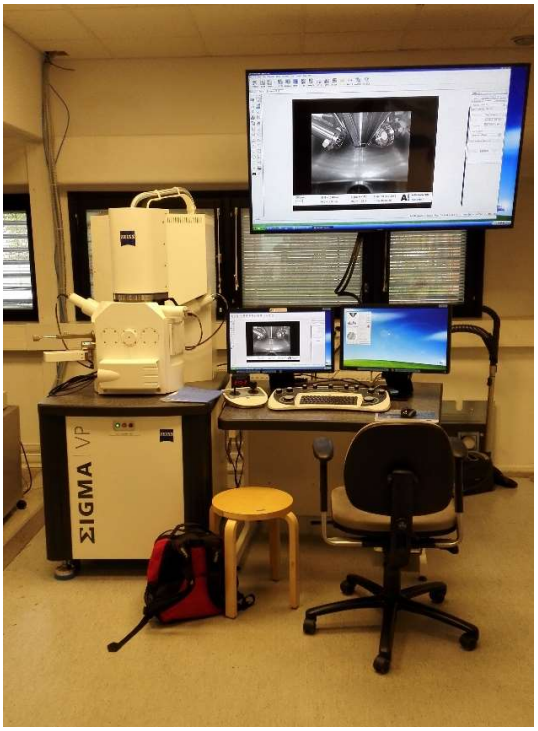

Figure 29: The set-up of SEM measurements.

The information of the SEM is shown in Table 1 (Zeiss sigma VP.2016). It has a variable pressure mode for slightly conductive samples like insulators and Gemini column. Five different types of magnification images were taken from the microcrystalline samples: 70x, 250x, 1000x, 3000x and 10 000x. Taking of the image of 10 000 times magnification for MCC2 was not possible because of burning of the surface of the sample due to high current.

Table 1: Zeiss Sigma VP -instrument with Schottky FEG emitter

Detectors:	In-column SE, ETSE, BSE (5 segments), VPSE, STEM
Resolutions:	1,3 nm at 20 kV, 2,8 nm at 1 kV, 2,5 nm at 30 kV with VPSE-detector
Acceleration voltage:	0,1-30 kV
Probe current:	4 pA-20 nA
Operating modes:	High vacuum (10^{-5} Pa), Variable pressure (2-133 Pa, N_2)

4.3 Specific surface area measurement

The specific surface areas of three microcrystalline cellulose samples (MCC1-MCC3) were measured with BET- instrument (Micromeritics TriStar II 320) by a volumetric method with N_2 as an absorbent (Figure 30). The MCC samples were first freeze-dried as before and oven-dried for three days in 100 ºC (Memmert UE500). Then the samples were weighted (~ 200 mg MCC/glass tube) and pretreated with a sample degas system (Micromeritics FlowPrep 060) with N_2 flow: 15 min in room temperature, 1 h in 150 ºC (MCC1) or 120 ºC (2.-MCC3) and 15 min cooling in room temperature. Each microcrystalline cellulose was measured simultaneously in three parallel sample tubes, which had been oven-dried before pretreatment. Sample tubes were placed on the BET-instrument and the measurements were done using cellulose density 1,553 g/cm^3 and multipoint BET-method as mentioned in Brunauer, Emmett and Teller (1938).

Figure 30: BET-instrument with sample pretreatment equipment.

4.4 Particle size distribution

The particle size distributions of MCC samples were measured by laser diffraction with a particle size analyzer (Malvern Inst. Mastersizer 2000) combined with Hydro 2000MU wet dispersion unit according to Vanhatalo and Dahl (2014) (Figure 31). Samples (~ 1 g) were taken from the refrigerated container, dispersed in 25 ml of distilled water and stirred for an 1 h 17 min (800 rpm). Then the samples were treated ultrasonically (1 min, amplitude 39 %, 20 Hz) with an ultrasonic processor (Sonics & Material Ultrasonic VCX 750). Solutions were pipetted to the dispersion unit and the particle size parameters were determined as average values from two measurements. Distilled water was used as a background solution, which was measured between MCC samples. Measurement time for each MCC and background sample was 5 seconds. Refractive index values applied in the measurements were 1,33 for water and 1,59 for solid material. Absorption index was exceptionally 0,1 for slightly colored powder instead of 0,01, which was used in Vanhatalo and Dahl (2014).

Figure 31: Mastersizer 2000 with MCC samples.

4.5 Molecular weight distribution

Microcrystalline cellulose samples were first air-dried almost over a month (27 d) to dry matter content of 90−95 % (Figure 32) and then ground with a Wiley mill (Figure 33) (Oy Strömberg Ab N:o 25635 B) as in Testova, Chong, Tenkanen and Sixta (2011) and Testova et al. (2014) to powder (Figure 34). The MCC samples were then extracted with acetone in a Soxhlet apparatus (Figure 35) to separate acetone-soluble matter (SCAN-CM 49:03). Extraction thimbles were tared and MCC samples (~ 5 g) and acetone (~ 200-228 g) were added. Extraction time was 4 h, in which the total number of extraction cycles was 16 or more. Extraction thimbles were dried in a fume hood overnight and weighted. The extract (~ 5 ml) was poured into a glass vials of constant weight and dried overnight in a fume hood. The extractives were measured gravimetrically. Dry matter contents of MCC samples were determined before and after acetone extraction as before. Acetone-extracted microcrystalline cellulose samples (~ 50 mg dry mass/MCC) were activated according to Tolonen (2012) and Potthast et al. (2002).

Activation was conducted by adding 4 ml MilliQ-water to each sample placed in a syringe and let it stabilize overnight (Figure 36). Next day the syringes were dewatered, and 2 ml acetone was added. Acetone was shortly removed by vacuum, after which 4 ml acetone was added to stabilize for almost 3 hours. Acetone was again removed by vacuum, after which 4 ml DMAc was added to the syringes over the next three days. DMAc was then removed by vacuum as before, whereas the residue was collected into glass bottles.

5 ml LiCl/DMac (90 g/l) was pipetted on the glass bottles to dissolve the residues under a constant magnetic stirring at room temperature overnight. Next day 0,5 ml sample solution was diluted into 4,5 ml pure DMAc to prepare sample concentration on DMAc (1,0 mg/ml) and LiCl (9 g/l). The diluted samples were filtered with 0,2 µm syringe filters into sample vials. Each MCC sample was measured twice in room temperature and the results were taken as an average. The run was performed by Dionex Ultima 3000 system (Figure 37) with the flow rate of 0,75 ml/min via guard column (PLgel Mixed-A, 7.5 x 50 mm, Agilent Technologies), four analytical columns (PLgel Mixed-A, 7,5 x 300 mm) and RI-detection (Shodex RI-101, Kawasaki) as in Testova et al. (2014). Two different standards (343 Da – 708 kDa, Polymer Standard Service GmbH and 1600 kDa, Fluka GmbH) were used to calibrate the GPC system. Moreover, the molar masses of these standards were optimized to correspond to those of cellulose as stated in Testova et al. (2014).

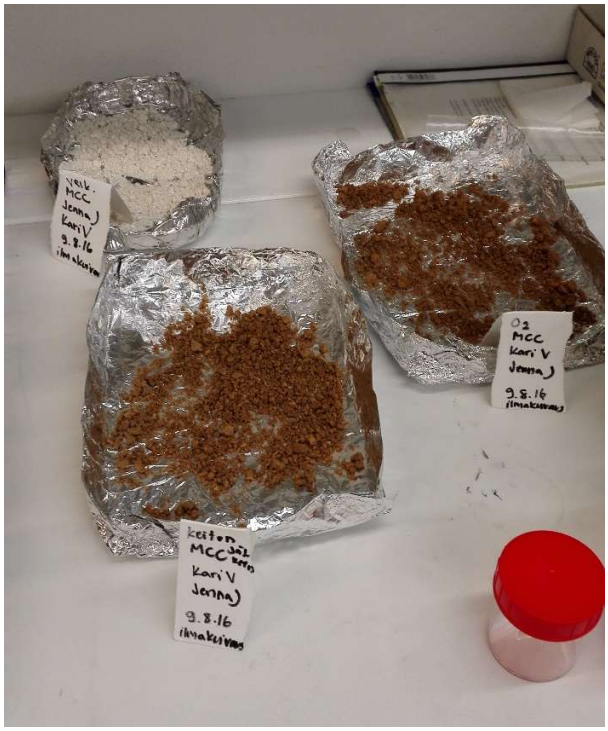

Figure 32: Air-drying microcrystalline cellulose.

Figure 33: Wiley mill grinding.

Figure 34: Ground MCCs in various lignin contents.

Figure 35: Soxhlet extraction of the MCC samples.

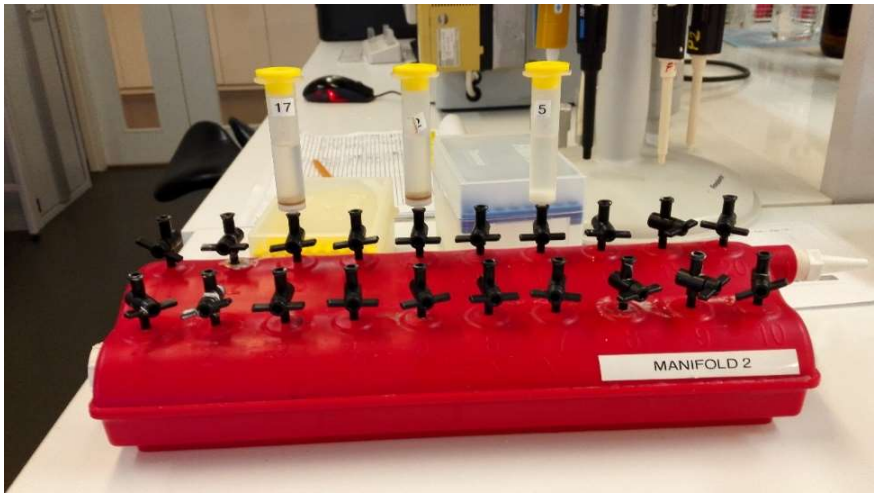

Figure 36: A set-up for the sample activation.

Figure 37: Dionex Ultimate 3000 system.

4.6 Carbohydrate and lignin content

Structural carbohydrates (CH) and lignin were determined according to a National Renewable Energy Laboratory procedure (Sluiter et al., 2008). The filtering crucibles were heated in an oven (105 °C) for a minimum of 4 hours, cooled in a desiccator (≥ 45 min) and measured until constant weight. Parallel acetone-extracted samples were weighted (~ 320 mg MCC) to test tubes and 72 % H_2SO_4 (aq) (3 ml) was added. Each test tube was stirred in every ten minutes for an hour in a water bath 30 °C (Köttermänn, GWB) (Figure 38). Then test tubes were washed into glass bottles by distilled water (83 ml) and autoclaved (Systec DE-23, Figure 39). A standard sample was prepared by adding 20 ml of standard solution (Table 2) and 696 µl of 72 % H_2SO_4 (aq) into a glass bottle for hydrolysis. The hydrolysis was conducted with temperature of 121 °C, reaction time of 60 min and duration of 100 min. The pressure of the hydrolysis was 208 kPa. Cooled samples were filtered through filtering crucibles by vacuum. The first filtrate was discarded, and the rest was collected.

Table 2: The CH concentrations of the standard solution

Name	Arabinose	Rhamnose	Galactose	Glucose	Xylose	Mannose
C (mg/l)	50	50	50	1500	300	400

Figure 38: A set-up for a water bath and six test tubes.

Figure 39: The autoclave with temperature measurement.

The set-up for sample preparation is shown in Figure 40 and the filtering procedure in Figure 41. An aliquot of 1 ml was taken from each solution and diluted up to 100 ml by ion exchanged water. A diluted subsample (1-1,5 ml) was filtered with 0,2 µm filter (PALL GHP acrodisc 13) into a vial for determination of carbohydrates with HPAEC-PAD (Dionex ICS-3000, pulsed amperometric detector, Dionex CarboPac PA20 column) as shown in Figure 42. Each subsample was measured twice, and the results were compared between runs.

Figure 40: Sample preparations for filtering.

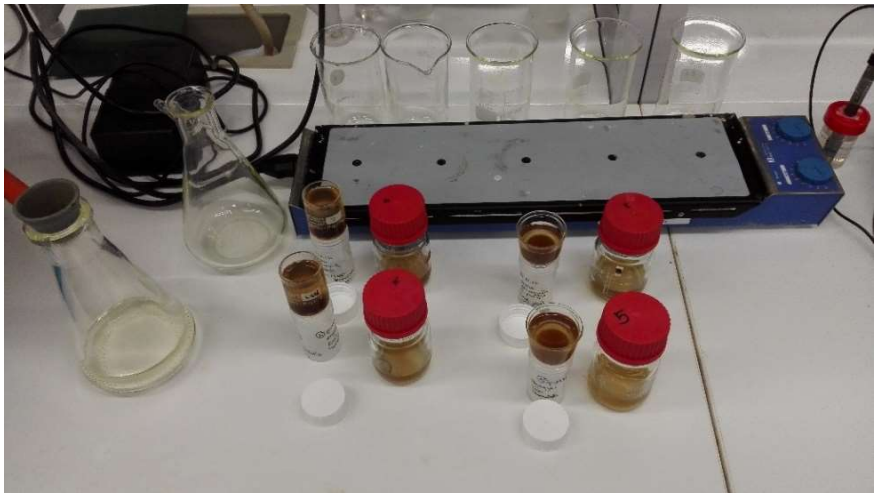

Figure 41: Filtering procedure.

Figure 42: The used HPAEC-PAD chromatography.

The total solids of acetone-extracted MCC samples were determined simultaneously as acid-insoluble lignin from filtering crucibles by drying them in an oven (103 ºC) for two days and measuring them gravimetrically (Figure 43). Acid-soluble lignin was analyzed from undiluted solution from light absorbance at 205 nm with UV/VIS spectrometer (Shimadzu UV-2550) as in Vanhatalo et al. (2016) (Figure 44). Determination of structural carbohydrates and lignin was conducted twice to strengthen the obtained results.

Figure 43: Dried and cooled filtering crucibles.

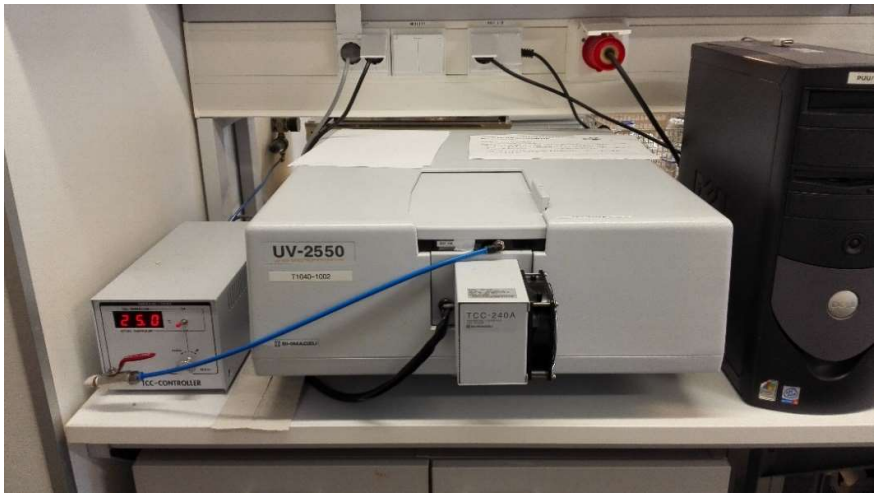

Figure 44: The used UV/VIS spectrometer.

4.7 Surface lignin coverage

The chemical analyses of the surfaces of the microcrystalline cellulose samples were determined with XPS, using AXIS Ultra electron spectrometer (Kratos Analytical) (Figure 45) with monochromatic low power radiation (100 W) and neutralization as in Vanhatalo et al. (2016). Grinded and acetone-extracted microcrystalline cellulose samples were positioned on double-side tape on a metal disk and pre-evacuated several days in a pre-chamber together with *in situ* reference (100 % pure cellulose Whatman filter paper) before the measurement

according to Johansson and Campbell (2004). Data was acquired from two locations for each sample instead of three as in Vanhatalo et al. (2016) due to long measurement times caused by uneven surfaces of the samples. Elemental content of each sample surface was determined from low-resolution surveys whereas cellulose and lignin contents were measured from the high-resolution carbon C 1 s orbital region as mentioned in Vanhatalo et al. (2016). Obtained data were fitted into several Gaussian peaks using CasaXPS software (Casa Software Ltd.) as in Johansson and Campbell (2004).

Figure 45: The used XPS instrument.

4.8 Batch sorption

The batch sorption experiments on MCC were conducted by three major experiment paths of the kinetic sorption, the sorption as a function of pH and the effect of the ionic strength on sorption. The kinetic sorption experiments including a 3-day batch test, a 14-day batch experiment and a 24-h batch experiment were done prior the other paths to determine the kinetic sorption behaviour of microcrystalline cellulose as a function of time as well as the suitable equilibration time for the following experiments. A phosphate buffer solution of pH 7 was used in the experiments of the first path to provide pH-area, where carboxylic acid groups of lignin were ionized (pKa ≈ 4,8) (Scudder, 2013, p. 65) and cobalt was soluble (below pH 8) (Huang, Kargl-Simard, Oliazadeh, & Alfantazi, 2004). By contrast, the experiments on the sorption as a function of pH were made mainly with 10 mM $NaNO_3$ (aq) to

test the effect of Na^+(aq) on sorption. These experiments included several tests on ^{134}Cs, ^{85}Sr and ^{57}Co. The re-test and the last test on sorption as a function of pH for ^{57}Co were made exceptionally with a phosphate buffer. Last, the effect of the ionic strength and the Donnan potential were studied with 0,01 M, 0,1 M and 1 M solutions of $NaNO_3$ (aq) and $NaClO_4$ (aq) in the presence of reactive electrolyte NO_3^- and unreactive electrolyte ClO_4^- (Yoon et al., 2009). The process chart of experiment methods and the measurement step are presented in Figure 46 and Figure 47. The method of each individual experiment is explained in detail in the following chapters and in generally in Appendix 2.

The efficiencies used for determining suitable activities for used solutions were 90 % for ^{57}Co, 30 % for ^{134}Cs and 8 % for ^{85}Sr (PerkinElmer, 2002, p. 136). By contrast, the efficiencies for each radionuclide were checked on the screen of Wallac 1480 WIZARD 3" gamma counter, which gave 90 % for ^{57}Co, 30 % for ^{134}Cs and 25 % for ^{85}Sr. The difference in the efficiency value of ^{85}Sr could have been due to random coincidence summing as mentioned in Shweikani, Hasan and Takeyeddin (2013). After the batch sorption experiments, the counting efficiencies were determined for each radionuclide and the results were 87% for ^{57}Co, 40 % for ^{134}Cs and 30 % for ^{85}Sr (Appendix 3).

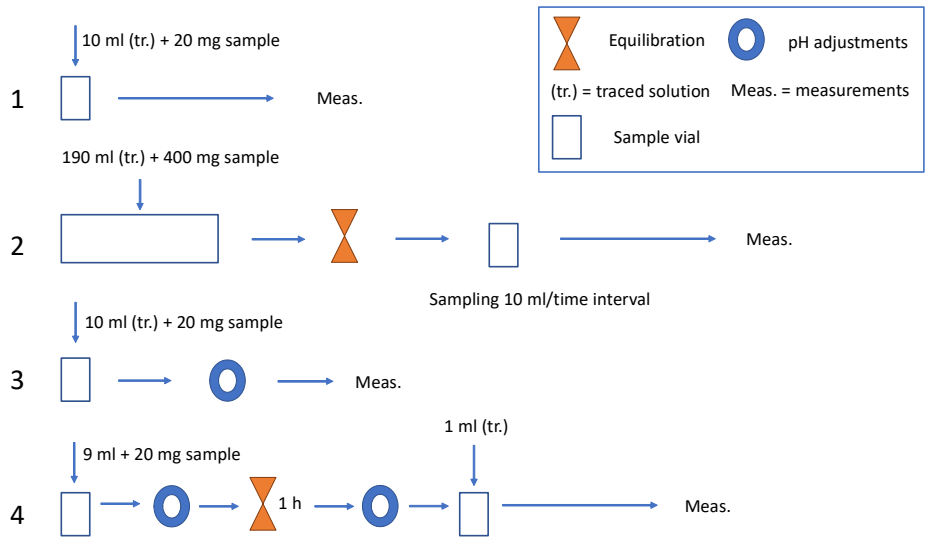

Figure 46: The different methods (M1-M4) used in batch experiments.

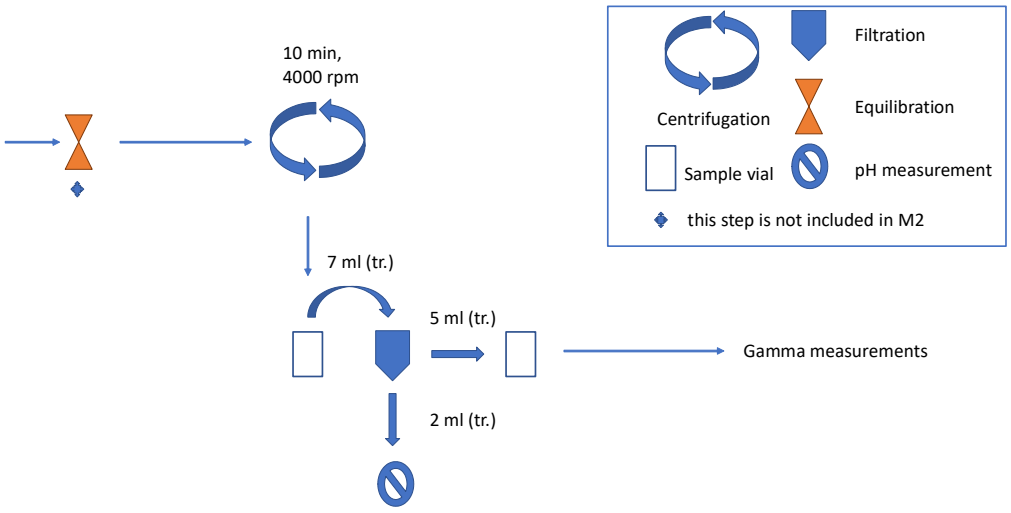

Figure 47: The measurement step equal to every experiment.

4.8.1 Kinetic sorption experiment

The sorption abilities of different microcrystalline celluloses were first pre-tested with a 3-day batch experiment (M1). The different MCC batches from the Aalto University were kept in a freezer (+ 4 °C), from which subsamples were taken at each experiment (Figure 48). Each experiment sample was taken from these subsamples, weighted and kept in a plastic scintillation vial for further steps. Each sample preparation was done on the same day as the experiment started to minimize the decomposition of microcrystalline cellulose. The 3-day experiment was conducted by weighting three parallel samples of 40 mg, an 80 mg sample and a 200 mg sample of each wet MCC material.

One liter solutions of 1/15 M KH_2PO_4 (solution 6) and 1/15 M $Na_2HPO_4*H_2O$ (solution 7) were prepared according to Lurie (1975, p. 253) by diluting 9,1 g KH_2PO_4 (s) and 9,5 g Na_2HPO_4 (s) to 1 liter MilliQ water. A phosphate buffer solution (200 ml) of pH 7 was made by adding 77,6 ml of solution 6 to 122,4 ml of solution 7 (Lurie, 1975, p. 258, F-table). The buffer was traced with 52 µl of ^{57}Co (batch: 692-1 C-2, 3,7 MBq/ml, 0,16 mM HCl, 37 MBq 18.2.2013). 10 ml of the traced buffer solution (37,3 Bq/ml) was directly added to scintillation vial, after which the solutions and MCC samples were equilibrated in rubber sample tracks by 3 days in a rolling Tumble Master Stone Polisher (M.L. Beach products LTD) (Figure 49).

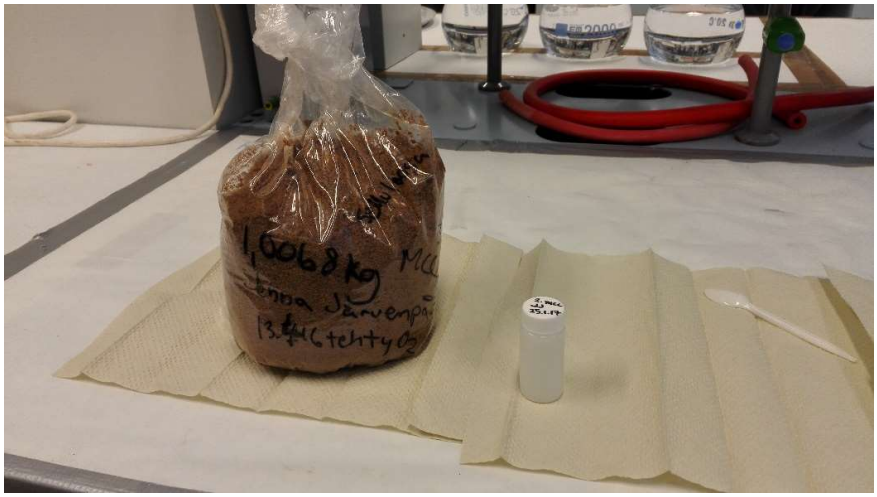

Figure 48: The sampling process from MCC batches.

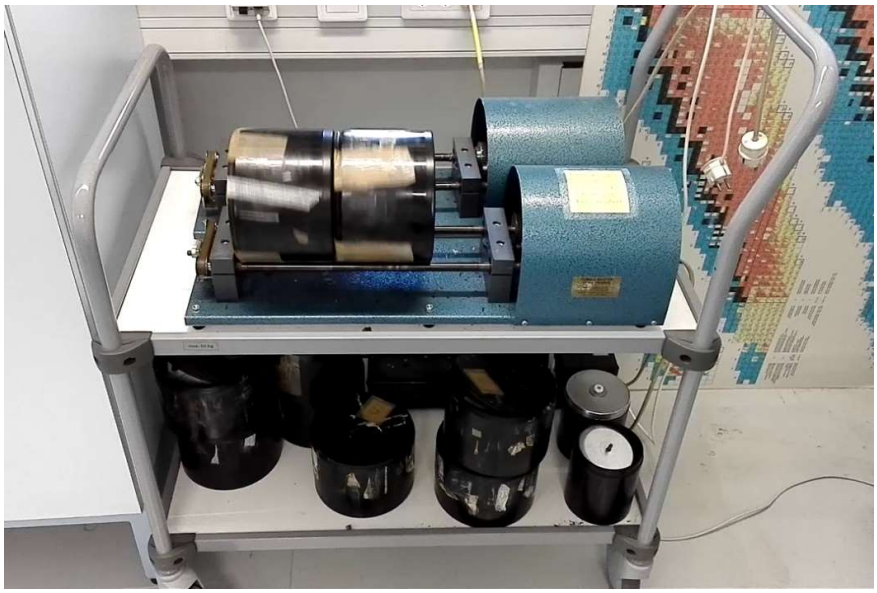

Figure 49: Tumble Master Stone Polisher and rubber sample tracks.

After three days, the solution mixtures were centrifuged with Heraeus Megafuge 1.0R centrifuge (Thermo Scientific, Germany, 50/60 Hz, 2009) for 10 min at 4000 rpm. Then 7 ml of the solution mix was filtered with 0,2 µm filters (Bulk Acrodisc LC Syringe Filters, PVDF membrane, 13 mm, PALL Life Science) and the pH was determined for each separate filtrate (2 ml) and for the traced buffer solution with pH-meter (ORION 4 STAR, Thermo Electron Corporation) (Figure 47). The pH-meter was calibrated every day before measurements. The

exact pH-value of the traced phosphate buffer was measured to be 6,81. Final samples were prepared by pipetting 5 ml of each filtrate to new vials, 5 ml of the traced buffer to each of the two parallel standard vials and 5 ml of MilliQ water to each of the three parallel background vials. The activity of a standard sample was estimated to 10 000 cpm/ 5 ml. The real activities of the vials were measured with gamma spectrometry (Wallac 1480 WIZARD 3" gamma counter, Figure 50) with measurement time of 1800 s and the results were compared to each other. The measurement time for further experiments was 1200 s, if not otherwise mentioned.

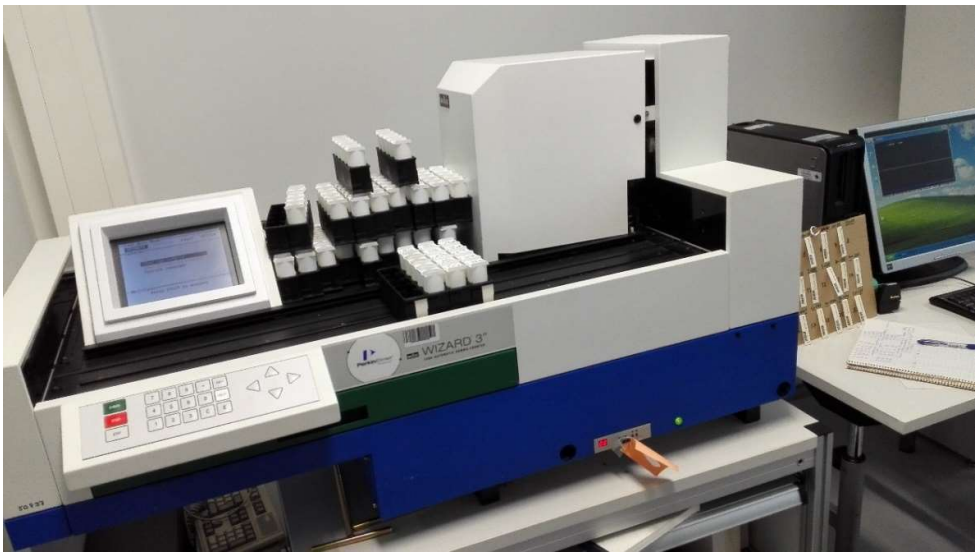

Figure 50: WIZARD 3" gamma counter.

The dry content of each microcrystalline cellulose was determined gravimetrically by first taring three watch glasses in an oven (POL-EKO aparatura, 105℃, max. 115 ℃) for five times and then adding 5-7 g of one MCC per each watch glass, after which the watch glasses were tared three times in the same oven for various time periods. After each drying time in the oven, the samples and the watch glasses were cooled in a desiccator and weighted (Figure 51). The change of each MCC mass and their dry content (%) were calculated from the average values of the last three measurements of the empty and full watch glasses. The determined dry content value of each MCC was used in every further batch experiment to weight the same dry content masses of each MCC samples.

Kinetic sorption experiments were conducted in two separate tests, in a 14-day and a 24-h batch experiments. The 14-day experiment consisted of individual batch experiments of 1 d, 2 d, 3 d, 7 d and 14 d equilibration times, each of which had two parallel samples of each MCC (20 mg dry mass/sample), three background samples (MilliQ) and two standard samples (traced buffer) (M1). For each individual experiment, the samples were taken from the freezer as before. For the 14-day experiment the phosphate buffer solution (350 ml) was prepared according to Lurie (1975, p. 253, p. 258, F-table) and traced with 107 µl of ^{57}Co (batch: 692-1 C-2, 3,7 MBq/ml, 0,16 mM HCl, 37 MBq 18.2.2013). 10 ml of traced buffer solution (37,3 Bq/ml) was added directly to each sample vial, which were then equilibrated for specific time of 1, 2, 3, 7 or 14 days. The samples were centrifuged, filtered and prepared for the gamma spectroscopy as before with calibrated pipettes. The pH-values were determined as mentioned, except with 3 d samples, where pH-meter was Orion, Semi-Micro Combination pH (9103BNWP). The radioactivity of each sample was measured as before. Moreover, the density of the buffer solution was determined, and the volume of each sample was weighted with a scale (Sartorius Weighing Technology GmbH). The BF-values of the samples were close to 500.

Figure 51: MCC samples drying in a desiccator.

By contrast, the 24-h batch experiment consisted of seven subtests of time intervals of 5 min, 15 min, 30 min, 1 h, 2 h, 4 h and 24 h (M2). For the whole 24-h batch experiment, a specific laboratory set-up was made, and all the plastic scintillation vials, filters and syringes were prepared beforehand (Figure 52). The phosphate buffer solution (600 ml) was prepared as before and traced with 186 µl of ^{57}Co (batch: 692-1 C-2, 3,7 MBq/ml, 0,16 mM HCl, 37 MBq 18.2.2013). Three beakers were weighted empty and then full after adding one MCC (400 mg dry mass) per each beaker. The empty beakers were placed on magnetic stirrers for starting the tests. Each experiment started with adding the buffer solution on the beaker. After adding 190 ml of traced buffer solution per each beaker, they were weighted again, and the density of the buffer was determined.

Their almost similar BF-values were close to 480. The tests were started at different times according to the time schedule (Figure 53) made with MATLAB. From each beaker, the two parallel samples were taken during each time interval by closing the magnetic stirrer, pipetting 10 ml of mixed solution to scintillation vial for centrifugation (10 min, 4000 rpm) and filtering 7 ml of the solution, of which 2 ml was used for pH-measurements and 5 ml to gamma measurements. After each pipetting, the magnetic stirrer was turned on to support equilibration. After sampling of 5 min to 4 h tests, the beakers were covered with Parafilm for overnight stirring. The final samples were measured as before and with three background and two standard samples (Figure 54).

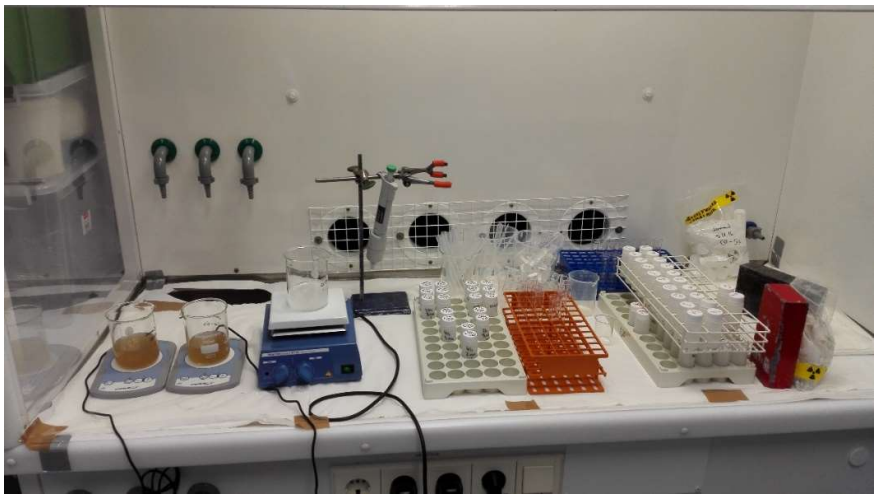

Figure 52: The set-up for the 24-h batch experiment.

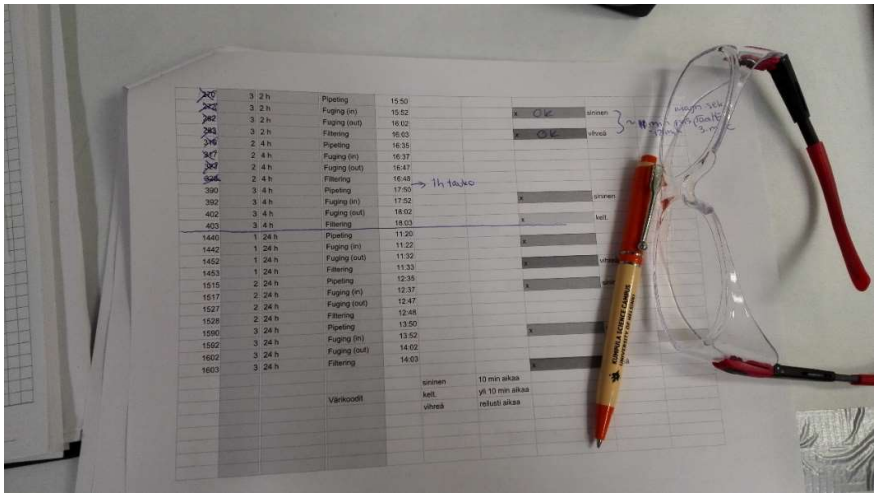

Figure 53: The time schedule for the 24-h batch experiment.

Figure 54: The samples prepared for gamma measurements.

4.8.2 Sorption as a function of pH

After the kinetic sorption experiments, the focus was moved to test the sorption as a function of pH for MCC2 with radionuclides of ^{134}Cs, ^{85}Sr and ^{57}Co. The reason to choose only MCC2 for the further experiments was its good sorption properties compared to MCC1. MCC2 was also made from the oxygen delignified pulp, which is produced between digestion and bleaching leaving some lignin to the pulp in the kraft process. Due to reason to test the effect of lignin on microcrystalline cellulose before bleaching, MCC3 was left out of the further

experiments. Moreover, MCC2 was expected to have the middle content of lignin compared to the other MCCs. The sample masses are given as the dry mass of MCC2. The further experiments were also decided to be conducted with traced solutions of 1/10 of the activity of the kinetic experiments to reduce radioactive waste and dose during the tests.

The sorption as a function of pH was first conducted with ^{134}Cs by M3. 10 mM $NaNO_3$ (aq) was prepared by diluting 0,17 g $NaNO_3$(s) to 200 ml of MilliQ water and tracing it with 233 µl ^{134}Cs (batch: D-2, 37 kBq/ml, 0,2 mM HCl, 5.10.2009). The solutions of 1 M, 0,1 M and 0,001 M of NaOH (aq) and HNO_3 (aq) were prepared for adjustment of pH. One sample of each pH value (1-9) was prepared (20 mg) and weighted as before. 10 ml of the traced solution (3,7 Bq/ml) was added to each sample, after which their pH was measured and adjusted to values of 1 to 9 with the pH-meter (ORION 4 STAR, Thermo Electron Corporation). Then the samples were equilibrated for an hour, after which their pH was again adjusted to the same values as before. Then the samples were equilibrated for approximately 17 hours, centrifuged, filtered and measured with gamma spectrometry. The pH was measured after filtration. The BF-values of samples varied from 500 to 610, which had a significant effect on the reliability of certain results. Moreover, the activities of the samples were 1/3 of planned, since a wrong efficiency value was used in the calculations.

The sorption as a function of pH for ^{134}Cs was repeated with pH-values of 2, 5 and 8 with two parallel samples of MCC2 (20 mg each) per each pH interval by method 4 from Figure 47. By contrast, this time 9 ml of 10 mM $NaNO_3$ (aq) was added first to the samples, after which the pH was measured and adjusted. The samples were equilibrated for an hour and adjusted again to stabilize the equilibrium with the solution without added radionuclide. 20 ml of traced 10 mM $NaNO_3$ (aq) (111,17 Bq/ml) was prepared by adding 688 µl ^{134}Cs (batch: D-2, 37 kBq/ml, 0,2 mM HCl, 5.10.2009) to previously traced 10 mM $NaNO_3$ (aq) (^{134}Cs: 3,6 Bq/ml, 20 ml). 1 ml of this new traced solution was added to each sample, after which the samples were equilibrated for 20 hours. Finally, the samples were treated and measured as mentioned earlier, except the standards were made by adding 4,5 ml 10 mM $NaNO_3$ (aq) and 0,5 ml 10 mM $NaNO_3$ (aq) (111,17 Bq/ml) to scintillation vials for the gamma measurements. The density of the new traced solution was determined gravimetrically as before. Due to more suitable acid and base solutions, the BF-values were kept between 500-510.

The sorption as a function of pH was then conducted with ^{85}Sr by method 4 from Figure 47. An intermediate dilution (63 kBq/ml) was prepared by adding 307 µl ^{85}Sr (batch: 818, 74

MBq, 7,4 MBq/ml, 1 mM HNO_3, 1.11.2016) to 10 ml 1 mM HNO_3 (aq). 15 ml 10 mM $NaNO_3$ (aq) was then traced with 100 µl ^{85}Sr of intermediate dilution to achieve the activity concentration of 420 Bq/ml. One sample (20 mg) of each pH value (1-9) was prepared and weighted. 9 ml 10 mM $NaNO_3$ (aq) was added to each sample, after which the pH was measured and adjusted. After one hour equilibration, the pH was measured and adjusted again. 1 ml of traced 10 mM $NaNO_3$ (aq) (420 Bq/ml) was added to each sample, after which they were equilibrated for approx. 20 hours, centrifuged, filtered and measured. The standard samples were prepared by adding 4,5 ml 10 mM $NaNO_3$ (aq) and 0,5 ml 10 mM $NaNO_3$ (aq) (420 Bq/ml) to scintillation vials. The density of the solution was determined. The BF-values were kept between 500-510.

The sorption as a function of pH for ^{57}Co was conducted with the same method by tracing 15 ml 10 mM $NaNO_3$ (aq) with 7 µl of ^{57}Co (batch: 692-1 C-2, 3,7 MBq/ml, 0,16 mM HCl, 37 MBq 18.2.2013) and then adding 9 ml 10 mM $NaNO_3$ (aq) to each sample (20 mg), one for each pH interval (1-9). The pH adjustments and equilibration were done as before. After the second pH adjustment, 1 ml of traced $NaNO_3$ (aq) (38,9 Bq/ml) was added to each sample and they were equilibrated for approx. 18 hours. The sample preparation for gamma measurements was executed as before. Due to the unexpected results, the test was repeated with some improvements. The re-test was conducted with two parallel samples (20 mg each) of pH 7, on which 10 ml of 10 mM $NaNO_3$ (aq) (3,85 Bq/ml) was added directly. Exceptionally M3 from Figure 47 was used in the re-test to compare the methods. The traced solution was made by diluting a previously done tracer solution with MilliQ water. After combining the MCC and the solution, the pH adjustments and equilibration were done as before. After the second pH adjustment, the samples were equilibrated for approx. 19 hours, centrifuged, filtered and measured. New background and standard samples were done. Due to convergent results, the sorption of ^{57}Co in phosphate buffer was measured again.

The re-test on the sorption of ^{57}Co in phosphate buffer was conducted by tracing previously made phosphate buffer solution (100 ml) of pH 7 with 5 µl of ^{57}Co (batch: 692-1 C-2, 3,7 MBq/ml, 0,16 mM HCl, 37 MBq 18.2.2013). 10 ml of traced buffer solution (4 Bq/ml) was added to four parallel samples of MCC2 (20 mg), which were then equilibrated for 1 day, centrifuged, filtered and measured (M1). New standard samples were prepared from the traced buffer solution. The density of the buffer was also determined. The results were convergent with the 14-day experiment results for 1 day equilibration with MCC2.

Due to the contradictory results between ^{57}Co sorption on MCC2 in $NaNO_3$ (aq) and phosphate buffer, one more experiment with ^{57}Co was executed. The last experiment was focused on the sorption as a function of pH on phosphate buffers of pH 3 and 7 with concentration of 0,01 M, 0,1 M and 1 M. The 1 M buffers were made according to Beynon (2008) by diluting 13,8 g $Na_2HPO_4*H_2O$ (s) to 100 ml of MilliQ water and adjusting the pH to 7 with 1-10 M NaOH (aq) and by diluting 9,8 g H_3PO_4 (s) to 100 ml of MilliQ water and adjusting the pH to 3 with 10 M NaOH (aq). The other solutions of 50 ml (0,1 M and 0,01 M) were diluted from these two buffers. The pH values were measured directly from the solutions. The six buffer solutions were each traced with 3 µl of ^{57}Co (batch: 692-1 C-2, 3,7 MBq/ml, 0,16 mM HCl, 37 MBq 18.2.2013).

Three parallel samples of MCC2 (20 mg) and two standard samples were prepared for each buffer solution (4,5 Bq/ml). 10 ml of the buffer solution was added directly to the samples, after which they were equilibrated for 24 hours (M1). Three new background samples were made. The density was determined for each buffer solution. After equilibration, the samples were treated as before. Exceptional results on samples with pH 7 (0,01 M) were achieved.

4.8.3 The effect of the Donnan potential

Before the last sorption experiment on phosphate buffers and ^{57}Co, the effect of ionic strength of the solution on sorption was measured with two tests with M1. The tests were conducted by preparing 50 ml of 0,01 M, 0,1 M and 1 M $NaNO_3$ (aq) solutions from previously made 1 M $NaNO_3$ (aq) and 50 ml of 0,01 M, 0,1 M and 1 M $NaClO_4$ (aq) solutions by diluting 14,0 g $NaClO_4$ (s) to 100 ml MilliQ water to prepare 1 M $NaClO_4$ (aq). All six solutions of 0,01 M, 0,1 M and 1 M were traced by adding 3 µl of ^{57}Co to each solution (batch: 692-1 C-2, 3,7 MBq/ml, 0,16 mM HCl, 37 MBq 18.2.2013). Three parallel samples were prepared for each solution from MCC2 (20 mg) and 10 ml of the solution (4,7 Bq/ml) was directly added to them. The samples were then equilibrated for 24 h, after which they were processed as before. The density was also determined for each traced solution. The results were compared to each other and to the previous sorption experiments with ^{57}Co. The sorption of ^{57}Co increased with the concentration of $NaNO_3$(aq), which could indicate the effect of the Donnan potential. Moreover, it was shown that the experiment methods had noticeable effects on the K_d -values between different experiments.

5 Results and discussion

The experimental work on AaltoCell^{TM} materials was divided into the structural studies and the batch sorption experiments. These included SEM imaging, measurements on BET surface area, particle size distributions and molecular weight distribution as well as determination of carbohydrate and lignin content and surface lignin coverage. Moreover, several different batch sorption experiments were executed to reveal phenomena behind the sorption of radionuclides, ^{57}Co, ^{134}Cs and ^{85}Sr, in various solutions and different MCC samples. In the following subsections the results of the experimental work are presented, after which the reliability and repeatability, the research questions and the limitations are discussed in detail.

5.1 SEM images

The morphology of three different microcrystalline celluloses were determined by SEM imaging of five different magnifications (70x, 250x, 1000x, 3000x and 10 000x). All SEM images can be seen on Appendix 4 to Appendix 8. From these images, some discoveries between AaltoCell^{TM} materials were found. First, white MCC1 made from bleached sulfate pulp had clearly more homogenous structure than other more brown MCC materials, which can be seen on Figure 55, taken from Appendix 4. Although MCC1 had some longer fibers of approx. 1000 µm, it mainly consisted of small homogenous clusters approx. 70 µm to 150 µm. By contrast, MCC3 lacked surprisingly those long fibers, since its longest was approx. 600 µm. The minimum sizes of clusters in MCC3 were 200–300 µm. The distribution of small clusters was higher in MCC1 than in MCC3 as shown in Figure 55.

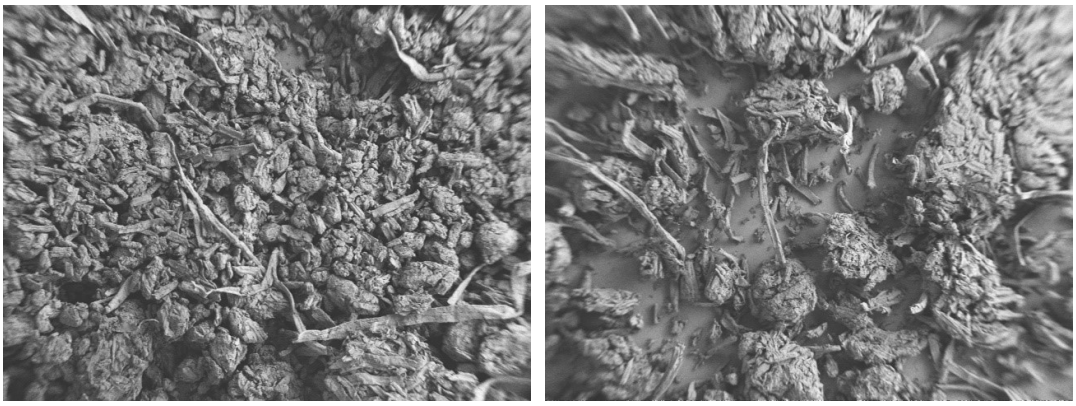

Figure 55: The structure of MCC1 (left) and MCC3 (right) with 70x magnification.

Secondly, MCC3 made from unbleached pulp after sulfate cooking showed more roughness and spikiness on 10 000x magnification than MCC1 (Figure 56 taken from Appendix 8). This might be due to the different manufacturing processes and origins of microcrystalline celluloses. Finally, MCC2 made from unbleached oxygen delignified pulp was found to have closely similar micro-level structure to other MCC materials as seen on Figure 57 taken from Appendix 5. The fibers of MCC2 were less visible than of MCC1 and thus only lengths of approx. 40 and 80 µm were determined. By contrast, MCC1 had fibres of lengths of approx. 70–140 µm. No cluster size comparison was made on this magnification due to the different image locations on the samples.

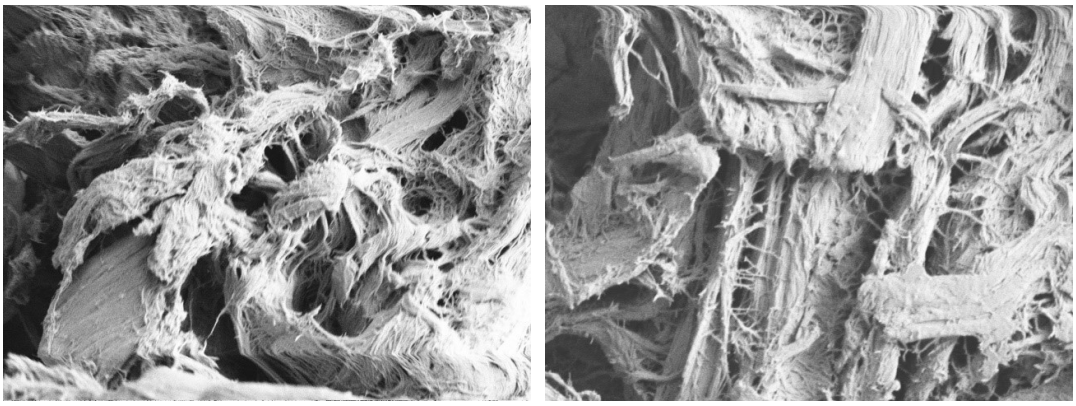

Figure 56: The structure of MCC1 (left) and MCC3 (right) with 10 000x magnification.

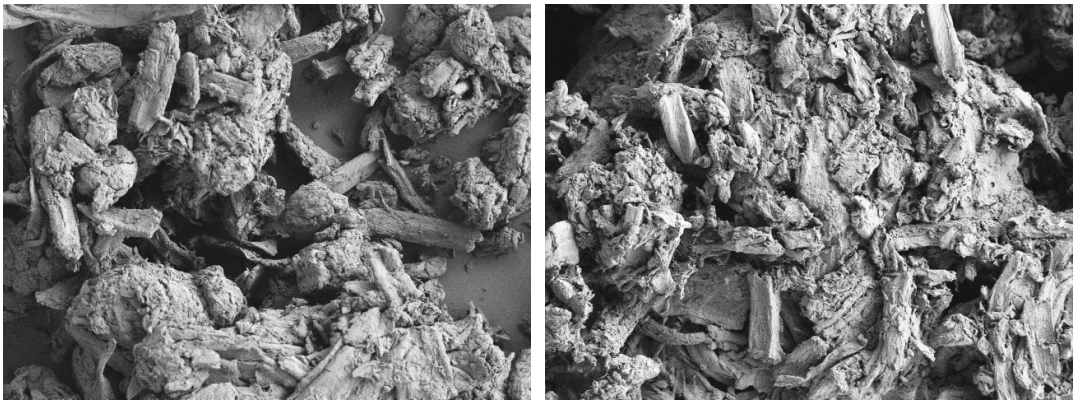

Figure 57: The structure of MCC1 (left) and MCC2 (right) with 250x magnification.

5.2 Specific surface areas of microcrystalline celluloses

The specific surface areas of microcrystalline celluloses were determined volumetrically with the BET-instrument. Each microcrystalline cellulose was measured with three parallel samples and both the averaged results and their standard deviations are shown in Table 3. The results on Table 3 show increasing values of BET surface area and adsorption volume of pores from MCC1 to MCC3, which could be explained by the different manufacturing processes. By contrast, the results of MCC2 show unexpectedly high values compared to other MCC materials. Even the adsorption average pore widths of MCC2 are higher than in any other MCC material. On the other hand, the BET surface area value of MCC2 is still closer to the value of MCC3 than MCC1, which is reasonable and expected. The BET surface area results are close to some literature values, e. g., the values of cellulose and pine wood biochar (21,9 m^2/g and 33,3 m^2/g) in Li, Li, Wu and Zheng (2014).

Table 3: The BET results for microcrystalline cellulose samples

Parameter	MCC1	MCC2	MCC3
BET surface area (m^2/g)	29,5 ± 1,8	41,5 ± 2,9	38,8 ± 0,8
BJH Adsorption volume of pores, 17 000 -3000 Å (cm^3/g)	0,089 ± 0,005	0,154 ± 0,005	0,107± 0,000
D-H Adsorption volume of pores, 7500 -3000 Å (cm^3/g)	0,088 ± 0,005	0,149 ± 0,002	0,106 ± 0,000
BJH Adsorption average pore width (Å)	113,4 ± 2,1	142,1 ± 5,2	105,9 ± 1,8
D-H Adsorption average pore width (Å)	114,1 ± 2,1	140,3 ± 8,4	106,6 ± 1,8

5.3 Particle size distributions

The particle size distributions of microcrystalline celluloses were measured individually with a particle size analyzer. The obtained results can be found in Table 4, where d(x) notations percentiles of x below which x % of the particles are located. For example, d(0.1) describes the 10^{th} percentile of the cumulative particle size distribution as mentioned in Koo and Heng (2001). The combination of the particle size distributions is shown in Figure 58, in which the different MCCs are marked with red (MCC1), green (MCC2) and blue (MCC3). The wide size range of different clusters and particles on the SEM images of MCC1 can be verified with the results of both Table 4 and Figure 58, since the 90 % percentile is significantly higher than with other MCC materials. The values of other percentiles are very close to each other, e. g., d(0.1) values for MCC2 (17,9 µm) and MCC3 (16,5 µm) as well as d(0.5) for MCC1 (73,1 µm) and MCC2 (76,9 µm), which indicates similar small structures as seen on SEM images.

It can be seen on Figure 58 that the volume peak of particle size differs a lot between different MCC materials, e. g., the peak of MCC1 is highest around 70–80 µm (~ 8,2 %), whereas the peaks of MCC2 and MCC3 are smaller (80–100 µm, 7 % and 70–80 µm, 6,8 %). Moreover, the second volume peak can be found on MCC1 (600 µm, 2 %) and MCC3 (500 µm, 1,7 %), which describes the heterogeneity of clusters and other fiber-like particles in SEM images. No clear second volume peak was found on MCC2, although the decrease of volume was uneven close the particle size areas of the second volume peaks of MCC1 and MCC3.

Table 4: The particle size distribution results

Parameter	MCC1	MCC2	MCC3
d(0.1) (µm)	21,9	17,9	16,5
d(0.5) (µm)	73,1	76,9	64,2
d(0.9) (µm)	553,9	254,6	199,3

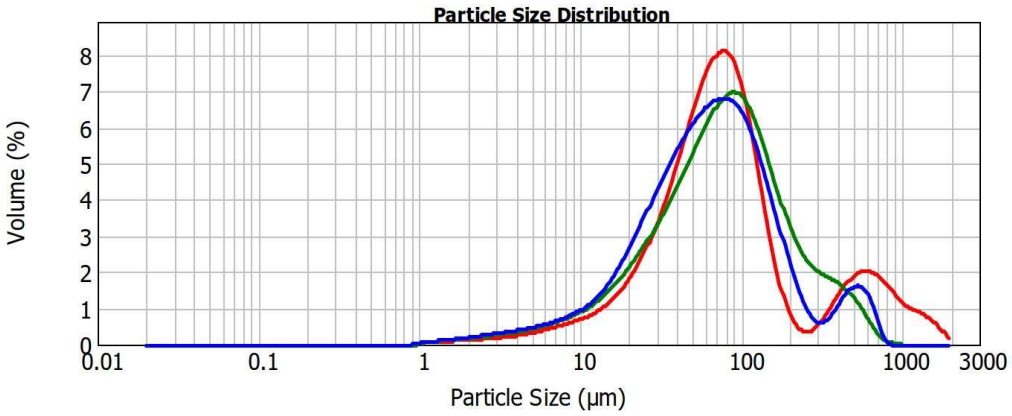

Figure 58: The particle size distributions of all microcrystalline cellulose materials.

5.4 Molecular weight distributions

The molecular weight distributions of microcrystalline celluloses were determined with the GPC system by measuring each microcrystalline sample twice and comparing the results with each other. Since the differences between runs on each microcrystalline cellulose were generally small, the use of average values in the result interpretation was acceptable and reasonable. The results of the runs are shown in Appendix 9. The distributions are shown in Figure 59 and the averaged parameters in Table 5. The colors in Figure 59 represent MCC1 (red), MCC2 (green) and MCC3 (blue). The unit of different molar mass parameters is kg/mol, whereas the dispersity index and the different degrees of polymerization are unitless. The average and DP values were comparable with the literature values, e.g., Testova et al. (2014).

The similar molecular weight distribution of MCC1 and MCC2 can be seen on these results, as well as their significant difference in peak width and height compared to MCC3. The narrowest distribution and the highest peak belonged to MCC3, whereas 1. and MCC2 had almost similar values in each measured parameter. Even the different degrees of polymerization (DP) values support their likeness. According to the DP values, the most dominating share of cellulose chains in each microcrystalline cellulose lies in the lengths above DP2000, which has not been measured in this experiment. This could explain the clusters and large particles in the SEM images. Moreover, the dispersity index ($Đ_M$) reveals that 1. and MCC2 have higher non-uniformity and broader distribution than MCC3. The differences between microcrystalline celluloses could be explained by variations in acid hydrolysis and depolymerization of cellulose, as mentioned in Vanhatalo et al. (2016).

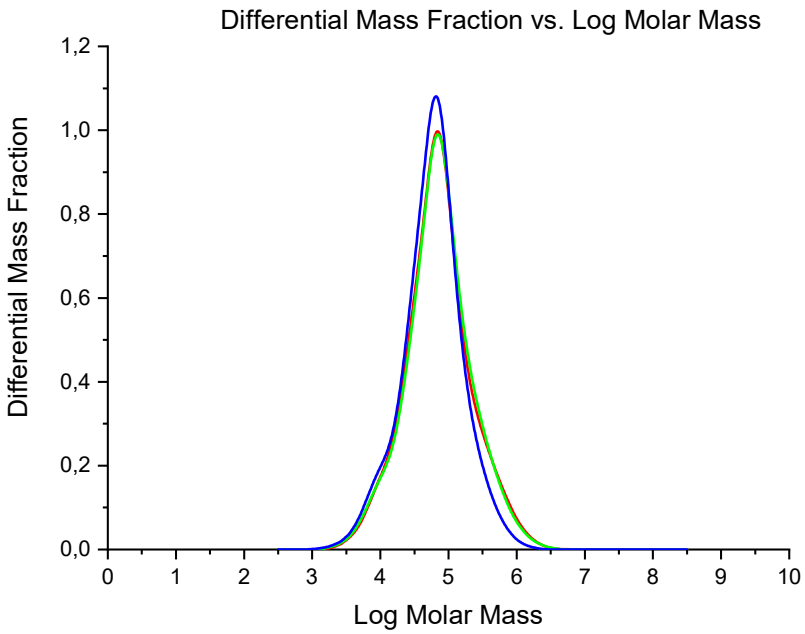

Figure 59: The molecular weight distribution as a function of logarithmic molar mass.

Table 5: The parameters to determine MMD

Parameter	MCC1	MCC2	MCC3
M_n (kg/mol)	37,7	37,4	32,4
M_w (kg/mol)	139,2	138,3	98,2
M_z (kg/mol)	539,3	517,1	286,9
M_{z+1} (kg/mol)	1 350,4	1 306,7	700,8
$Đ_M$	3,7	3,7	3,0
DP50	0,03	0,03	0,04
DP100	0,09	0,09	0,11
DP2000	0,10	0,09	0,05

5.5 Carbohydrate and lignin contents

The carbohydrate (CH) contents of microcrystalline celluloses were determined with HPAEC-PAD by measuring each subsample twice and comparing the results between runs A and B. The results can be seen on Appendix 10 to Appendix 15, where parallel samples for different MCC materials are: samples 1–2 (MCC1), samples 3–4 (MCC2) and samples 5–6 (MCC3). The standard sample was also measured twice, from which the run B results were used to determine different parameters for samples (Appendix 16). The average results of each microcrystalline cellulose are given in Table 6. The CH values of MCC1 and MCC2 are taken from the average values of the A and B runs of samples 2 and 3, since the runs of the first and the fourth sample differed significantly from the others. The tabulated CH values of MCC3 are the average values of all four runs of samples 5 and 6. The percentage values of carbohydrates are calculated according to Appendix 17. The lignin contents of MCC samples were determined according to Appendix 18.

Table 6: The composition of MCC samples

Composition (%)	MCC1	MCC2	MCC3
Sugars:	99,80	90,80	88,89
Glucose	88,32	83,59	82,77
Xylose	6,07	3,18	2,67
Mannose	5,42	4,02	3,45
Lignin:	0,02	4,71	1,45
Klason	-0,10	4,61	1,34
ASL	0,12	0,11	0,11
Sum:	99,82	95,51	90,35

The averaged results are presented on Table 6, where Klason % refers to the percentage of insoluble lignin and ASL % to the acid-soluble lignin in the sample. No extractives were found on the microcrystalline samples. Ash and acetate contents of the samples were not studied, although they could explain the missing percentages of MCC2 and MCC3. According to the results, the percentage of the sugars in MCC decreases as the total lignin percentage increases, with an exception of MCC2. Its sugar content is nearly the same as with MCC3, although its total lignin content is the highest of all MCC samples. On the other hand, different MCC samples had similar acid-soluble lignin contents. The lowest total lignin content belonged to MCC1, which consisted of 99,8 % of sugars. The Klason lignin experiment was repeated for two parallel samples of MCC2 and MCC3. The results were 5,4 % (MCC2) and 1,9 % (MCC3), which were higher, yet still comparable with the results of the first experiment. All obtained results were comparable with the literature values, e.g., birch kraft pulp values before and after hot water extraction as in Borrega and Sixta (2013).

5.6 Surface lignin coverages

The surface lignin and cellulose coverages as well as the elemental contents of the microcrystalline cellulose samples were determined with XPS from two locations from each sample. The obtained spectra of the samples are presented in Appendix 19 to Appendix 21. The XPS spectrum of the reference sample, 100 % cellulose filter paper, is shown in Appendix 22. The wide atomic concentrations in the surface area in atomic % for both the MCC and the reference samples are shown in Appendix 23. Exceptionally, the MCC3 sample was measured from three locations, since one location was visibly charged. The atomic concentrations of different functional group components, e.g., CC, CO, COO, COOO, in C 1 s signal are presented in Appendix 24. From Appendix 23 and Appendix 24, the measurement data points were plotted in the correlation graph (Figure 60).

As can be seen from this graph, the measurement data points form a clear pattern, that closely follows the linearity of the theoretical values. The distribution of these points is narrowly spread without any outliers. Moreover, it shows clear correlation between the amount of C-C carbons in total carbon composition and O/C atomic ratio. As expected, MCC2 has the highest C-C carbon composition of total carbon and the lowest O/C atomic ratio, whereas the values of MCC1 are the opposite. The measurement points of MCC1 are similar to the reference sample.

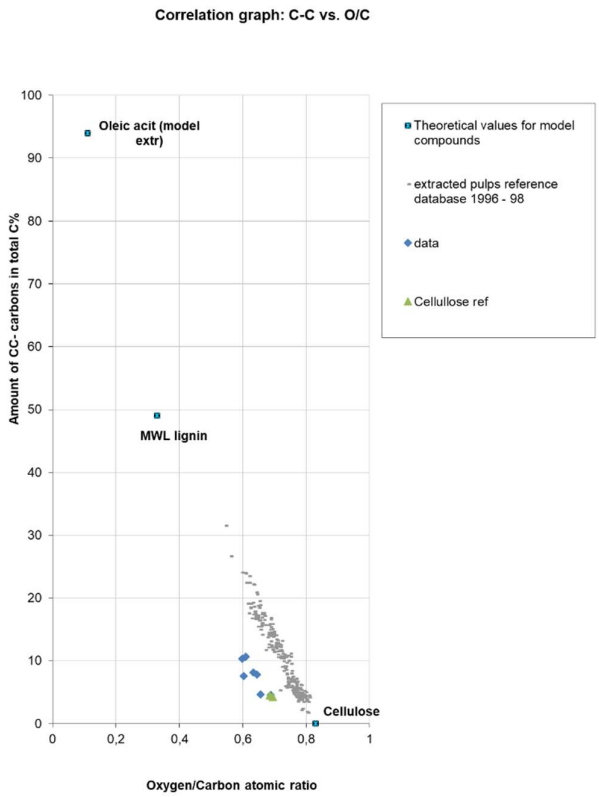

Figure 60: The correlation graph of C-C carbons vs. O/C ratio.

The surface lignin content is determined according to Appendix 25, from which the average values are derived to Table 7. According to these results, the decreasing order of the surface lignin content is: MCC2 > MCC3 > MCC1. These results correspond with the previous results by MCC2 having the highest lignin content (12,55 %) and MCC1 the lowest (0,77 %). They also correspond with the literature values of Johansson, Campbell, Koljonen and Stenius (1999), where an extracted bleached chemical pulp sample had smaller C-C peak in C 1s region than an unbleached sample.

Table 7: The surface lignin contents of MCCs

MCC	MCC1	MCC2	MCC3
Lignin content (%)	0,77	12,55	7,53

5.7 Results of the batch sorption experiments

The batch experiments are numbered from 1 to 11 and separated by their experiment method M1 to M4 in Appendix 2. The different experiment methods are explained in Figure 46. The experiments were started with the 3-day pre-test on ^{57}Co (1), which indicated no significant difference on sorption between different masses of MCCs. By contrast, it showed clearly the increase of sorption as the expected lignin content increased. The sorption order was found to be: MCC3 > MCC2 > MCC1, which was confirmed with later experiments. Since no correlation between the mass and sorption was found, the experiments were further executed with 20 mg of dry MCC per sample. The determination of the uncertainty of the scale, the calculations of the dry mass uncertainties and the results of the 3-day pre-test are shown in Appendix 26 to Appendix 28. Due to the lack of gravimetric data of the pre-test, the results are exceptionally not integrated into any graphs. The experiments following the pre-test had adequate gravimetrical data taken to make the further results comparable.

Since the 14-day and 24-h batch experiments (2, 3) as well as the re-test with ^{57}Co (9) were made in the same phosphate buffer, they were plotted with uncertainties in the same graph (Figure 61). The results of the re-test are circled in the graph to visualize their comparability to the other results on MCC2. The original data of the graph is attached in Appendix 29. According to Figure 61, the sorption of ^{57}Co increases from 5 min to 2 hours, from which it starts to decline. This trend is the most visible with MCC3, which shows the highest K_d-values in the 24-h batch experiments. As expected, MCC3 shows the highest and MCC1 the lowest K_d-values also in the 14-day batch experiment from 24 h to 14 days.

By contrast, the results of 24 h time interval in the 24-h batch experiments are lower than in the 14-day batch experiment. This and other differences between these two experiments could be due to the different experiment methods (M1-M2) and swelling of the MCC matrices. The 24-h batch experiment was done by taking individual samples from the same decanter glass through the whole experiment (M2), whereas the 14-d batch experiment was conducted with individual samples vials and gravimetric measurements (M1). The stirring method and the sampling process used in M2 might have caused some heterogeneity on the sampled MCC masses as well as increase swelling compared to M1. By contrast, the precision of the parallel samples in these experiments remained high regardless of the method used. Moreover, the results of the 14-day and 24-h batch experiments resemble each other by rising and declining trend describing the ion-exchange kinetics of each MCC matrix.

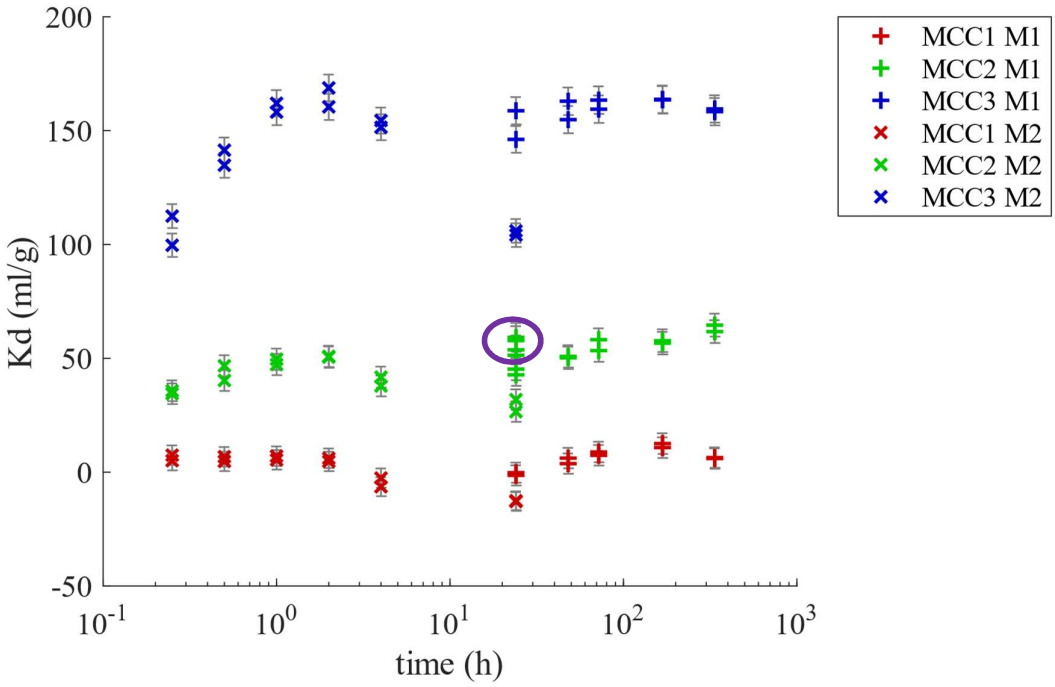

Figure 61: The sorption of ^{57}Co as a function of time for MCC1 to MCC3 with experiment methods M1 and M2 in phosphate buffer. The results of the re-test (experiment 9) are circled in the graph.

According to Helfferich (1962, p. 509, 511) elastic ion-exchange resins will achieve swelling equilibrium in aqueous solvents due to, e. g., the hydration tendency of the functional groups and counter-ions, the osmotic activity of the counter-ions and electrostatic forces. The equilibrium is dependent on several factors, such as, swelling pressure and complex formation. Swelling causes water accumulation on the pores of the ion exchanger, thus increasing the electrolyte sorption, mobility of the counter-ions and ionic dissociation, which further increase the rate of ion exchange to achieve equilibrium (p. 516). This phenomenon could be seen on Figure 61, where M2 method in the 24-h batch experiment produces swelling equilibrium significantly earlier than M1 method in the 14-d batch experiment. The equilibrium times (~ 24 h) for further experiments were chosen according to the results on this graph.

To compare the sorption results as a function of pH between different radionuclides within the same sodium nitrate solution, the data of the sorption vs. pH experiments on ^{134}Cs (4, 5), ^{85}Sr (6) and ^{57}Co (7, 8) were plotted with uncertainties in the same graph shown in Figure 62. The results of the re-test on ^{57}Co (8) are also circled in the graph to compare them with other results. The original data of the graph is attached in Appendix 30.

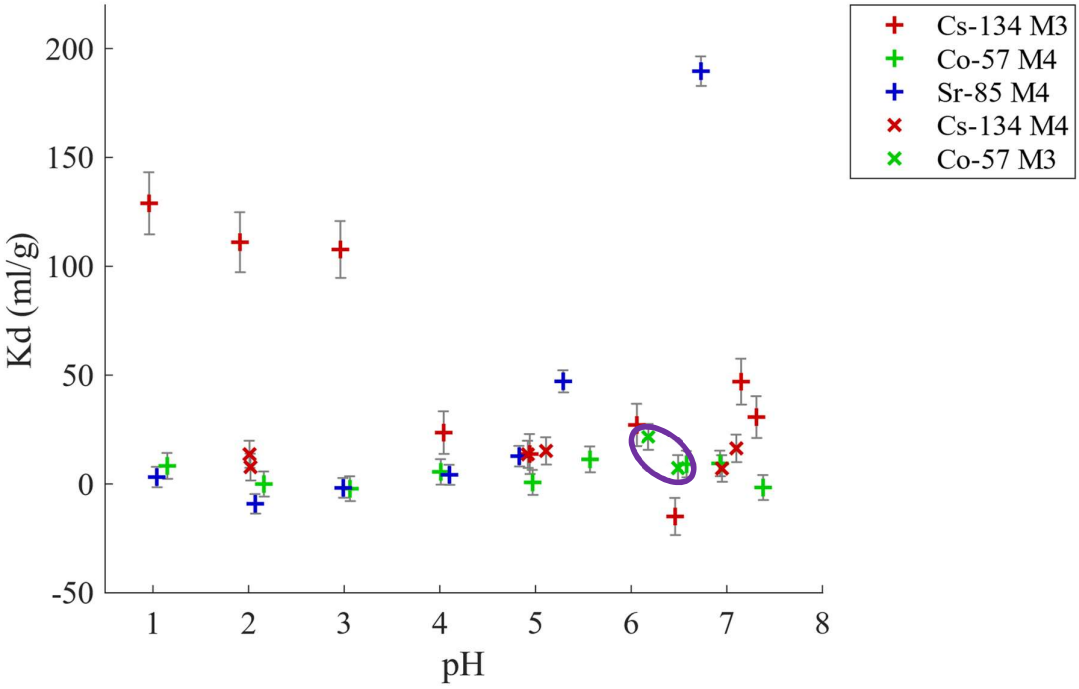

Figure 62. The sorption of ^{134}Cs, ^{57}Co and ^{85}Sr as a function of pH for MCC2 with experiment methods M3 and M4 in 10 mM $NaNO_3$ (aq). The results of the re-test on ^{57}Co (experiment 8) are circled in the graph.

According to Figure 62, the sorption of ^{57}Co is negligible compared to the results of other radionuclides on MCC2. Moreover, it shows no significant sorption on ^{57}Co regardless of the method used, contrary to the graph shown in Figure 61. Accordingly to Helfferich (1962, p. 139) this difference between sorption behaviors of cobalt could be due to complex formation of cobalt with co-ions, such as phosphate ions, $H_2PO_4^-$ and HPO_4^{2-}. Anionic metal complexes could enter the anion exchanger due to the reduced efficiency of Donnan exclusion of cobalt.

Although cobalt forms various complexes with phosphates as mentioned in Marzouki, Sayed, Graia and Zid (2019), no anionic cobalt phosphate complexes were found from literature. Thus, this difference could be resulted from, e.g., possible precipitation of cobalt complexes during batch experiments, unexpected interactions between phosphates, MCC2 and cobalt, formation of phosphate groups in the microcrystalline cellulose or impure washing of residual H_2SO_4 (aq) after hydrolysis. Nevertheless, the difference between cobalt sorption in phosphate buffer and sodium nitrate in Figure 61 and Figure 62 is significant and presents a new phenomenon, which is not fully studied in this research.

On the other hand, the sorption of ^{85}Sr shows a clear rising trend as a function of pH. This explicit ion exchange behaviour of MCC2 resembles a cation ion exchanger, since the sorption capacity increases as the pH increases. This could be due to the ionized carboxylic acid groups and deprotonated alcohol groups, which can attract positively charged electrolytes from the solution. By contrast, the sorption of ^{134}Cs shows two different trends separated by the experiment method. M3 method produced a declining trend, whereas M4 method showed no significant sorption. This difference could be due to the variations of the BF-values, which are between 505– 610 (M3) and 500–506 (M4) (Appendix 30).

Other explanation could be different procedures of these two methods, since in M4 the ion exchanger is let to stabilize with the sodium nitrate solution before adding the tracer, whereas in M3 the tracer is mixed with the solution and added at the same time into MCC2 before adjusting the pH. The stabilizing period between MCC2 and the sodium nitrate solution might saturate the sorption sites with Na^+ and decrease the sorption of certain radionuclides. This could also explain the similar behavior of ^{57}Co between Figure 62 and Figure 63 in 10 mM $NaNO_3$ (aq) between pH 4–5. The K_d -values for ^{57}Co achieved by M1 in Figure 63 are clearly higher than in Figure 62. Only one of the circled results (M3) in Figure 62 achieves a K_d -value (21,5 ml/g) comparable to the values in Figure 63 (21,7–33,4 ml/g) (Appendix 30 and Appendix 31).

To compare the sorption results as a function of ionic strength between $NaNO_3$ (aq) and $NaClO_4$ (aq), the data of the sorption vs. ionic strength experiment on ^{57}Co (10, M1) was plotted with uncertainties in the graph shown in Figure 63. The original data of the graph is attached in Appendix 31. According to Solomon (2001), the ionic strength for $NaNO_3$ (aq) and $NaClO_4$ (aq) is the same as their molarity, since both compounds contain only single-charged ions. Thus, the results of these two solutions can be directly compared to each other by different molarity. No pH adjustment was done during this experiment. As can be seen from the graph, the sorption of ^{57}Co is the highest in 0,01 M $NaClO_4$ (aq) (52,6–56,1 ml/g) at pH ~ 4,7 and the lowest in 0,1 M $NaClO_4$ (aq) (−3,6–2,1 ml/g) at pH ~ 4,6.

By contrast, for $NaNO_3$ (aq) the highest values are 47,2–53,7 ml/g for 1 M at pH ~ 6,5 and the lowest 0,9–6,7 ml/g for 0,1 M at pH ~ 4,8–4,9. For both solutions, the lowest K_d-values are close to zero, whereas the highest K_d-values reach close to 60 ml/g. The sorption of ^{57}Co on $NaNO_3$ (aq) shows an increasing trend as a function of ionic strength and pH, which is opposite to the decreasing trend on $NaClO_4$ (aq).

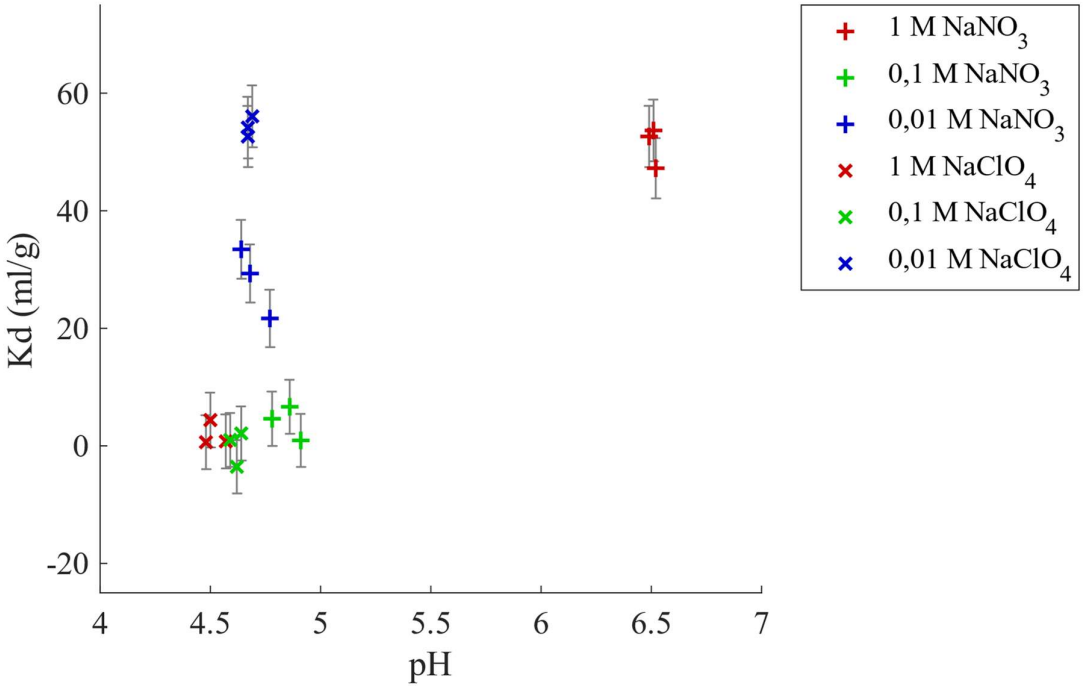

Figure 63: The sorption of ^{57}Co as a function of pH for MCC2 with experiment method M1 in 0,01–1 M $NaNO_3$ (aq) and 0,01–1 M $NaClO_4$ (aq).

The sorption behaviour on these solutions could be explained by the increase of electrolyte exclusion by the Donnan potential with the decrease of solution concentration. As the electrolyte exclusion increases, the sorption of ^{57}Co decreases, in agreement with Helfferich (1962, p. 136). Since ClO_4^- ion is inert, it doesn´t have an effect on the Donnan potential and decrease the sorption with molarity.

The data of the sorption vs. pH in phosphate buffer experiment on ^{57}Co (11, M1) was plotted with uncertainties in the graph shown in Figure 64. The plot for K_d is exceptionally logarithmic, which visually creates large errors on small values. However, the uncertainties of these small values are similar to the other uncertainty values on this and other graphs. The original data of the graph is attached in Appendix 32. According to Figure 64, the sorption of ^{57}Co increases clearly as the pH increases and the molarity decreases. This can be seen on both pH areas (~3 and ~7). As it appears, the electrolyte exclusion by the Donnan potential doesn´t have an effect on the sorption of ^{57}Co in phosphate buffer solution in these pH areas.

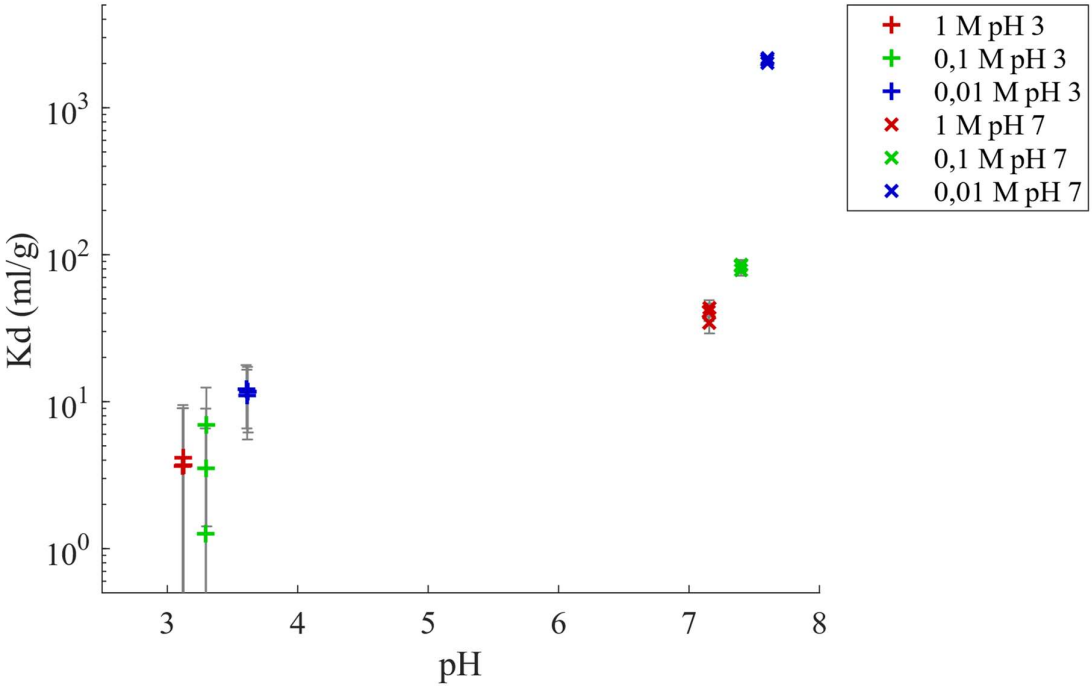

Figure 64: The sorption of ^{57}Co as a function of pH for MCC2 with experiment method M1 in 0,01–1 M phosphate buffer solutions of pH 3 and 7.

The highest K_d-values 2017,6–2171,0 ml/g are present in 0,01 M phosphate buffer solution with pH 7,6 and the lowest K_d-values 1,3–6,9 ml/g in 0,1 M and 3,7–4,21 ml/g in 1 M phosphate buffer solutions with pH 3,3 and 3,1. Moreover, the K_d-values for 0,01 M and 0,1 M phosphate buffer solutions were clearly higher than the values presented in Figure 61 with 0,067 M phosphate buffer. For example, the K_d-values for MCC2 in a 14-day batch experiment with 1 d equilibrium time are 42,7–45,2 ml/g at pH 6,9 and in a 24-hour batch experiment with 24 h equilibrium time 26,6–31,8 ml/g at pH 7,0.

These differences could be due to the different electrolyte compositions of the phosphate buffer solutions, since both K^+ and Na^+ ions were present in the buffer solution used in the experiments 1, 2, 3 and 9, but only Na^+ ions in the experiment 11. In addition, the differences could be also explained by the different pH values of the results, the different experiment methods used and by the different molarity of the buffer solutions. Moreover, the time passed between the experiments might have caused degradation of MCC2, although it was kept consistently in the refrigerator.

5.8 Reliability and Repeatability

The experimental work was divided into structural studies and batch sorption experiments. The results of the structural studies presented in Sections 5.1–5.6 were achieved through different measurements with various parallel samples, images or locations. In SEM imaging one to two images were taken per each magnification except with 10 000 times magnification of MCC2 due to the burning of its surface. The number of parallel samples for other measurements were: 3 for specific surface area measurements, 2 for particle size distributions, 2 for molecular weight distributions and 2 for carbohydrate and lignin contents.

Moreover, two locations per each MCC sample were measured with XPS to determine the surface lignin coverages. When determining the carbohydrate and lignin contents, each parallel sample was again measured twice. These parallel samples, images and locations improved the reliability of the results and decreased the possibility of any random measurement errors prone to experiments without parallel samples. Moreover, most of the results were consistent with the literature improving the reliability of the results even further.

The results of the batch sorption experiments presented in Section 5.7 were also achieved through different measurements and various parallel samples. The same level of reliability as in the structural studies was pursued in these experiments. The experiment 1 had three parallel samples and two individual samples per each MCC, whereas the experiments 2 and 3 had two parallel samples per each MCC. Moreover, the experiments 5 and 8–11 had two to four parallel samples of MCC2. However, the experiments 4, 6 and 7 had only individual MCC2 samples per each pH interval of 1–9, which presents a clear limitation to the reliability of these batch sorption results.

Moreover, high repeatability of the experimental work was achieved by precisely describing each step of each experiment in both structural studies and batch sorption experiments. The production of AaltoCell^{TM} materials, the measurement equipment, the experiment methods, the storage, the equilibrium times and other procedures are explained in this work in detail. Moreover, all intermediate results, equations, tables and uncertainties are presented here to enable repeating the experiments and calculations done in this work.

The availability and the cost of some measurement equipment used in this work, such as XPS and SEM, might limit the repeatability of some experiments, such as determining the surface lignin coverage or surface structure of MCC. On the other hand, most of the experiments and sample pre-treatments were conducted with less expensive and more available measurement equipment, such as the gamma counter, BET-instrument and Stone Polisher.

Since the starting materials, bleached softwood kraft pulp, oxygen delignified softwood pulp and unbleached softwood kraft pulp, were given to use by a Finnish kraft pulp mill without any information of the sampling process, the lack of knowledge on the sampling might limit the repeatability of the sampling as well as reduce the quality of the starting materials and reliability of the results. To overcome these disadvantages, the pulps should be taken from different phases of the same kraft process (Figure 22) by a traceable sampling method and a trained sampler.

In spite of some disadvantages, the experimental work has been carried out by giving high emphasis on reliability and repeatability of the results and experiments. For the reasons mentioned above, the results and experiments have high reliability and repeatability in this work. Thus, this experimental work and all its individual parts should be able to be repeated and achieved similar values and uncertainties as in this work.

5.9 Discussion on the research questions

The experimental work aimed to answer the research questions (Q1–Q3) defined at the beginning of the work. Especially the results of the batch sorption experiments were used to define the ion exchange properties of AaltoCell^{TM} materials in different solutions and with different radionuclides. Since all MCCs were not studied through all the batch sorption experiments, some of the questions were answered only by the experiments conducted on MCC2. However, all research questions could be answered to some extent by the batch sorption experiments done in this work.

The experiments 1–3 were studied with all three MCC samples to show the difference on sorption between different AaltoCell^{TM} materials in phosphate buffer solution (pH ≈ 7). These studies showed a clear increasing trend on sorption order as a function of expected lignin content. The order for the lignin content including both surface lignin and lignin composition was determined to be: MCC2 > MCC3 > MCC1, whereas the sorption order was

confirmed to be: MCC3 > MCC2 > MCC1. Moreover, the experiments 2–3 showed the trends on sorption as a function of time and the effect of the experiment method on swelling. According to these three experiments, the AaltoCell™ materials, MCC2 and MCC3, were suitable for sorption of ^{57}Co in phosphate buffer solution (Q1). Since MCC1 showed close to zero values in Figure 61, it can be stated to be an unsuitable AaltoCell™ material for sorption of ^{57}Co in phosphate buffer solution.

On the other hand, the experiments 7–11 on MCC2 gave more detailed information on the sorption behaviour of MCC2 in various solutions in addition to phosphate buffer solution. The experiments 7–8 were executed in 10 mM $NaNO_3$ (aq), where no significant sorption of ^{57}Co was found, whereas the results of the experiment 9 were consistent with the previous results in phosphate buffer solution. The experiment 10 showed high sorption of ^{57}Co in 0,01 M $NaClO_4$ (aq) (pH ≈ 4,7) and 1 M $NaNO_3$ (aq) (pH ≈ 6,5) and low sorption in 0,1 M $NaClO_4$ (aq) (pH ≈ 4,6). The results of this experiment could be explained by the change in the electrolyte exclusion caused by the Donnan potential. Moreover, the sorption of ^{57}Co increased as the pH increased, and the molarity decreased in the experiment 11. In this experiment no electrolyte exclusion by the Donnan potential was noticed in phosphate buffer solution.

According to these experiments 7–11, the AaltoCell™ material, MCC2, is unsuitable for sorption of ^{57}Co in 10 mM $NaNO_3$ (aq) at any pH level, 0,1–1 M $NaClO_4$ (aq) at pH ~ 4,6 and 0,1 M $NaNO_3$ (aq) at pH ~ 4,8–4,9 (Q1). By contrast, MCC2 is suitable for sorption of ^{57}Co in phosphate buffer solutions at pH ~ 7, especially in those having only Na^+ ions present. It is also suitable for sorption of ^{57}Co in solutions with inert electrolytes and low ionic strength, such as 0,01 M $NaClO_4$ (aq), or active electrolytes and high ionic strength, such as 1 M $NaNO_3$ (aq).

In addition, the results of the experiment 6 suggested that MCC2 might resemble a cation ion exchanger in 10 mM $NaNO_3$ (aq) for ^{85}Sr with oxidation state of +II. This can be detected from the rising curve in Figure 62. Since the experiment 6 was the only experiment done with ^{85}Sr, it can be stated that the AaltoCell™ material, MCC2, is suitable for sorption of ^{85}Sr in 10 mM $NaNO_3$ (aq) at pH range of 1–9 (Q2). By contrast, the experiments 4–5 on ^{134}Cs in 10 mM $NaNO_3$ (aq) gave two very different results. According to the experiment 4 (M3), the sorption of ^{134}Cs declines as pH increases, whereas the experiment 5 (M4) gives no significant sorption on ^{134}Cs at all. Thus, the AaltoCell™ material, MCC2, is not unequivocally suitable for sorption of ^{134}Cs in 10 mM $NaNO_3$ (aq) at pH range of 1–9 (Q3).

The research questions could have been studied in more profound manner, if all the batch experiments would have been done with all three different AaltoCell^{TM} materials, MCC1, MCC2 and MCC3, instead continuing with only MCC2 after the experiment 3. Even continuing with both MCC2 and MCC3 would have given more information on the relations between the sorption of different radionuclides and the lignin content of different AaltoCell^{TM} materials. Also, the experiments 4, 6 and 7 should have been conducted with 2 to 3 parallel samples to improve the reliability of the obtained results.

5.10 Limitations

The main limitations of this work are the insufficient characterization of the AaltoCell^{TM} materials, the dissimilarity of the sorption order and the lignin content order, the lack of individual gravimetric results of sample vials in the experiment 3, the lack of information on the sampling process of the starting materials, the inadequate number of parallel samples in the experiment 4, 6 and 7 as well as the insufficient error analysis and the reduction of uncertainties prior to all experiments. Most of the limitations are related to the planning of the experimental work and identifying the measurement steps causing the major uncertainties affecting on the reliability and repeatability of this work.

The major disadvantage is the lack of profound characterization of the AaltoCell^{TM} materials before and after the batch experiments with, e.g., Fourier transform infrared spectrometer (FTIR), X-ray diffraction (XRD) and ^{13}C cross-polarization magic angle spinning nuclear magnetic resonance (^{13}C CP MAS NMR), as in Liang, Song, Huang, Li and Chen (2013). These methods could have revealed more on the surface properties of AaltoCell^{TM} materials than was achieved with the methods used. Moreover, they could have been used to identify any degradation of the AaltoCell^{TM} materials over time.

Other disadvantages caused by the insufficient planning of the experimental work affect mainly on the quality of the AaltoCell^{TM} materials, the reliability and the repeatability of the obtained results in Figure 62 and the comparability of the results with each other, especially regarding the experiment 3 (M2). Due to the chosen experiment method, the samples were interdependent and not weighted after each sampling, contrary to the other experiment methods. Also, the sampling of these samples was made by pipetting twice 5 ml from the same beaker to the sample vial, which increased the pipetting error of the volume. Moreover, there was some swelling noticed in the M2 graphs in Figure 61. To minimize the differences

between the experiment methods and increase the independency of the samples, this experiment could have been done in a similar way as in M1.

The error analysis and the reduction of uncertainties prior to all experiments would have increased the reliability and the repeatability of some experiments, especially the determination of the carbohydrate and lignin contents with HPAEC-PAD, the surface lignin coverages with XPS and the batch sorption experiments with gamma counter. Their results are somewhat contradictory, since the sorption order for ^{57}Co was: MCC3 > MCC2 > MCC1, whereas the order for lignin content was: MCC2 > MCC3 > MCC1. The reason behind this difference was not revealed in the experiments, which is a clear limitation of the work. There might have been a confusion of MCC2 and MCC3 samples prior to these structural studies, which was not supported by the results of the re-test on the carbohydrate and lignin content. On the other hand, the results of the lignin contents might be correct, if the reason behind the difference in sorption behaviour of the AaltoCell^{TM} materials lies on other structural properties than lignin. This could have been revealed by studying all the AaltoCell^{TM} materials thoroughly in the batch sorption experiments, instead of continuing with MCC2 after the experiment 3.

Moreover, the emphasis on the uncertainties prior to the batch sorption experiments might have decreased the uncertainty values of the results and made the calculations of each parameter´s uncertainty simpler and more straightforward than in this work. This could have been achieved by analyzing the uncertainties of the scales and the pipettes beforehand and deciding the process of each method accordingly. In this work the uncertainty of the scale was 0,0002 g, which was significantly less than the sum of inaccuracy and imprecision of the pipette used for 1-10 ml additions (0,8 %) (Appendix 1). Especially on large volumes, the uncertainty of the pipette overpowers the uncertainty of the scale, which is the reason why each sample should have been weighted after the pH adjustments before centrifugation.

By contrast, some limitations are related to the main object of this work defined in Section 1. The experimental work focused on answering the research questions limited on the suitability of the AaltoCell^{TM} materials for sorption of ^{57}Co, ^{85}Sr and ^{134}Cs. Thus, some experiments were intentionally left out of the scope of this work. Some of these experiments would have been related to the use of real radioactive waste waters produced by NPPs, the different disposal methods, such as incineration and microbial conversion, and the mechanical, heat and radiation resistance of the AaltoCell^{TM} materials.

6 Conclusions

The main objective of this work was to define the suitability of the AaltoCell^{TM} materials as ion exchangers in the purification of the radioactive waste waters produced at NPPs. Instead of real waste waters, traced solutions of $NaNO_3$ (aq), $NaClO_4$ (aq) and phosphate buffers in different molarities were used to define the sorption behaviour of the AaltoCell^{TM} materials on the most important radionuclides, ^{137}Cs, ^{90}Sr and ^{60}Co, in radioactive waste waters. The experimental work was divided into the structural studies and the batch sorption experiments.

The purpose of the structural studies was to provide detailed information on the morphology, specific surface area, particle size and molecular weight distributions, carbohydrate and lignin content and surface lignin coverage of the AaltoCell^{TM} materials and to support the batch sorption experiments. The AaltoCell^{TM} materials, MCC1–MCC3, were produced from bleached sulfate, unbleached oxygen delignified and unbleached pulps in the beginning of the structural studies. On the other hand, the batch sorption experiments were focused on kinetics, sorption as a function of pH and ionic strength and the electrolyte exclusion by the Donnan potential. These experiments were conducted with less hazardous radionuclides, ^{134}Cs, ^{85}Sr and ^{57}Co with half-lives of 2,1 a, 65 d and 272 d.

According to the structural studies, MCC1 had the widest size range of particles and clusters and the smallest values of BET surface area and surface lignin content compared to the other MCCs. On the other hand, it had similar values on molecular weight distribution as MCC2. Although MCC2 had the highest BET surface area, it closely resembled MCC3 on the particle size distribution and the carbohydrate content. Moreover, MCC2 had the highest total lignin and surface lignin contents of all MCCs. The order of the lignin content was noticed to be: MCC2 > MCC3 > MCC1. The results of the batch sorption experiments confirmed the sorption order for ^{57}Co to be: MCC3 > MCC2 > MCC1.

According to the batch sorption experiments, the AaltoCell^{TM} materials, except MCC1, were found to be suitable for sorption of ^{57}Co in phosphate buffer solutions at pH ~ 7 (Q1). Similarly, MCC2 was determined to be suitable in solutions with inert electrolytes and low ionic strength, such as 0,01 M $NaClO_4$ (aq) at pH ~ 4,7 or active electrolytes and high ionic strength, such as 1 M $NaNO_3$ (aq) at pH ~ 6,5. By contrast, MCC2 was detected to be unsuitable in 10 mM $NaNO_3$ (aq) at any pH level tested, 0,1–1 M $NaClO_4$ (aq) at pH ~ 4,6 and

0,1 M $NaNO_3$ (aq) at pH ~ 4,8–4,9. In addition, the sorption of ^{57}Co was discovered to be dependent on the solution, swelling and the experiment method used. Moreover, MCC2 was found to be suitable for sorption of ^{85}Sr in 10 mM $NaNO_3$ (aq) at pH range of 1–9 (Q2) and not consistently suitable for sorption of ^{134}Cs in 10 mM $NaNO_3$ (aq) at the same pH range due to the divergent results of two experiment 4 and 5 (Q3).

Since no research on MCC as an ion exchanger for purification of NPP-based radioactive waste waters was mentioned in literature, this work gave a novel perspective on the production of ion exchange materials from cellulose by the AaltoCell^{TM}-process. It also brought up the potential of the AaltoCell^{TM} materials as ion exchangers in suitable conditions depending on the radionuclide of interest, the solution and the molarity of the solution. The results of the batch sorption experiments indicated that these materials, except MCC1, could have a significant sorption of ^{57}Co in phosphate buffer solutions, especially in those without disturbing K^+ ions. In addition, MCC2 was found to act as a cation exchanger with ^{85}Sr in 10 mM $NaNO_3$ (aq). Since the results were promising, the AaltoCell^{TM} materials containing lignin could be seen as inexpensive, non-toxic and environmentally friendly bases for chemical modifications to achieve better ion exchangers in the nuclear industry and to reduce the volume and the costs of their final disposal.

However, additional research in this field is required before the AaltoCell^{TM} materials can be successfully used in NPPs as ion exchangers. First, chemical modifications and chelating agents or combinations with other ion exchange materials, such as zeolites, leading to better sorption values of these radionuclides and to practical applications should be studied on AaltoCell^{TM} materials. Secondly, the effect of different disposal methods, such as microbial conversion treatment, pyrolysis and incineration, on reducing the volume and the costs of the final disposal of these materials should be studied and compared to the existing procedures. For a more comprehensive study on the relations of the structural properties of the AaltoCell^{TM} materials and their sorption behaviour on different radionuclides in various solutions, more characterization and wider batch sorption experiments should be done in the future.

References

Adams, C., Wang, Y., Loftin, K., & Meyer, M. (2002). Removal of antibiotics from surface and distilled water in conventional water treatment processes. *Journal of Environmental Engineering, 128*(3), 253-260. doi:10.1061/(ASCE)0733-9372(2002)128:3(253)

Akiba, K., Hashimoto, H., & Kanno, T. (1989). Distribution coefficient of cesium and cation exchange capacity of minerals and rocks. *Journal of Nuclear Science and Technology, 26*(12), 1130-1135. doi:10.1080/18811248.1989.9734437

Alén, R. (2000a). Basic chemistry of wood delignification. In P. Stenius, J. Gullichsen & H. Paulapuro (Eds.), *Papermaking Science and Technology, Book 3. Forest Products Chemistry* (pp. 59-104). Jyväskylä: Fabet Oy.

Alén, R. (2000b). Structure and chemical composition of wood. In P. Stenius, J. Gullichsen & H. Paulapuro (Eds.), *Papermaking Science and Technology, Book 3. Forest Products Chemistry* (pp. 12-57). Jyväskylä: Fapet Oy.

Badawy, S. M., Sokker, H. H., Othman, S. H., & Hashem, A. (2005). Cloth filter for recovery of uranium from radioactive waste. *Radiation Physics and Chemistry 73 (2),* 125-130 doi:10.1016/j.radphyschem.2004.08.003

Bang, H., Watanabe, K., Nakashima, R., Kai, W., Song, K., Lee, J. S., . . . Kim, I. (2014). A highly hydrophilic water-insoluble nanofiber composite as an efficient and easily-handleable adsorbent for the rapid adsorption of cesium from radioactive wastewater. *RSC Advances, 4*(103), 59571-59578. doi:10.1039/C4RA09713K

Bang, J., Lee, H., Noh, G. W., Park, J. M., & Yoon, J. K. (2018). Survey result of the counting efficiency of gamma counter by certified reference materials. *Nuclear Medicine and Molecular Imaging, 52*(3), 234-237. doi:10.1007/s13139-018-0515-z

Battista, O. A. (1971). Colloidal polymer microcrystals - new compositions for cosmetics. *Journal of the Society of Cosmetic Chemists, 22*, 561-569.

Battista, O. A., & Smith, P. A. (1962). Microcrystalline cellulose. *Industrial & Engineering Chemistry, 54*(9), 20-29. doi:10.1021/ie50633a003

Beynon, R. (2008). Buffer calculator. Retrieved from https://www.liverpool.ac.uk/pfg/Research/Tools/BuffferCalc/Buffer.html

Bindell, J. B. (1992). SEM: Scanning electron microscopy. In R. C. Brundle, C. A. Evan Jr & S. Wilson (Eds.), *Encyclopedia of materials characterization : Surfaces, interfaces, thin films* (pp. 70-84). United States: Manning Publications Co.

Boerjan, W., Ralph, J., & Baucher, M. (2003). Lignin biosynthesis. *Annual Review of Plant Biology, 54*(1), 519-546. doi:10.1146/annurev.arplant.54.031902.134938

Borrega, M., & Sixta, H. (2013). Purification of cellulosic pulp by hot water extraction. *Cellulose, 20*(6), 2803-2812. doi:10.1007/s10570-013-0086-1

Braunstein, E. L., Dostie, R. L., Germano, K. H., Lamb, S. C., Penet, C. S., & Richards, P. B. (1994). *U.S. Patent No. 5,346,589*. Washington, DC: U.S. Patent and Trademark Office.

Brey, R. R., Butikofer, T., McConnell, J. W., & Rogers, R. D. (1998). Radiocolloids in leachate from the NRC field lysimeter investigations. *Waste Management, 18*(1), 39-53. doi:10.1016/S0956-053X(98)00013-0

Brown, G. N., Bray, L. A., Carlson, C. D., Carson, K. J., DesChane, J. R., Elovich, R. J., . . . Tanaka, P. K. (1996). Comparison of organic and inorganic ion exchangers for removal of cesium and strontium from simulated and actual hanford 241-AW-101 DSSF tank waste (no. PNNL--11120).

Bruggink, C., Wuhrer, M., Koeleman, C. A. M., Barreto, V., Liu, Y., Pohl, C., . . . Deelder, A. M. (2005). Oligosaccharide analysis by capillary-scale high-pH anion-exchange chromatography with on-line ion-trap mass spectrometry. *Journal of Chromatography B*, *829*(1-2), 136-143. doi:10.1016/j.jchromb.2005.10.006

Brunauer, S., Emmett, P. H., & Teller, E. (1938). Adsorption of gases in multimolecular layers. *Journal of the American Chemical Society, 60*(2), 309-319. doi:10.1021/ja0126-9a023

Jollez, P., Chornet, E., & Cloutier, S. (2006). *U.S. Patent No. 6,986,828*. Washington, DC: U.S. Patent and Trademark Office.

Christianson, D. D., Paulis, J. W., & Wall, J. S. (1968). *Ion-exchange chromatography of nucleotides on polyethyleneimine cellulose columns: Analysis of maize grain extracts* doi:10.1016/0003-2697(68)90256-X

Corradini, C., Cavazza, A., & Bignardi, C. (2012). High-performance anion-exchange chromatography coupled with pulsed electrochemical detection as a powerful tool to evaluate carbohydrates of food interest: Principles and applications. *International Journal of Carbohydrate Chemistry, 2012* doi:10.1155/2012/487564

Crist, R. H., Martin, J. R., & Crist, D. R. (2002). Heavy metal uptake by lignin: Comparison of biotic ligand models with an ion-exchange process. *Environmental Science & Technology, 36*(7), 1485-1490. doi:10.1021/es011136f

Dahl, O. P. (2017). Clean technologies. Retrieved from http://bio2.aalto.fi/en/research_groups/clean_technologies/

Dahl, O. P., Vanhatalo, K., & Parviainen, K. (2011). *A novel method to produce microcellulose. Pub. No. WO/2011/154600.* WIPO IP Portal.

Dahl, O. P., Vanhatalo, K., Parviainen, K., & Svedman, M. (2011). *A novel method to produce microcellulose. Pub. No. WO/2011/154601.* WIPO IP Portal.

Demirbas, A. (2004). Adsorption of lead and cadmium ions in aqueous solutions onto modified lignin from alkali glycerol delignication. *Journal of Hazardous Materials, 109*(1-3), 221-226. doi:10.1016/j.jhazmat.2004.04.002

Dobashi, S., Uchida, H., & Ohara, K. (1992). *U.S. Patent No. 5,175,275*. Washington, DC: U.S. Patent and Trademark Office.

Dollimore, D., Spooner, P., & Turner, A. (1976). The BET method of analysis of gas adsorption data and its relevance to the calculation of surface areas. *Surface Technology, 4*(2), 121-160. doi:10.1016/0376-4583(76)90024-8

Dynamic flow method. (2004). In S. Lowell, J. E. Shields, M. A. Thomas & M. Thommes (Eds.), *Characterization of porous solids and powders: Surface area, pore size and density. Particle Technology Series*. Dordrecht: Springer. doi:10.1007/978-1-4020-2303-3_15

Feng, D., Aldrich, C., & Tan, H. (2000). Treatment of acid mine water by use of heavy metal precipitation and ion exchange. *Minerals Engineering, 13*(6), 623-642. doi:10.1016/S0892-6875(00)00045-5

Fischer, H., & Lieser, K. H. (1993). Cellulose exchangers with tailor-made chelating groups for selective separation of uranium. *Fresenius' Journal of Analytical Chemistry, 346*(10-11), 934-942. doi:10.1007/BF00322754

Garg, B. S., Sharma, R. K., Bhojak, N., & Mittal, S. (1999). Chelating resins and their applications in the analysis of trace metal ions. *Microchemical Journal, 61*(2), 94-114. doi:10.1006/mchj.1998.1681

Giordano, N. J. (2013). *College Physics: Reasoning and relationships* (2nd ed.). Brooks/Cole: Cengage Learning.

Greenwood, N. N., & Earnshaw, A. (1997). *Chemistry of the Elements* (2nd ed.) Elsevier.

Griebl, A., Lange, T., Weber, H., Milacher, W., & Sixta, H. (2005). Xylo-oligosaccharide (XOS) formation through hydrothermolysis of xylan derived from viscose process. *Macromolecular Symposia, 232*(1), 107-120. doi:10.1002/masy.200551413

Grubhofer, N. (1991). 1.3 Cellulose Ion Exchangers. In K. Dorfner (Ed.), *Ion Exchangers* (pp. 443-460). New York: Walter de Gruyter.

Guo, X., Zhang, S., & Shan, X. (2008). Adsorption of metal ions on lignin. *Journal of Hazardous Materials, 151*(1), 134-142. doi:10.1016/j.jhazmat.2007.05.065

Havancsák, K. (2017). High-resolution Scanning Electron Microscopy. Retrieved from http://www.technoorg.hu/news-and-events/articles/high-resolution-scanning-electron-microscopy-1/

Helfferich, F. G. (1962). *Ion exchange*. New York: McGraw-Hill.

Hertz, H. (1887). Ueber einen einfluss des ultravioletten lichtes auf die electrische entladung. *Annalen Der Physik, 267*(8), 983-1000. doi:10.1002/andp.18872670827

Himmel, M. E., Ding, S., Johnson, D. K., Adney, W. S., Nimlos, M. R., Brady, J. W., & Foust, T. D. (2007). Biomass recalcitrance: Engineering plants and enzymes for biofuels production. *Science, 315*(5813), 804-807. doi:10.1126/science.1137016

Hokkanen, S., Bhatnagar, A., & Sillanpää, M. (2016). A review on modification methods to cellulose-based adsorbents to improve adsorption capacity. *Water Research, 91*, 156-173. doi:10.1016/j.watres.2016.01.008

Huang, J. H., Kargl-Simard, C., Oliazadeh, M., & Alfantazi, A. M. (2004). pH-controlled precipitation of cobalt and molybdenum from industrial waste effluents of a cobalt electrodeposition process. *Hydrometallurgy, 75*(1-4), 77-90. doi:10.1016/j.hydromet.2004.-06.008

Husgafvel, R., Vanhatalo, K., Rodriguez-Chiang, L., Linkosalmi, L., & Dahl, O. P. (2016). Comparative global warming potential assessment of eight microcrystalline cellulose manufacturing systems. *Journal of Cleaner Production, 126* (Supplement C), 620-629. doi:10.1016/j.jclepro.2016.03.091

Hwang, N., & Barron, A. R. (2011). BET surface area analysis of nanoparticles. *The Connexions project*, 1-11.

Jain, A. K., Siddiqui, M. J., & Singh, R. P. (1979). Solubility of cobalt complex soaps using co^{58} as radiotracer. *Journal of Chemical Technology and Biotechnology, 29*(8), 499-505. doi:10.1002/jctb.503290806

Johansson, L., Campbell, J. M., Koljonen, K., & Stenius, P. (1999). Evaluation of surface lignin on cellulose fibers with XPS. *Applied Surface Science, 144-145*, 92-95. doi:10.1016/S0169-4332(98)00920-9

Johansson, L., & Campbell, J. (2004). Reproducible XPS on biopolymers: Cellulose studies. *Surface and Interface Analysis, 36*(8), 1018-1022. doi:10.1002/sia.1827

Kamel, S. (2005). Preparation of cation-exchange resin from lignin. *International Journal of Polymeric Materials and Polymeric Biomaterials, 55*(4), 283-291. doi:10.1080/00914037390945141

Kautenburger, R., & Beck, H. P. (2010). Influence of geochemical parameters on the sorption and desorption behaviour of europium and gadolinium onto kaolinite. *Journal of Environmental Monitoring, 12*(6), 1295-1301. doi:10.1039/B914861B

Knoll, G. F. (2010). *Radiation detection and measurement* (4th ed.). Hoboken, N.J.: John Wiley.

Koo, O. M. Y., & Heng, P. W. S. (2001). The influence of microcrystalline cellulose grade on shape and shape distributions of pellets produced by extrusion-spheronization. *Chemical and Pharmaceutical Bulletin, 49*(11), 1383-1387. doi:10.1248/cpb.49.1383

Kulbak, M., Gupta, S., Kedem, N., Levine, I., Bendikov, T., Hodes, G., & Cahen, D. (2016). Cesium enhances long-term stability of lead bromide perovskite-based solar cells. *The Journal of Physical Chemistry Letters, 7*(1), 167-172. doi:10.1021/acs.jpclett.5b02597

Kutchko, B. G., & Kim, A. G. (2006). Fly ash characterization by SEM–EDS. *Fuel, 85*(17-18), 2537-2544. doi:10.1016/j.fuel.2006.05.016

Largitte, L., & Pasquier, R. (2016). A review of the kinetics adsorption models and their application to the adsorption of lead by an activated carbon. *Chemical Engineering Research and Design, 109*, 495-504. doi:10.1016/j.cherd.2016.02.006

Lee Black, D., McQuay, M. Q., & Bonin, M. P. (1996). Laser-based techniques for particle-size measurement: A review of sizing methods and their industrial applications. *Progress in Energy and Combustion Science, 22*(3), 267-306. doi:10.1016/S0360-1285(96)00008-1

Lehto, J. (2000). The nuclear industry: Ion exchange. In I. D. Wilson (Ed.), *Encyclopedia of Separation Science* (pp. 3509-3517). Oxford: Academic Press.

Lehto, J., & Hou, X. (2011). *Chemistry and Analysis of Radionuclides: Laboratory techniques and methodology*. Weinheim: Wiley-VCH.

Li, J., Li, Y., Wu, Y., & Zheng, M. (2014). A comparison of biochars from lignin, cellulose and wood as the sorbent to an aromatic pollutant. *Journal of Hazardous Materials, 280*, 450-457. doi:10.1016/j.jhazmat.2014.08.033

Liang, F., Song, Y., Huang, C., Li, Y., & Chen, B. (2013). Synthesis of novel lignin-based ion-exchange resin and its utilization in heavy metals removal. *Industrial & Engineering Chemistry Research, 52*(3), 1267-1274. doi:10.1021/ie301863e

Loebenstein, W. V. (1962). Batch adsorption from solution. *Journal of Research of the National Bureau of Standards – A. Physics and Chemistry, 66A*(6), 503-515.

Luca, C. (2000). Organic ion exchangers. In I. D. Wilson, E. R. Adlard, M. Cooke & C. F. Poole (Eds.), *Encyclopedia of Separation Science* (pp. 1617-1632). Oxford: Academic Press.

The Lund/LBNL nuclear data search. (1999). Retrieved from http://nucleardata.nuclear.lu.se/toi/

Lurie, J. (1975). *Handbook of Analytical Chemistry*. Moscow: MIR Publishers.

Ma, H., Hsiao, B. S., & Chu, B. (2011). Ultrafine cellulose nanofibers as efficient adsorbents for removal of UO_2^{2+} in water. *ACS Macro Letters, 1*(1), 213-216. doi:10.1021/mz2000-47q

Mabrouk, A., Lagneau, V., De Dieuleveult, C., Bachet, M., Schneider, H., & Coquelet, C. (2012). Experiments and modeling of ion exchange resins for nuclear power plants. *International Journal of Engineering and Applied Sciences, 6*(3), 130-134. doi:10.5281/zenodo.1332902

Marinin, D. V., & Brown, G. N. (2000). Studies of sorbent/ion-exchange materials for the removal of radioactive strontium from liquid radioactive waste and high hardness groundwaters. *Waste Management, 20*(7), 545-553. doi:10.1016/S0956-053X(00)00017-9

Marzouki, R., Sayed, M. A., Graia, M., & Zid, M. F. (2019). Cobalt phosphates and applications. *Cobalt Compounds and Applications*. IntechOpen.

Matthews, M. D. (2007). The effect of pretreatment on size analysis. In J. P. M. Syvitski (Ed.), *Principles, Methods and Application of Particle Size Analysis* (pp. 34-42). Cambridge: Cambridge University Press.

McCave, I. N., & Syvitski, J. P. M. (2007). Principles and methods of geological particle size analysis. In J. P. M. Syvitski (Ed.), *Principles, Methods and Application of Particle Size Analysis* (pp. 3-21). Cambridge: Cambridge University Press.

McNaught, A. D., & Wilkinson, A. (1997). *IUPAC. Compendium of Chemical Terminology* (2nd ed.). Oxford: Blackwell Scientific Publications. doi:10.1351/goldbook

Mechelke, M., Herlet, J., Benz, J. P., Schwarz, W. H., Zverlov, V. V., Liebl, W., & Kornberger, P. (2017). HPAEC-PAD for oligosaccharide analysis—novel insights into analyte sensitivity and response stability. *Analytical and Bioanalytical Chemistry, 409*(30), 7169-7181. doi:10.1007/s00216-017-0678-y

Mehta, R. (2012). Interactions, imaging and spectra in SEM. In K. Viacheslav (Ed.), *Scanning Electron Microscopy* (pp. 17-30) Intech.

Mohan, D., Pittman, C. U., & Steele, P. H. (2006). Single, binary and multi-component adsorption of copper and cadmium from aqueous solutions on kraft lignin—a biosorbent. *Journal of Colloid and Interface Science, 297*(2), 489-504. doi:10.1016/j.jcis.2005.11.023

Neeb, K. (1997). *The Radiochemistry of Nuclear Power Plants with Light Water Reactors*. New York: Walter de Gruyter.

Novaes, E., Kirst, M., Chiang, V., Winter-Sederoff, H., & Sederoff, R. (2010). Lignin and biomass: A negative correlation for wood formation and lignin content in trees. *Plant Physiology, 154*(2), 555-561. doi:10.1104/pp.110.161281

O'Connell, D. W., Birkinshaw, C., & O'Dwyer, T. F. (2008). Heavy metal adsorbents prepared from the modification of cellulose: A review. *Bioresource Technology, 99*(15), 6709-6724. doi:10.1016/j.biortech.2008.01.036

Othman, S. H., Sohsah, M. A., & Ghoneim, M. M. (2009). The effects of hazardous ions adsorption on the morphological and chemical properties of reactive cloth filter. *Radiation Physics and Chemistry, 78*(11), 976-985. doi:10.1016/j.radphyschem.2009.06.009

Particle Technology Labs. (2018). BET Surface Area Analysis. Retrieved from https://www.particletechlabs.com/analytical-testing/gas-adsorption-porosimetry-analyses/bet-specific-surface-area

PerkinElmer. (2002). *Wallac 1480 WIZARD 3" gamma counter manual*. Turku: Wallac Oy.

Photonuclear/compton scattering cross section ratio. (2017). Retrieved from http://physicsopenlab.org/2017/10/01/photonuclear-compton-scattering-cross-section-ratio/

Potthast, A., Radosta, S., Saake, B., Lebioda, S., Heinze, T., Henniges, U., . . . Wetzel, H. (2015). Comparison testing of methods for gel permeation chromatography of cellulose: Coming closer to a standard protocol. *Cellulose, 22*(3), 1591-1613. doi:10.1007/s105-70-015-0586-2

Potthast, A., Rosenau, T., Buchner, R., Röder, T., Ebner, G., Bruglachner, H., . . . Kosma, P. (2002). The cellulose solvent system N,N-dimethylacetamide/lithium chloride revisited: The effect of water on physicochemical properties and chemical stability. *Cellulose, 9*(1), 41-53. doi:1015811712657

Reimer, L. (1998). *Scanning Electron Microscopy: Physics of Image Formation and Microanalysis* (2nd ed.). Berlin: Springer-Verlag. doi:10.1007/978-3-540-38967-5

Rocklin, R. D., & Pohl, C. A. (1983). Determination of carbohydrates by anion exchange chromatography with pulsed amperometric detection. *Journal of Liquid Chromatography, 6*(9), 1577-1590. doi:10.1080/01483918308064876

Rohrer, J. S., Basumallick, L., & Hurum, D. (2013). High-performance anion-exchange chromatography with pulsed amperometric detection for carbohydrate analysis of glycoproteins. *Biochemistry (Moscow), 78*(7), 697-709. doi:10.1134/S000629791307-002X

Rønnov-Jenssen, V., & Hansen, J. (1965). The site of absorption of Co^{58}-labeled vitamin B_{12} in man: An investigation made by intestinal intubation with polyethylene glycol as a marker substance. *Blood, 25*(2), 224-230. doi:10.1182/blood.V25.2.224.224

Samat, N., Zulkapli, N., Halim, Z., Ahmad, Z., & Habibah, A. (2015). (2015). Study of mechanical and flammability properties of polypropylene/microcrystalline cellulose composites filled with nano-sized aluminium hydroxide (ATH) particles. Paper presented at the *Advanced Materials Research, , 1115* 402-405.

Sartorius Biohit Liquid Handling Oy. (2013a). *mLINE pipette user manual*. Finland.

Sartorius Biohit Liquid Handling Oy. (2013b). *Picus electronic pipette user manual*. Finland.

Scudder, P. H. (2013). *Electron Flow in Organic Chemistry: A decision-based guide to organic mechanisms*. New York: John Wiley & Sons, Incorporated.

Shlieout, G., Arnold, K., & Müller, G. (2002). Powder and mechanical properties of microcrystalline cellulose with different degrees of polymerization. *Journal of the American Association of Pharmaceutical Scientists, 3*(2), 45-54. doi:10.1208/pt030211

Shweikani, R., Hasan, M., & Takeyeddin, M. (2013). A simplified technique to determine random coincidence summing of gamma rays and dead time count loss corrections. *Applied Radiation and Isotopes, 82*, 72-74. doi:10.1016/j.apradiso.2013.07.036

Sluiter, A., Hames, B., Ruiz, R., Scarlata, C., Sluiter, J., Templeton, D., & Crocker, D. (2008). Determination of structural carbohydrates and lignin in biomass. *Laboratory analytical procedure*, *1617*, 1-16.

Solomon, T. (2001). The definition and unit of ionic strength. *Journal of Chemical Education, 78*(12), 1691. doi:10.1021/ed078p1691

Sonzogni, A. A. (2005). *NuDat 2.0: Nuclear structure and decay data on the internet*. United States: Retrieved from http://www.osti.gov/scitech/biblio/20722626

Srivastava, S. K., Singh, A. K., & Sharma, A. (1994). Studies on the uptake of lead and zinc by lignin obtained from black liquor - a paper industry waste material. *Environmental Technology, 15*(4), 353-361. doi:10.1080/09593339409385438

Staffas, L., Tufvesson, L., Svenfelt, Å, Åström, S., Torén, J., & Arushanyan, Y. (2013). *Alternative sources for products competing with forest based biofuel–A pre-study*. Sweden: F3 The Swedish Knowledge Centre for Renewable Transportation Fuels.

Stenius, P. (2000). Macromolecular, Surface, and Colloid Chemistry. In P. Stenius, J. Gullichsen & H. Paulapuro (Eds.), *Papermaking Science and Technology, Book 3. Forest Products Chemistry* (pp. 173-276). Jyväskylä: Fapet Oy.

Striegel, A. M., Yau, W. W., Kirkland, J. J., & Bly, D. D. (2009). *Modern Size-Exclusion Liquid Chromatography* (2nd ed.). Hoboken, N.J.: John Wile & Sons.

Sun, J., Liu, X., Liang, Y., Wang, L., & Liu, Y. (2017). The preparation of microcrystalline cellulose–nanoSiO_2 hybrid materials and their application in tire tread compounds. *Journal of Applied Polymer Science, 134*(20), 11. doi:10.1002/app.44796

Syvitski, J. P. M. (2007). Introduction. In J. P. M. Syvitski (Ed.), *Principles, Methods and Application of Particle Size Analysis* (pp. 1-2). Cambridge: Cambridge University Press.

Taylor, J. R. (1997). *An Introduction to Error Analysis: The Study of Uncertainties in Physical Measurements* (2nd ed.). Sausalito, CA: University Science Books.

Teollisuuden Voima. (2013). *OL1 and OL2 Nuclear Power Plant Units- technical report*.

Teshirogi, T., & Ohtomo, T. (1986). Preparation of cellulose ion-exchange adsorbents and their bovine serum albumin adsorption capacity. *Sen'i Gakkaishi, 42*(2), T11-T122. doi:10.2115/fiber.42.2_T119

Testova, L., Borrega, M., Tolonen, L. K., Penttilä, P. A., Serimaa, R., Larsson, P. T., & Sixta, H. (2014). Dissolving-grade birch pulps produced under various prehydrolysis intensities: Quality, structure and applications. *Cellulose, 21*(3), 2007-2021. doi:10.1007/s10570-014-0182-x

Testova, L., Chong, S., Tenkanen, M., & Sixta, H. (2011). Autohydrolysis of birch wood. *Holzforschung, 65*(4), 535-542. doi:10.1515/hf.2011.073

ThermoScientific. (2012). *User manual: Finnpipette® F1 single channel variable: fixed volume multichannel*. Finland: Thermo Fisher Scientific.

Tobyn, M. J., McCarthy, G. P., Staniforth, J. N., & Edge, S. (1998). Physicochemical comparison between microcrystalline cellulose and silicified microcrystalline cellulose. *International Journal of Pharmaceutics, 169*(2), 183-194. doi:10.1016/S0378-5173(98)00127-6

Tolonen, L. (2012). *Preparation of cellulose samples for GPC at Aalto University*. Espoo: Aalto University.

Tuason, D. C., Krawczyk, G. R., & Buliga, G. (2010). 12 Microcrystalline Cellulose. In A. Imeson (Ed.), *Food Stabilisers, Thickeners and Gelling Agents*. Wiley-Blackwell.

U.S.NRC. (2017). Transient. Retrieved from https://www.nrc.gov/reading-rm/basic-ref/glossary/transient.html

Van der Heide, P. (2012). *X-ray Photoelectron Spectroscopy: An Introduction to Principles and Practices*. Hoboken, N.J.: John Wiley & Sons.

Vanhatalo, K. (2017). *A new manufacturing process for microcrystalline cellulose (MCC)*

Vanhatalo, K., & Dahl, O. P. (2014). Effect of mild acid hydrolysis parameters on properties of microcrystalline cellulose. *BioResources, 9*(3), 4729-4740. doi:10.15376/biores.9.3.4729-4740

Vanhatalo, K., Lundin, T., Koskimäki, A., Lillandt, M., & Dahl, O. P. (2016). Microcrystalline cellulose property–structure effects in high-pressure fluidization: Microfibril characteristics. *Journal of Materials Science, 51*(12), 6019-6034. doi:10.1007/s10853-016-9907-6

Vanhatalo, K., Maximova, N., Perander, A., Johansson, L., Haimi, E., & Dahl, O. P. (2016). Comparison of conventional and lignin-rich microcrystalline cellulose. *BioResources, 11*(2), 4037-4057. doi:10.15376/biores.11.2.4037-4054

Vanhatalo, K., Parviainen, K., & Dahl, O. P. (2014). Techno-economic analysis of simplified microcrystalline cellulose process. *BioResources, 9*(3), 4741-4755. doi:10.15376/bio-res.9.3.4741-4755

Vasiliu-Oprea, C., & Nicoleanu, J. (1993). Micronized (and microcrystalline) celluloses. obtainment and fields of application. *Polymer-Plastics Technology and Engineering, 32*(3), 181-214. doi:10.1080/03602559308019227

Virtanen, S., Meriläinen, S., Eibl, M., Rabung, T., Lehto, J., & Huittinen, N. (2018). Sorption competition and kinetics of trivalent cations (Eu, Y and Cm) on corundum (α-Al_2O_3): A batch sorption and TRLFS study. *Applied geochemistry*, *92*, 71-81. doi: 10.1016/j.apgeochem.2018.02.011

Vlasselaer, S., D'Olieslager, W., & D'Hont, M. (1976). Caesium ion exchange equilibrium on potassium-zinc-hexacyanoferrate(II) $K_2Zn_3(Fe(CN)_6)_2$. *Journal of Inorganic and Nuclear Chemistry, 38*(2), 327-330. doi:10.1016/0022-1902(76)80419-8

Wang, J., & Wan, Z. (2015). Treatment and disposal of spent radioactive ion-exchange resins produced in the nuclear industry. *Progress in Nuclear Energy, 78*, 47-55. doi:10.1016/j.pnucene.2014.08.003

Webb, J., & Holgate, J. H. (2003). MICROSCOPY | Scanning Electron Microscopy. In B. Caballero (Ed.), *Encyclopedia of Food Sciences and Nutrition (2nd ed.)* (pp. 3922-3928). Oxford: Academic Press.

Wegscheider, W., Knapp, G., & Leyden, D. E. (1981). Preparation of chemically modified cellulose exchangers and their use for the preconcentration of trace elements. *C R C Critical Reviews in Analytical Chemistry, 11*(2), 79-102. doi:10.1080/104083481085-42707

Wu, K., Shen, M., Hu, Y., Xing, W., & Wang, X. (2011). Thermal degradation and intumescent flame retardation of cellulose whisker/epoxy resin composite. *Journal of Thermal Analysis and Calorimetry, 104*(3), 1083-1090. doi:10.1007/s10973-011-1380-5

Wu, Q., Henriksson, M., Liu, X., & Berglund, L. A. (2007). A high strength nanocomposite based on microcrystalline cellulose and polyurethane. *Biomacromolecules, 8*(12), 3687-3692. doi:10.1021/bm701061t

Wu, Y., Zhang, S., Guo, X., & Huang, H. (2008). Adsorption of chromium(III) on lignin. *Bioresource Technology, 99*(16), 7709-7715. doi:10.1016/j.biortech.2008.01.069

Yan, X. (2014). High Performance Liquid Chromatography for Carbohydrate Analysis. In Y. Zou (Ed.), *HPLC Principle, Practices and Procedures* (pp. 1-20) Nova Science.

Yasunari, T. J., Stohl, A., Hayano, R. S., Burkhart, J. F., Eckhardt, S., & Yasunari, T. (2011). Cesium-137 deposition and contamination of Japanese soils due to the Fukushima nuclear accident. *Proceedings of the National Academy of Sciences, 108*(49), 19530-19534. doi:10.1073/pnas.1112058108

Yoon, I., Meng, X., Wang, C., Kim, K., Bang, S., Choe, E., & Lippincott, L. (2009). Perchlorate adsorption and desorption on activated carbon and anion exchange resin. *Journal of Hazardous Materials, 164*(1), 87-94. doi:10.1016/j.jhazmat.2008.07.123

Zakrzewska-Trznadel, G., Harasimowicz, M., & Chmielewski, A. G. (2001). Membrane processes in nuclear technology-application for liquid radioactive waste treatment. *Separation and purification technology*, *22*, 617-625.doi:10.1016/S1383-5866(00)00167-2

Zeiss Sigma VP. (2018). Retrieved from https://www.aalto.fi/en/services/zeiss-sigma-vp

Zhang, Y. P., & Lynd, L. R. (2005). Determination of the number-average degree of polymerization of cellodextrins and cellulose with application to enzymatic hydrolysis. *Biomacromolecules, 6*(3), 1510-1515. doi:10.1021/bm049235j

Zhao, H., Kwak, J. H., Conrad Zhang, Z., Brown, H. M., Arey, B. W., & Holladay, J. E. (2007). Studying cellulose fiber structure by SEM, XRD, NMR and acid hydrolysis. *Carbohydrate Polymers, 68*(2), 235-241. doi:10.1016/j.carbpol.2006.12.013

Zhdanov, B. V., Ehrenreich, T., & Knize, R. J. (2006). Highly efficient optically pumped cesium vapor laser. *Optics Communications, 260*(2), 696-698. doi:10.1016/j.optcom.2005.11.042

Zoumpoulakis, L., & Simitzis, J. (2001). Ion exchange resins from phenol/formaldehyde resin-modified lignin. *Polymer International, 50*(3), 277-283. doi:10.1002/pi.621

Appendices

Appendix 1: The uncertainties of each pipette used in pH adjustments.

Pipette	Test Volume µl	Inaccuracy (%)	Imprecision (%)	Total error (%)
Sartorius Picus 120 µl	120	0,40	0,15	0,55
	60	0,60	0,20	0,80
	12	2,00	1,00	3,00
Sartorius mLINE 0,5-10 µl	10	1,00	0,60	1,60
	5	1,50	1,00	2,50
	1	2,50	1,50	4,00
Finnpipette 100-1000 µl	1000	0,80	0,30	0,11
	100	8,00	3,00	11,00
Finnpipette 5-50 µl	50	1,00	0,40	1,40
	5	10,00	4,00	14,00

The tabled values are taken from the user manuals of Sartorius (2013a; 2013b) and ThermoScientific (2012). The uncertainty of solution volume of the sample (δ_{V_s}) is determined as below:

$$\delta_{V_s} = 0{,}008 \cdot (V_{sol.}) + 0{,}14 \cdot V_{added}, \qquad 20.$$

where $V_{sol.}$ is the volume of the sample before volume addition (V_{added}) caused by pH adjustment, 0,14 is the uncertainty of the added volume (a_i) and 0,008 is the total error (0,8 %) of pipetting of 1 ml, 10 ml or 9 ml with Sartorius 100-1000 µl mLINE or Sartorius 1-10 ml mLINE with inaccuracy of 0,6 % and imprecision of 0,2 %.

Appendix 2: Method indication for each batch experiment from Figure 46.

Experiment	Number	Method
a 3-day batch test: Co-57	1	M1
a 14-day batch experiment: Co-57	2	M1
a 24-h batch experiment: Co-57	3	M2
a sorption vs. pH experiment: Cs-134	4	M3
a re-test on sorption vs. pH experiment: Cs-134	5	M4
a sorption vs. pH experiment: Sr-85	6	M4
a sorption vs. pH experiment: Co-57	7	M4
a re-test on sorption vs. pH experiment: Co-57	8	M3
a re-test with phosphate buffer: Co-57	9	M1
a sorption vs. ionic strength experiment: Co-57	10	M1
a sorption vs. pH experiment with phosphate buffer: Co-57	11	M1

Appendix 3: The measured counting efficiencies for ^{134}Cs, ^{57}Co, and ^{85}Sr.

Sample	Radionuclide	A (Bq)	R (cps)	Efficiencies (%)
1	^{134}Cs	60,44	24,44	40,4
2	^{134}Cs	38,26	15,24	39,8
3	^{57}Co	84,45	73,39	86,9
4	^{57}Co	24,99	21,67	86,7
5	^{85}Sr	714,00	218,83	30,6
6	^{85}Sr	74,70	21,67	29,0

The samples were taken from the different batch experiments, consisting of standard and waste solutions. The volume of each sample was 5 ml. The samples were measured with Wallac 1480 WIZARD 3" gamma counter for count rate (1200 s). Genie 2K and PopTop germanium detectors were used to measure the activity of the samples. The average of three background samples of MilliQ water was 21,5 cpm. This value was subtracted from the count rate values (cpm) of the samples. The counting efficiencies were calculated according to Bang, Lee, Noh, Park and Yoon (2018) with Eq. 21:

$$Counting\ efficiency = \frac{R}{A} \cdot 100\ \%. \qquad 21.$$

The average counting efficiency values for each radionuclide were: 40,1 % for ^{134}Cs, 86,8 % for ^{57}Co, and 29,8 % ^{85}Sr.

Appendix 4: 70x magnification of microcrystalline celluloses: MCC1 (above), MCC2 (middle) and MCC3 (bottom).

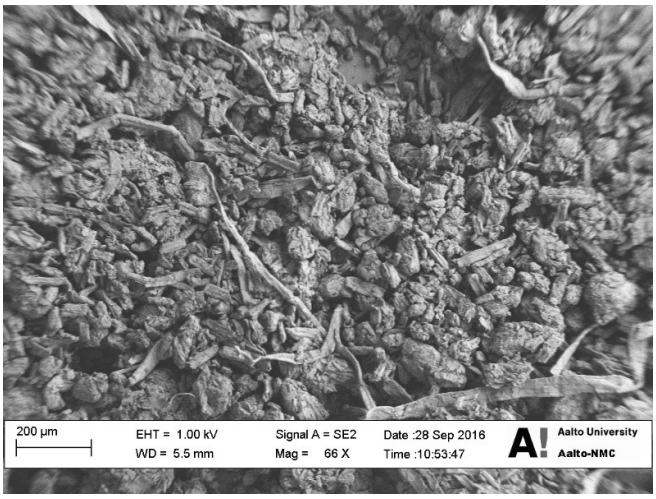

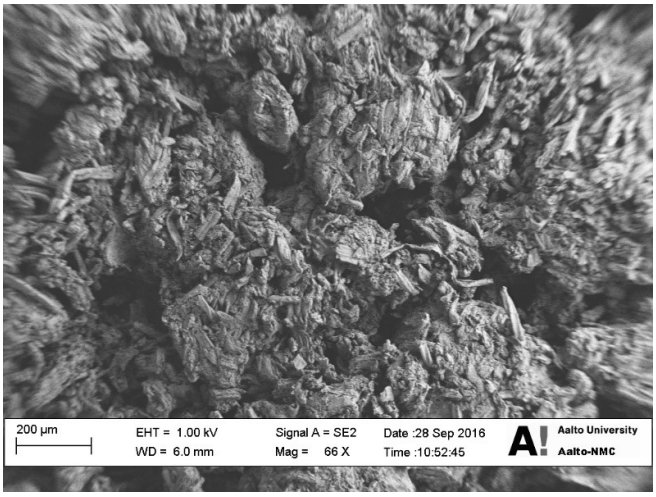

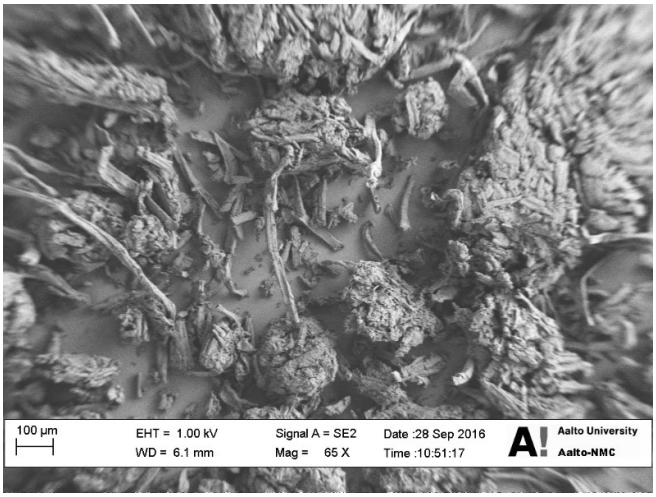

Appendix 5: 250x magnification of microcrystalline celluloses: MCC1 (above), MCC2 (middle) and MCC3 (bottom).

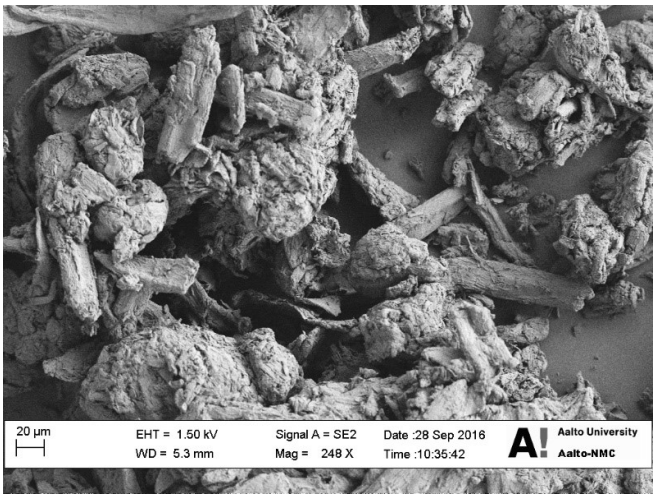

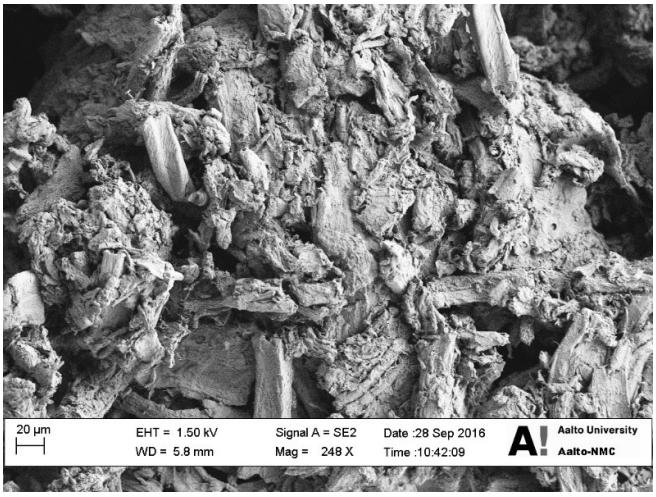

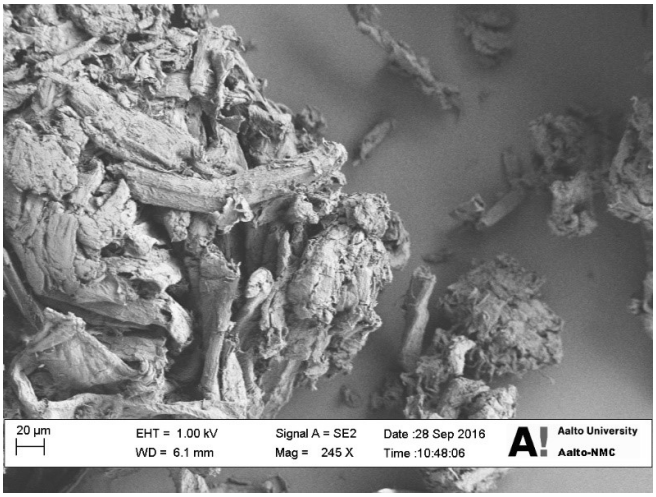

Appendix 6: 1000x magnification of microcrystalline celluloses: MCC1 (above), MCC2 (middle) and MCC3 (bottom).

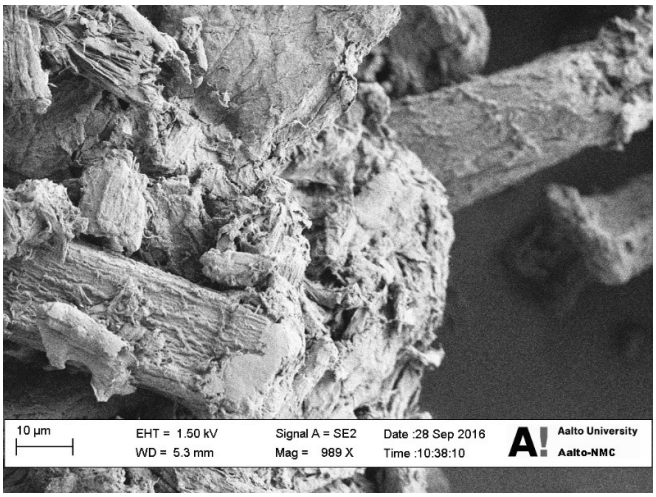

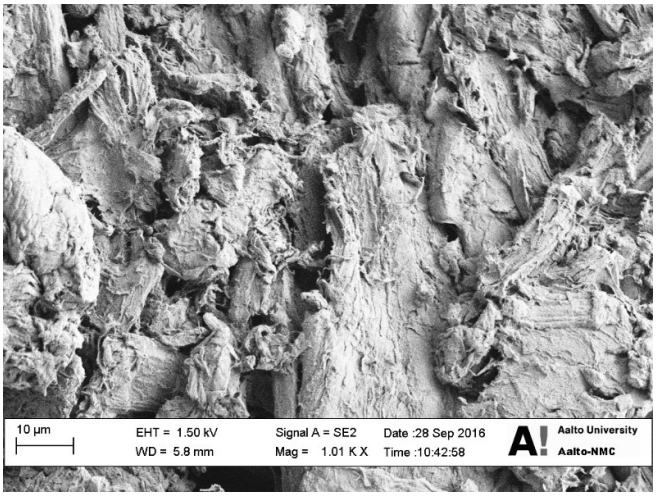

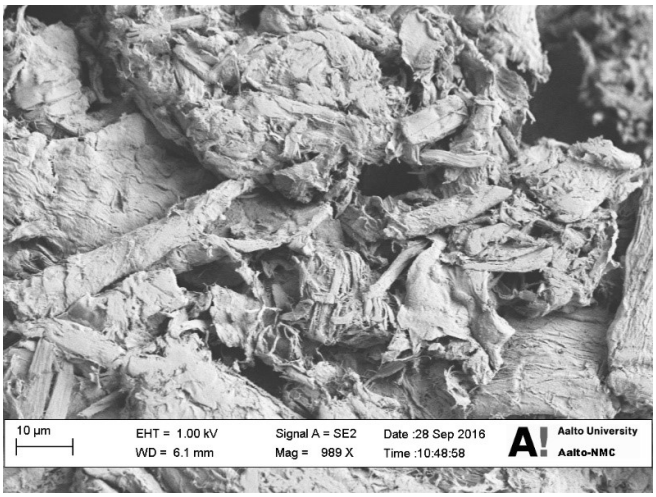

Appendix 7: 3000x magnification of microcrystalline celluloses: MCC1 (above), MCC2 (middle) and MCC3 (bottom).

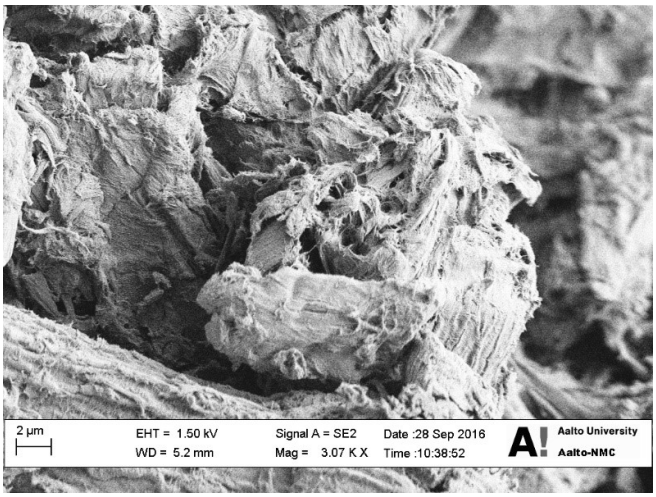

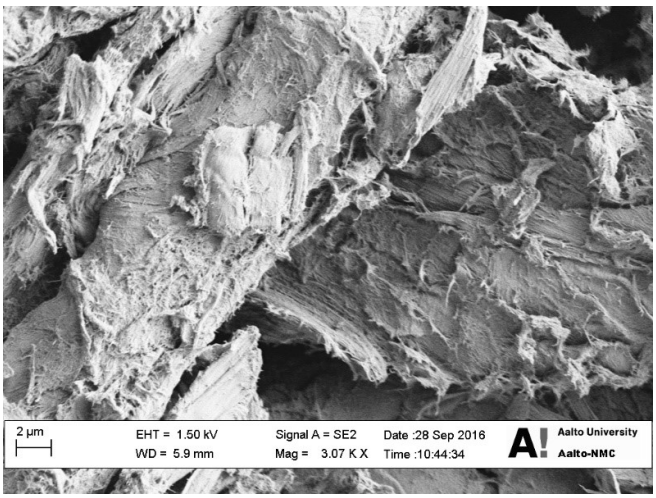

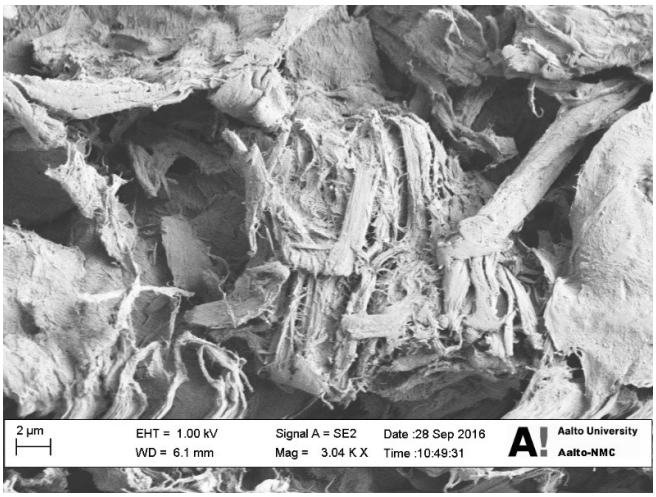

Appendix 8: 10 000x magnification of microcrystalline celluloses: MCC1 (above) and MCC3 (below).

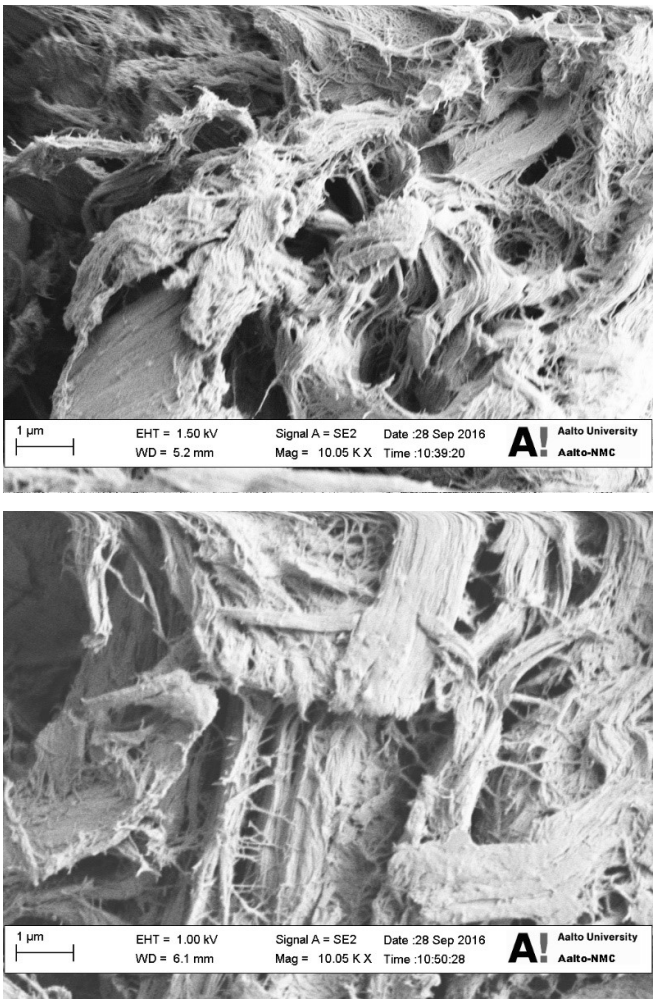

Appendix 9: Original GPC-results.

MCC1:

	Mn	Mw	Mz	Mz+1
	37303,01	138948,83	570323,55	1545224,81
	38113,95	139350,49	508315,8	1155642,39
average	37708	139150	539320	1350434

	DP50	DP100	DP2000	PDI
	0,031682	0,0928951	0,0943038	3,6901423
	0,030691	0,0910106	0,0967693	
average	0,031187	0,0919529	0,0955366	

MCC2:

	Mn	Mw	Mz	Mz+1
	37697,28	138345,89	521675,64	1329889,979
	37136,38	138222,21	512449,05	1283489,936
average	37417	138284	517062	1306690

	DP50	DP100	DP2000	PDI
	0,033243	0,0916503	0,0923575	3,695771201
	0,034131	0,0929765	0,0933791	
average	0,033687	0,0923134	0,0928683	

MCC3:

	Mn	Mw	Mz	Mz+1
	32477,299	98664,769	295313,612	743026,7
	32262,813	97727,61	278457,578	658570,1
average	32370	98196	286886	700798

	DP50	DP100	DP2000	PDI
	0,0408235	0,1080038	0,0480037	3,03355
	0,0414471	0,1083980	0,0475671	
average	0,0411353	0,1082009	0,0477854	

Appendix 10: Carbohydrate results for sample 1 run A (above) and run B (below).

Chromatogram and Results

Injection Details

Injection Name:	**2016-09-07_1087a**	*Run Time (min):*	**45,00**
Vial Number:	**32**	*Injection Volume:*	**20,00**
Injection Type:	**Unknown**	*Channel:*	**ED_1**
Calibration Level:		*Wavelength:*	**n.a.**
Instrument Method:	**Carbs_PA20_45min**	*Bandwidth:*	**n.a.**
Processing Method:	**Basic**	*Dilution Factor:*	**100,0000**
Injection Date/Time:	**07.syys.16 17:59**	*Sample Weight:*	**1,0000**

Chromatogram

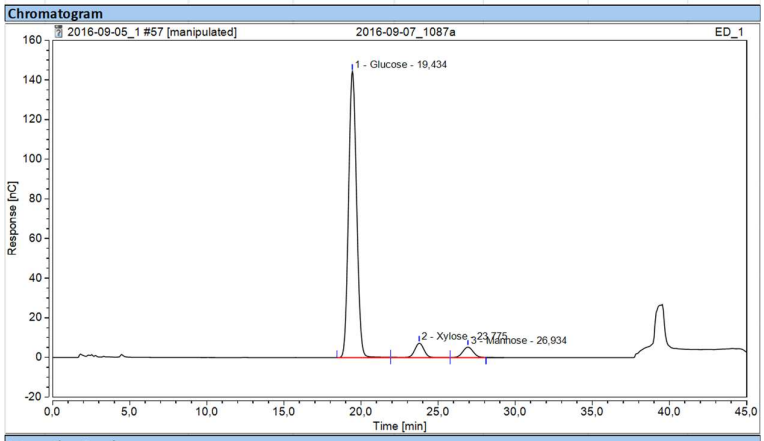

Integration Results

No.	Peak Name	Retention Time min	Area nC*min	Height nC	Relative Area %	Relative Height %	Amount mg/l
n.a.	Fucose	n.a.	n.a.	n.a.	n.a.	n.a.	n.a.
n.a.	Arabinose	n.a.	n.a.	n.a.	n.a.	n.a.	n.a.
n.a.	Rhamnose	n.a.	n.a.	n.a.	n.a.	n.a.	n.a.
n.a.	Galactose	n.a.	n.a.	n.a.	n.a.	n.a.	n.a.
1	Glucose	19,434	87,228	144,527	89,97	91,98	4200,6634
2	Xylose	23,775	5,397	7,290	5,57	4,64	293,9705
3	Mannose	26,934	4,330	5,313	4,47	3,38	273,2430
Total:			**96,954**	**157,130**	**100,00**	**100,00**	

Chromatogram and Results

Injection Details

Injection Name:	**2016-09-07_1087b**	*Run Time (min):*	**45,00**
Vial Number:	**32**	*Injection Volume:*	**20,00**
Injection Type:	**Unknown**	*Channel:*	**ED_1**
Calibration Level:		*Wavelength:*	**n.a.**
Instrument Method:	**Carbs_PA20_45min**	*Bandwidth:*	**n.a.**
Processing Method:	**Basic**	*Dilution Factor:*	**100,0000**
Injection Date/Time:	**07.syys.16 18:47**	*Sample Weight:*	**1,0000**

Chromatogram

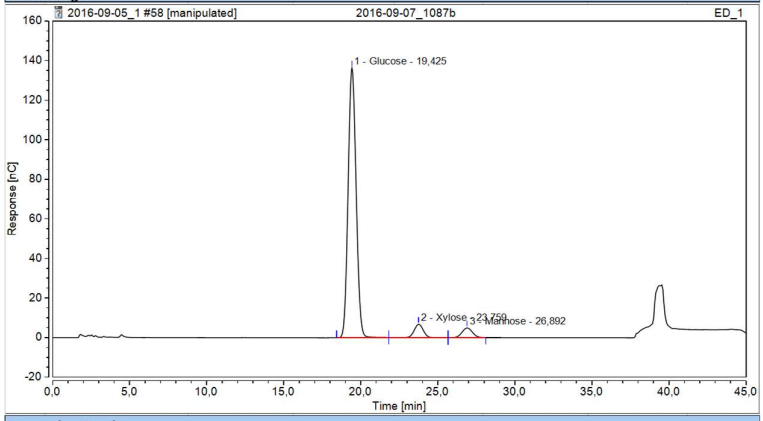

Integration Results

No.	Peak Name	Retention Time min	Area nC*min	Height nC	Relative Area %	Relative Height %	Amount mg/l
n.a.	Fucose	n.a.	n.a.	n.a.	n.a.	n.a.	n.a.
n.a.	Arabinose	n.a.	n.a.	n.a.	n.a.	n.a.	n.a.
n.a.	Rhamnose	n.a.	n.a.	n.a.	n.a.	n.a.	n.a.
n.a.	Galactose	n.a.	n.a.	n.a.	n.a.	n.a.	n.a.
1	Glucose	19,425	82,192	136,405	90,01	92,02	3958,1330
2	Xylose	23,759	5,055	6,852	5,54	4,62	275,3433
3	Mannose	26,892	4,064	4,972	4,45	3,35	256,4557
Total:			**91,310**	**148,230**	**100,00**	**100,00**	

Appendix 11: Carbohydrate results for sample 2 run A (above) and run B (below).

Chromatogram and Results

Injection Details

Injection Name:	**2016-09-07_1088a**	*Run Time (min):*	**45,00**
Vial Number:	**33**	*Injection Volume:*	**20,00**
Injection Type:	**Unknown**	*Channel:*	**ED_1**
Calibration Level:		*Wavelength:*	**n.a.**
Instrument Method:	**Carbs_PA20_45min**	*Bandwidth:*	**n.a.**
Processing Method:	**Basic**	*Dilution Factor:*	**100,0000**
Injection Date/Time:	**07.syys.16 19:35**	*Sample Weight:*	**1,0000**

Chromatogram

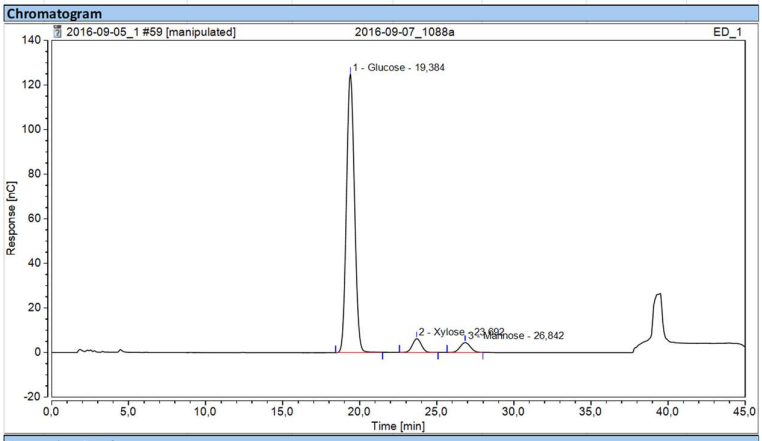

Integration Results

No.	Peak Name	Retention Time min	Area nC*min	Height nC	Relative Area %	Relative Height %	Amount mg/l
n.a.	Fucose	n.a.	n.a.	n.a.	n.a.	n.a.	n.a.
n.a.	Arabinose	n.a.	n.a.	n.a.	n.a.	n.a.	n.a.
n.a.	Rhamnose	n.a.	n.a.	n.a.	n.a.	n.a.	n.a.
n.a.	Galactose	n.a.	n.a.	n.a.	n.a.	n.a.	n.a.
1	Glucose	19,384	75,223	124,880	90,68	92,17	3622,5635
2	Xylose	23,692	4,193	6,148	5,05	4,54	228,4018
3	Mannose	26,842	3,535	4,462	4,26	3,29	223,0889
Total:			**82,952**	**135,491**	**100,00**	**100,00**	

Chromatogram and Results

Injection Details

Injection Name:	**2016-09-07_1088b**	*Run Time (min):*	**45,00**
Vial Number:	**33**	*Injection Volume:*	**20,00**
Injection Type:	**Unknown**	*Channel:*	**ED_1**
Calibration Level:		*Wavelength:*	**n.a.**
Instrument Method:	**Carbs_PA20_45min**	*Bandwidth:*	**n.a.**
Processing Method:	**Basic**	*Dilution Factor:*	**100,0000**
Injection Date/Time:	**07.syys.16 20:23**	*Sample Weight:*	**1,0000**

Chromatogram

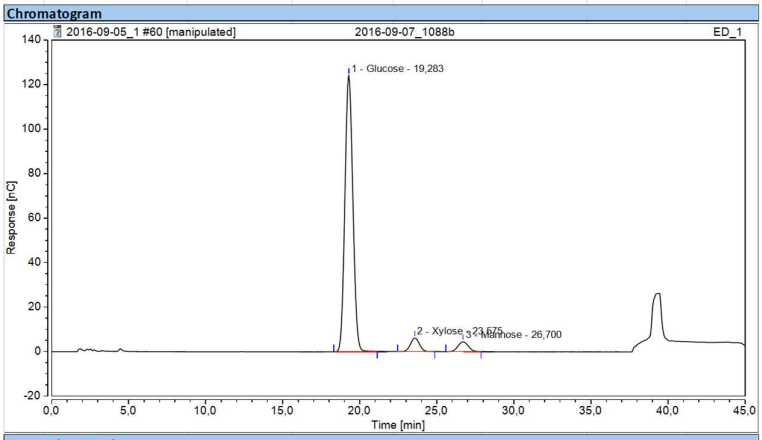

Integration Results

No.	Peak Name	Retention Time min	Area nC*min	Height nC	Relative Area %	Relative Height %	Amount mg/l
n.a.	Fucose	n.a.	n.a.	n.a.	n.a.	n.a.	n.a.
n.a.	Arabinose	n.a.	n.a.	n.a.	n.a.	n.a.	n.a.
n.a.	Rhamnose	n.a.	n.a.	n.a.	n.a.	n.a.	n.a.
n.a.	Galactose	n.a.	n.a.	n.a.	n.a.	n.a.	n.a.
1	Glucose	19,283	74,435	124,153	90,67	92,16	3584,6153
2	Xylose	23,575	4,145	6,113	5,05	4,54	225,7995
3	Mannose	26,700	3,511	4,446	4,28	3,30	221,5630
Total:			**82,092**	**134,711**	**100,00**	**100,00**	

Appendix 12: Carbohydrate results for sample 3 run A (above) and run B (below).

Chromatogram and Results

Injection Details

Injection Name:	**2016-09-07_1089a**	*Run Time (min):*	**45,00**
Vial Number:	**34**	*Injection Volume:*	**20,00**
Injection Type:	**Unknown**	*Channel:*	**ED_1**
Calibration Level:		*Wavelength:*	**n.a.**
Instrument Method:	**Carbs_PA20_45min**	*Bandwidth:*	**n.a.**
Processing Method:	**Basic**	*Dilution Factor:*	**100,0000**
Injection Date/Time:	**07.syys.16 21:12**	*Sample Weight:*	**1,0000**

Chromatogram

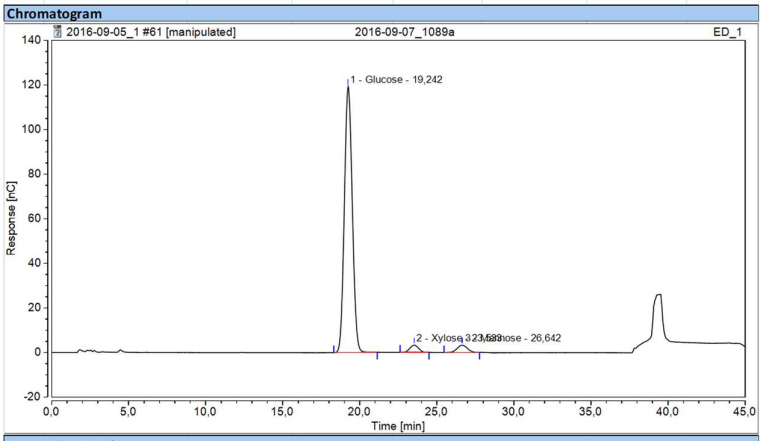

Integration Results

No.	Peak Name	Retention Time min	Area nC*min	Height nC	Relative Area %	Relative Height %	Amount mg/l
n.a.	Fucose	n.a.	n.a.	n.a.	n.a.	n.a.	n.a.
n.a.	Arabinose	n.a.	n.a.	n.a.	n.a.	n.a.	n.a.
n.a.	Rhamnose	n.a.	n.a.	n.a.	n.a.	n.a.	n.a.
n.a.	Galactose	n.a.	n.a.	n.a.	n.a.	n.a.	n.a.
1	Glucose	19,242	71,072	119,366	93,70	94,78	3422,6592
2	Xylose	23,533	2,157	3,258	2,84	2,59	117,4878
3	Mannose	26,642	2,625	3,322	3,46	2,64	165,6550
Total:			**75,854**	**125,947**	**100,00**	**100,00**	

Chromatogram and Results

Injection Details

Injection Name:	**2016-09-07_1089b**	*Run Time (min):*	**45,00**
Vial Number:	**34**	*Injection Volume:*	**20,00**
Injection Type:	**Unknown**	*Channel:*	**ED_1**
Calibration Level:		*Wavelength:*	**n.a.**
Instrument Method:	**Carbs_PA20_45min**	*Bandwidth:*	**n.a.**
Processing Method:	**Basic**	*Dilution Factor:*	**100,0000**
Injection Date/Time:	**07.syys.16 22:00**	*Sample Weight:*	**1,0000**

Chromatogram

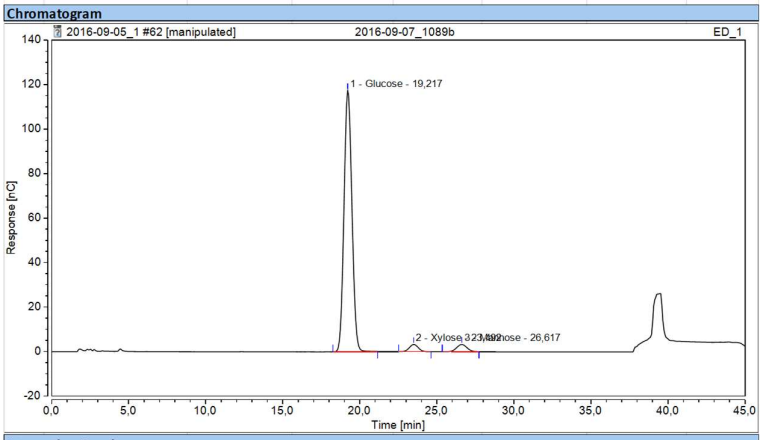

Integration Results

No.	Peak Name	Retention Time min	Area nC*min	Height nC	Relative Area %	Relative Height %	Amount mg/l
n.a.	Fucose	n.a.	n.a.	n.a.	n.a.	n.a.	n.a.
n.a.	Arabinose	n.a.	n.a.	n.a.	n.a.	n.a.	n.a.
n.a.	Rhamnose	n.a.	n.a.	n.a.	n.a.	n.a.	n.a.
n.a.	Galactose	n.a.	n.a.	n.a.	n.a.	n.a.	n.a.
1	Glucose	19,217	70,157	117,474	93,61	94,74	3378,5843
2	Xylose	23,492	2,203	3,245	2,94	2,62	120,0125
3	Mannose	26,617	2,588	3,274	3,45	2,64	163,3417
Total:			**74,949**	**123,994**	**100,00**	**100,00**	

Appendix 13: Carbohydrate results for sample 4 run A (above) and run B (below).

Chromatogram and Results

Injection Details

Injection Name:	**2016-09-07_1090a**	*Run Time (min):*	**45,00**
Vial Number:	**35**	*Injection Volume:*	**20,00**
Injection Type:	**Unknown**	*Channel:*	**ED_1**
Calibration Level:		*Wavelength:*	**n.a.**
Instrument Method:	**Carbs_PA20_45min**	*Bandwidth:*	**n.a.**
Processing Method:	**Basic**	*Dilution Factor:*	**100,0000**
Injection Date/Time:	**07.syys.16 23:07**	*Sample Weight:*	**1,0000**

Chromatogram

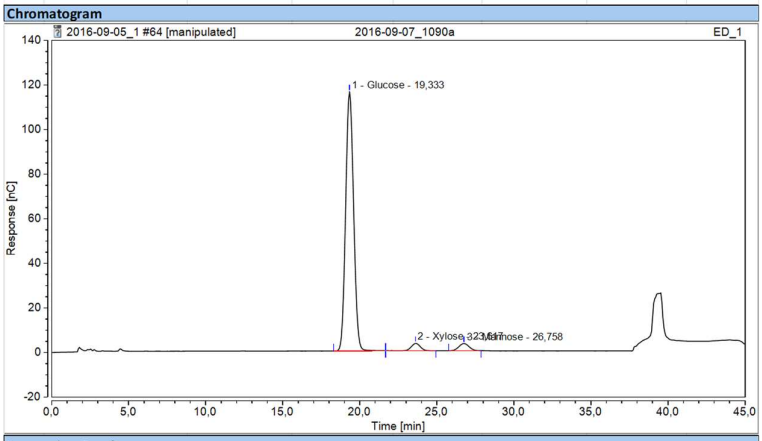

Integration Results

No.	Peak Name	Retention Time min	Area nC*min	Height nC	Relative Area %	Relative Height %	Amount mg/l
n.a.	Fucose	n.a.	n.a.	n.a.	n.a.	n.a.	n.a.
n.a.	Arabinose	n.a.	n.a.	n.a.	n.a.	n.a.	n.a.
n.a.	Rhamnose	n.a.	n.a.	n.a.	n.a.	n.a.	n.a.
n.a.	Galactose	n.a.	n.a.	n.a.	n.a.	n.a.	n.a.
1	Glucose	19,333	69,497	116,123	93,42	94,67	3346,7767
2	Xylose	23,617	2,335	3,295	3,14	2,69	127,2029
3	Mannose	26,758	2,563	3,248	3,44	2,65	161,7294
Total:			**74,395**	**122,665**	**100,00**	**100,00**	

Chromatogram and Results

Injection Details

Injection Name:	**2016-09-07_1090b**	*Run Time (min):*	**45,00**
Vial Number:	**35**	*Injection Volume:*	**20,00**
Injection Type:	**Unknown**	*Channel:*	**ED_1**
Calibration Level:		*Wavelength:*	**n.a.**
Instrument Method:	**Carbs_PA20_45min**	*Bandwidth:*	**n.a.**
Processing Method:	**Basic**	*Dilution Factor:*	**100,0000**
Injection Date/Time:	**07.syys.16 23:56**	*Sample Weight:*	**1,0000**

Chromatogram

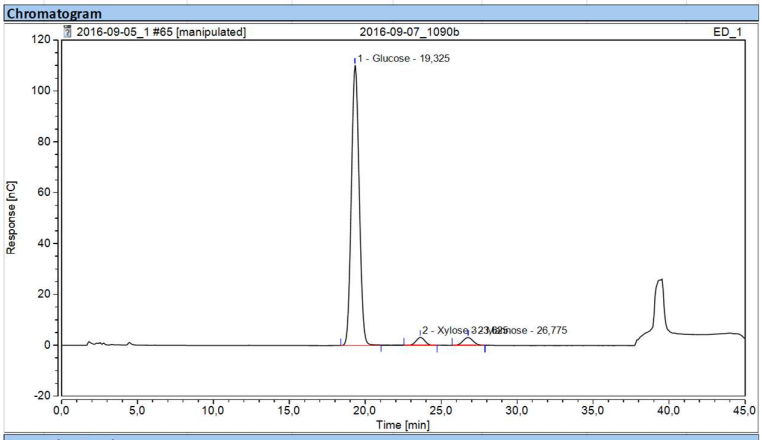

Integration Results

No.	Peak Name	Retention Time min	Area nC*min	Height nC	Relative Area %	Relative Height %	Amount mg/l
n.a.	Fucose	n.a.	n.a.	n.a.	n.a.	n.a.	n.a.
n.a.	Arabinose	n.a.	n.a.	n.a.	n.a.	n.a.	n.a.
n.a.	Rhamnose	n.a.	n.a.	n.a.	n.a.	n.a.	n.a.
n.a.	Galactose	n.a.	n.a.	n.a.	n.a.	n.a.	n.a.
1	Glucose	19,325	65,876	110,131	93,55	94,69	3172,4030
2	Xylose	23,625	2,120	3,108	3,01	2,67	115,4975
3	Mannose	26,775	2,420	3,069	3,44	2,64	152,7035
Total:			**70,416**	**116,307**	**100,00**	**100,00**	

Appendix 14: Carbohydrate results for sample 5 run A (above) and run B (below).

Chromatogram and Results

Injection Details

Injection Name:	**2016-09-07_1091a**	*Run Time (min):*	**45,00**
Vial Number:	**36**	*Injection Volume:*	**20,00**
Injection Type:	**Unknown**	*Channel:*	**ED_1**
Calibration Level:		*Wavelength:*	**n.a.**
Instrument Method:	**Carbs_PA20_45min**	*Bandwidth:*	**n.a.**
Processing Method:	**Basic**	*Dilution Factor:*	**100,0000**
Injection Date/Time:	**08.syys.16 00:44**	*Sample Weight:*	**1,0000**

Chromatogram

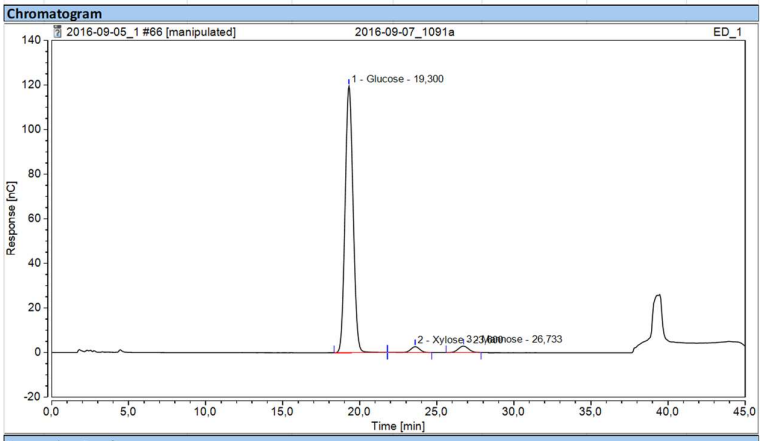

Integration Results

No.	Peak Name	Retention Time min	Area nC*min	Height nC	Relative Area %	Relative Height %	Amount mg/l
n.a.	Fucose	n.a.	n.a.	n.a.	n.a.	n.a.	n.a.
n.a.	Arabinose	n.a.	n.a.	n.a.	n.a.	n.a.	n.a.
n.a.	Rhamnose	n.a.	n.a.	n.a.	n.a.	n.a.	n.a.
n.a.	Galactose	n.a.	n.a.	n.a.	n.a.	n.a.	n.a.
1	Glucose	19,300	71,591	119,558	94,49	95,57	3447,6261
2	Xylose	23,600	1,861	2,633	2,46	2,10	101,3710
3	Mannose	26,733	2,314	2,913	3,05	2,33	146,0488
Total:			**75,766**	**125,104**	**100,00**	**100,00**	

Chromatogram and Results

Injection Details

Injection Name:	**2016-09-07_1091b**	*Run Time (min):*	**45,00**
Vial Number:	**36**	*Injection Volume:*	**20,00**
Injection Type:	**Unknown**	*Channel:*	**ED_1**
Calibration Level:		*Wavelength:*	**n.a.**
Instrument Method:	**Carbs_PA20_45min**	*Bandwidth:*	**n.a.**
Processing Method:	**Basic**	*Dilution Factor:*	**100,0000**
Injection Date/Time:	**08.syys.16 01:32**	*Sample Weight:*	**1,0000**

Chromatogram

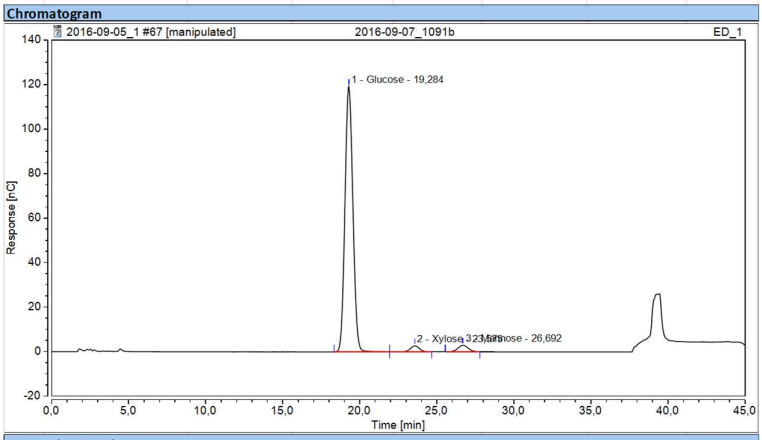

Integration Results

No.	Peak Name	Retention Time min	Area nC*min	Height nC	Relative Area %	Relative Height %	Amount mg/l
n.a.	Fucose	n.a.	n.a.	n.a.	n.a.	n.a.	n.a.
n.a.	Arabinose	n.a.	n.a.	n.a.	n.a.	n.a.	n.a.
n.a.	Rhamnose	n.a.	n.a.	n.a.	n.a.	n.a.	n.a.
n.a.	Galactose	n.a.	n.a.	n.a.	n.a.	n.a.	n.a.
1	Glucose	19,284	71,205	119,334	94,54	95,58	3429,0708
2	Xylose	23,575	1,827	2,620	2,43	2,10	99,4940
3	Mannose	26,692	2,283	2,898	3,03	2,32	144,0611
Total:			**75,315**	**124,852**	**100,00**	**100,00**	

Appendix 15: Carbohydrate results for sample 5 run A (above) and run B (below).

Chromatogram and Results

Injection Details

Injection Name:	**2016-09-07_1092a**	*Run Time (min):*	**45,00**
Vial Number:	**37**	*Injection Volume:*	**20,00**
Injection Type:	**Unknown**	*Channel:*	**ED_1**
Calibration Level:		*Wavelength:*	**n.a.**
Instrument Method:	**Carbs_PA20_45min**	*Bandwidth:*	**n.a.**
Processing Method:	**Basic**	*Dilution Factor:*	**100,0000**
Injection Date/Time:	**08.syys.16 02:21**	*Sample Weight:*	**1,0000**

Chromatogram

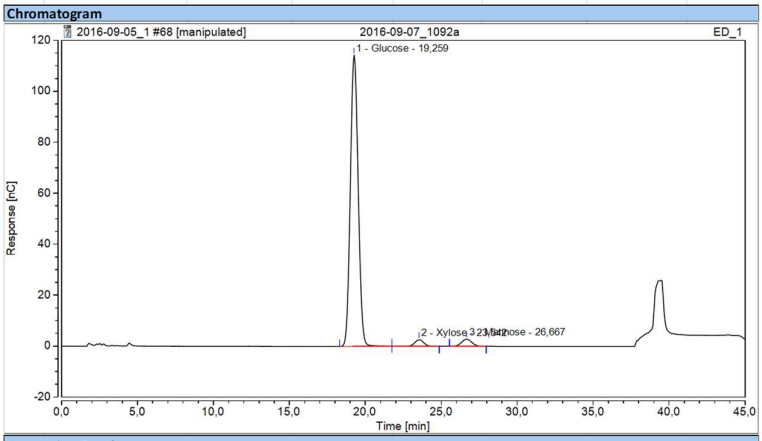

Integration Results

No.	Peak Name	Retention Time min	Area nC*min	Height nC	Relative Area %	Relative Height %	Amount mg/l
n.a.	Fucose	n.a.	n.a.	n.a.	n.a.	n.a.	n.a.
n.a.	Arabinose	n.a.	n.a.	n.a.	n.a.	n.a.	n.a.
n.a.	Rhamnose	n.a.	n.a.	n.a.	n.a.	n.a.	n.a.
n.a.	Galactose	n.a.	n.a.	n.a.	n.a.	n.a.	n.a.
1	Glucose	19,259	68,246	114,217	94,57	95,57	3286,5647
2	Xylose	23,542	1,809	2,540	2,51	2,13	98,5356
3	Mannose	26,667	2,109	2,750	2,92	2,30	133,0803
Total:			**72,164**	**119,507**	**100,00**	**100,00**	

Chromatogram and Results

Injection Details

Injection Name:	**2016-09-07_1092b**	*Run Time (min):*	**45,00**
Vial Number:	**37**	*Injection Volume:*	**20,00**
Injection Type:	**Unknown**	*Channel:*	**ED_1**
Calibration Level:		*Wavelength:*	**n.a.**
Instrument Method:	**Carbs_PA20_45min**	*Bandwidth:*	**n.a.**
Processing Method:	**Basic**	*Dilution Factor:*	**100,0000**
Injection Date/Time:	**08.syys.16 03:09**	*Sample Weight:*	**1,0000**

Chromatogram

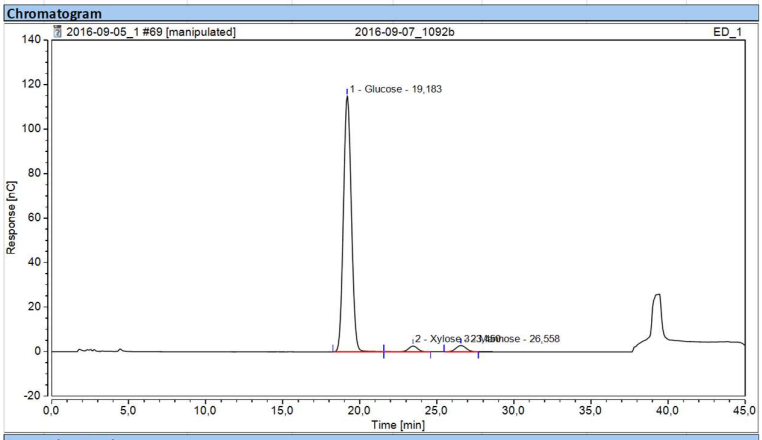

Integration Results

No.	Peak Name	Retention Time min	Area nC*min	Height nC	Relative Area %	Relative Height %	Amount mg/l
n.a.	Fucose	n.a.	n.a.	n.a.	n.a.	n.a.	n.a.
n.a.	Arabinose	n.a.	n.a.	n.a.	n.a.	n.a.	n.a.
n.a.	Rhamnose	n.a.	n.a.	n.a.	n.a.	n.a.	n.a.
n.a.	Galactose	n.a.	n.a.	n.a.	n.a.	n.a.	n.a.
1	Glucose	19,183	68,444	114,905	94,42	95,53	3296,0917
2	Xylose	23,450	1,820	2,559	2,51	2,13	99,1604
3	Mannose	26,558	2,222	2,821	3,06	2,34	140,1973
Total:			**72,486**	**120,285**	**100,00**	**100,00**	

Appendix 16: Carbohydrate results for the standard sample.

Chromatogram and Results

Injection Details

Injection Name:	**2016-09-07_1086b**	*Run Time (min):*	**45,00**
Vial Number:	**31**	*Injection Volume:*	**20,00**
Injection Type:	**Unknown**	*Channel:*	**ED_1**
Calibration Level:		*Wavelength:*	**n.a.**
Instrument Method:	**Carbs_PA20_45min**	*Bandwidth:*	**n.a.**
Processing Method:	**Basic**	*Dilution Factor:*	**100,0000**
Injection Date/Time:	**07.syys.16 17:10**	*Sample Weight:*	**1,0000**

Chromatogram

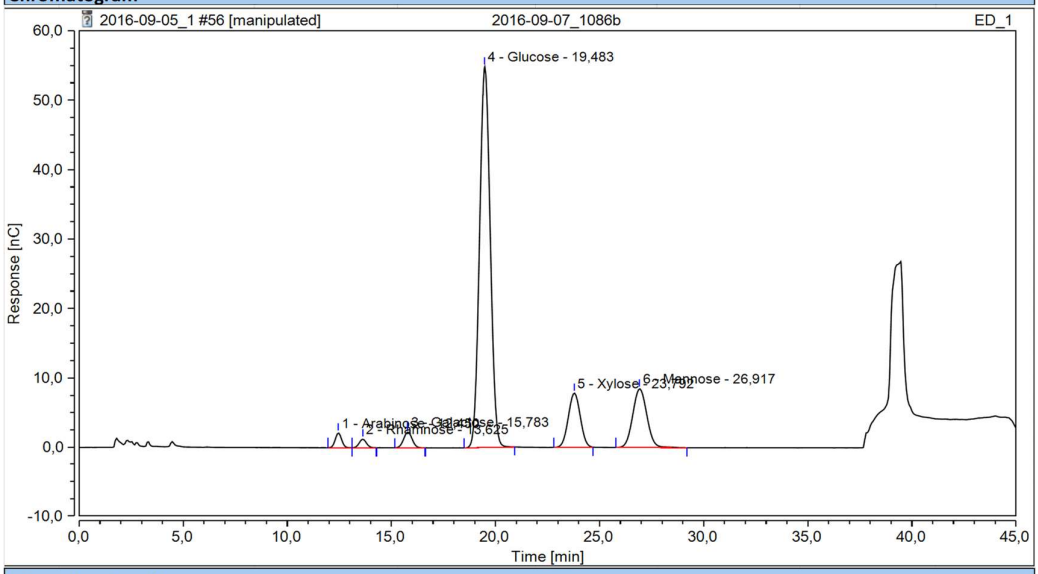

Integration Results

No.	Peak Name	Retention Time min	Area nC*min	Height nC	Relative Area %	Relative Height %	Amount mg/l
n.a.	Fucose	n.a.	n.a.	n.a.	n.a.	n.a.	n.a.
1	Arabinose	12,450	0,761	2,125	1,62	2,77	53,2456
2	Rhamnose	13,625	0,498	1,224	1,06	1,60	52,2751
3	Galactose	15,783	1,075	2,258	2,30	2,94	53,1633
4	Glucose	19,483	32,652	54,851	69,70	71,50	1572,4232
5	Xylose	23,792	5,180	7,795	11,06	10,16	282,1484
6	Mannose	26,917	6,679	8,457	14,26	11,02	421,4597
Total:			**46,844**	**76,710**	**100,00**	**100,00**	

Appendix 17: Determination of sugar compositions of the MCC samples.

Sugar reference	concentration (mg/l)	measured concentration (mg/l)	standard correction
Glucose	1500	1572,423	1,048
Xylose	300	282,148	0,940
Mannose	400	421,460	1,054
Arabinose	50	53,246	1,065
Galactose	50	53,163	1,063
Rhamnose	50	52,275	1,046

Sample 2 runs A and B	concentration (mg/l)	correction ratio	C (corr.) (mg/l)	sugar %
Arabinose	n/a	0,88		
Rhamnose	n/a	0,9		
Galactose	n/a	0,9		
Glucose	3603,589	0,9	3093,853	88,318 %
Xylose	227,101	0,88	212,493	6,066 %
Mannose	222,326	0,9	189,905	5,421 %
Dry mass %	94,97 %		total	99,805 %
Average mass (mg)		319,8		

Sample 3 runs A and B	measured concentration (mg/l)	correction ratio	C (corr.) (mg/l)	sugar %
Arabinose	n/a	0,88		
Rhamnose	n/a	0,9		
Galactose	n/a	0,9		
Glucose	3400,622	0,9	2919,595	83,591 %
Xylose	118,750	0,88	111,112	3,181 %
Mannose	164,498	0,9	140,510	4,023 %
Dry mass %	94,77 %		total	90,795 %
Average mass (mg)		319,5		

Average of samples 5 and 6 runs A and B	measured concentration (mg/l)	correction ratio	C (corr.) (mg/l)	sugar %
Arabinose	n/a	0,88		
Rhamnose	n/a	0,9		
Galactose	n/a	0,9		
Glucose	3364,838	0,9	2888,874	82,774 %
Xylose	99,640	0,88	93,231	2,671 %
Mannose	140,847	0,9	120,308	3,447 %
Dry mass %	94,67 %		total	88,892 %
Average mass (mg)		319,6		

The example calculations for sample 2 are presented in Equations 22 and 23:

$$C(corr.) = \frac{3603{,}5894\ mg/l}{1{,}048} \cdot 0{,}9 = 3093{,}853\ mg/l, \qquad 22.$$

$$sugar\ \% = \frac{3093{,}853 \frac{mg}{l} \cdot 86{,}696\ ml}{1000 \frac{ml}{l} \cdot 319{,}8\ mg \cdot 0{,}9497} * 100\ \% = 88{,}318\ \%, \qquad 23.$$

where 1,048 is the standard correction of glucose in sugar reference determined by comparing the concentration of glucose before and after measurement.

Appendix 18: Determination of lignin compositions of the MCC samples.

MCC	MCC1	MCC1	MCC2	MCC2	MCC3	MCC3
Sample	**1**	**2**	**3**	**4**	**5**	**6**
Amount (mg)	320,50	319,10	319,20	319,80	320,60	318,60
Dry mass (mg)	304,37	303,04	302,52	303,09	303,52	301,63
Crucible (g)	29,08	29,32	29,71	29,50	29,57	29,32
Crucible + Lignin (g)	29,08	29,32	29,73	29,51	29,57	29,32
Klason lignin (mg)	0,60	-1,20	14,20	13,70	2,70	5,40
Klason %	0,197 %	-0,396 %	4,694 %	4,520 %	0,890 %	1,790 %
Average Klason %		-0,099 %		4,607 %		1,340 %
Volume (ml)	86,70	86,70	86,70	86,70	86,70	86,70
Dilution	0,50	0,50	0,50	0,50	0,50	0,50
Absorbance, 205 nm	0,86	0,93	0,88	0,74	0,87	0,89
ASL %	0,111 %	0,121 %	0,115 %	0,096 %	0,113 %	0,116 %
Average ASL %		0,116 %		0,105 %		0,114 %
Total lignin %	0,308 %	-0,275 %	4,808 %	4,616 %	1,003 %	1,907 %
Sum of averages %		0,017 %		4,712 %		1,454 %

The calculations for lignin values of sample 1 are presented in Equations 24 and 25:

$$Klason\ \% = \frac{(29{,}085\ g - 29{,}084\ g)\cdot 1000\ mg/g}{304{,}369\ mg} = 0{,}197\ \%, \qquad 24.$$

$$ASL\ \% = \frac{0{,}086696\ l\cdot 0{,}5\cdot 0{,}859}{0{,}304369\ g\cdot 110\ \frac{g}{l}cm\cdot 1\ cm} = 0{,}111\ \%. \qquad 25.$$

The extinction coefficient of lignin is 110 g/l cm and the cuvette path length is 1 cm. The total lignin % is the sum of Klason % and ASL %.

Appendix 19: The XPS results for MCC1.

[Page 1 of 4] O:\Projects\T10402_Rojas\XPS_data\Vamas\2016\2016-11-17-jenna.vms
Date printed: 12/05/16 11:20:04

wide/14
XPS Spectrum Lens Mode:Hybrid Res:80 Iris(Aper):slot(Slot)
Acqn. Time(s): 599 Sweeps: 2 Anode:Mono(Al (Mono))(100 W) Step(meV): 1000.0
Dwell Time(ms): 272 Charge Neutraliser :On (Current 2.0 A: Balance 3.9 V: Bias 0.7 V) Acquired On :16/11/17 13:27:57
MCC1, p2

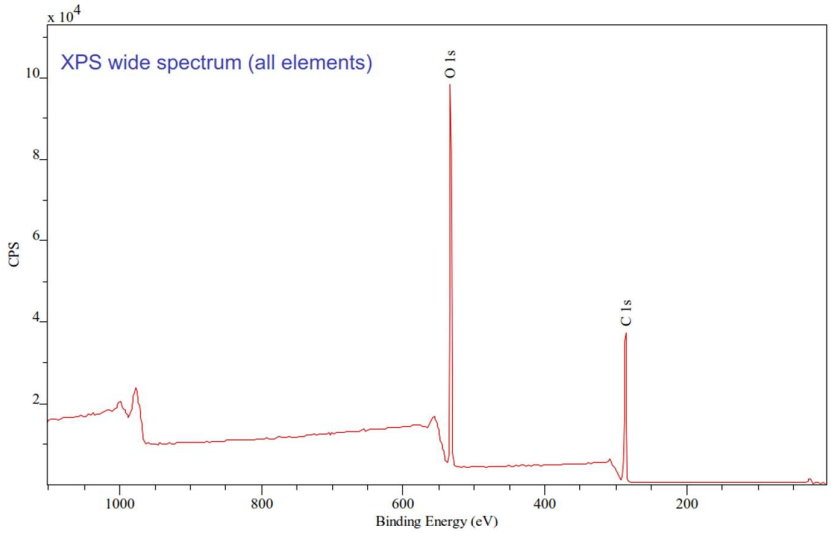

O 1s/12
XPS Spectrum Lens Mode:Hybrid Res:20 Iris(Aper):
Acqn. Time(s): 120 Sweeps: 2 Anode:Mono(Al (M
Dwell Time(ms): 298 Charge Neutraliser :On (Current
MCC1, p2

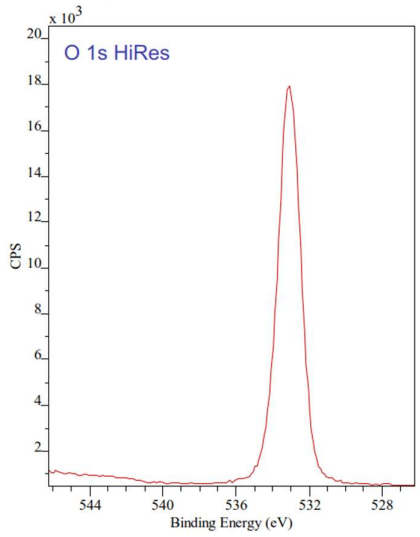

C 1s/13
XPS Spectrum Lens Mode:Hybrid Res:20 Iris(Aper):
Acqn. Time(s): 479 Sweeps: 8 Anode:Mono(Al (M
Dwell Time(ms): 298 Charge Neutraliser :On (Current

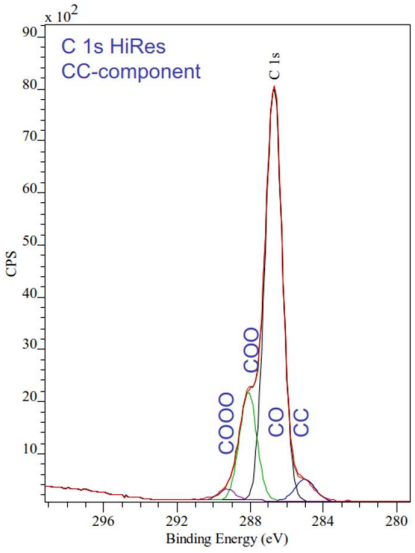

AXIS Ultra and CasaXPS at Aalto PUU

Appendix 20: The XPS results for MCC2.

[Page 2 of 4] O:\Projects\T10402_Rojas\XPS_data\Vamas\2016\2016-11-17-jenna.vms
Date printed: 12/05/16 11:20:04

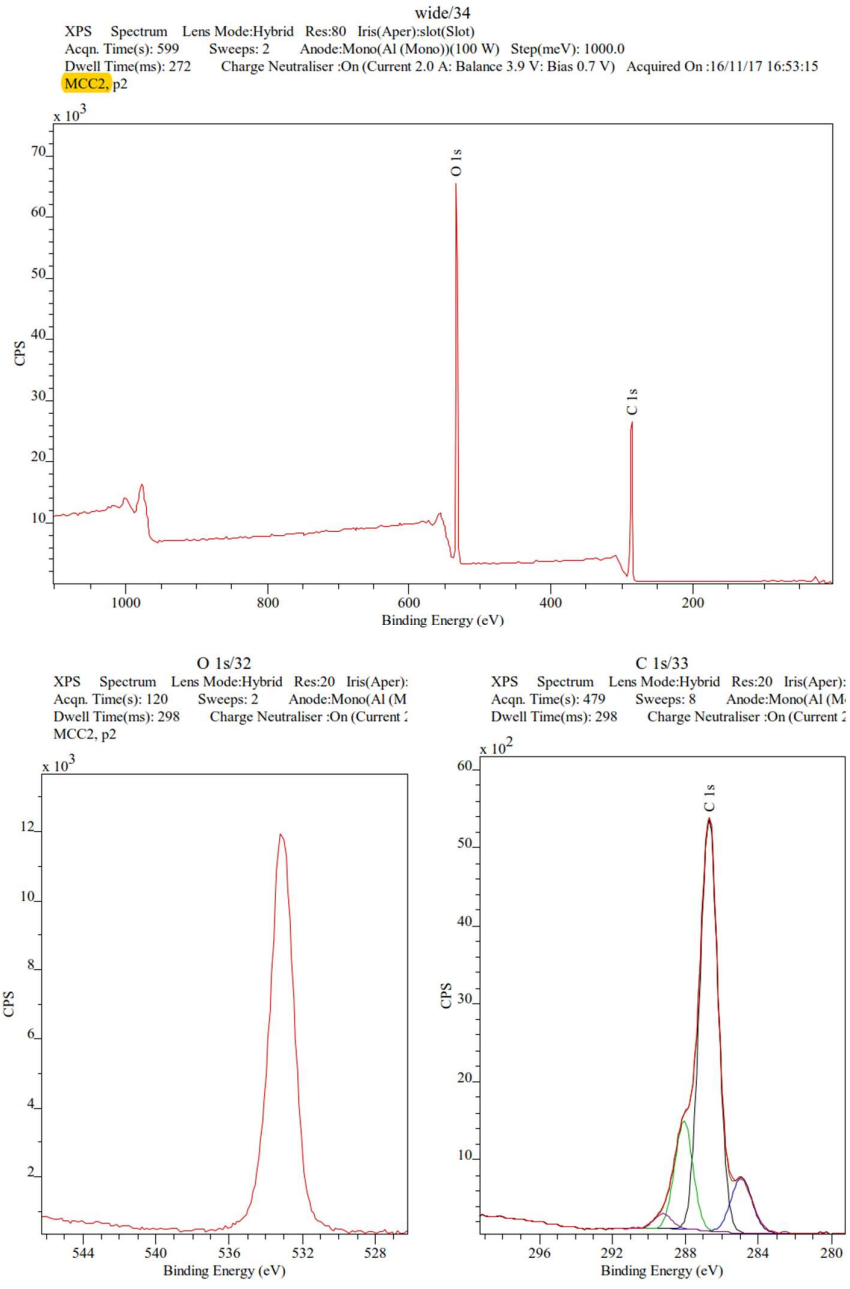

AXIS Ultra and CasaXPS at Aalto PUU

Appendix 21: The XPS results for MCC3.

[Page 3 of 4] O:\Projects\T10402_Rojas\XPS_data\Vamas\2016\2016-11-17-jenna.vms
Date printed: 12/05/16 11:20:04

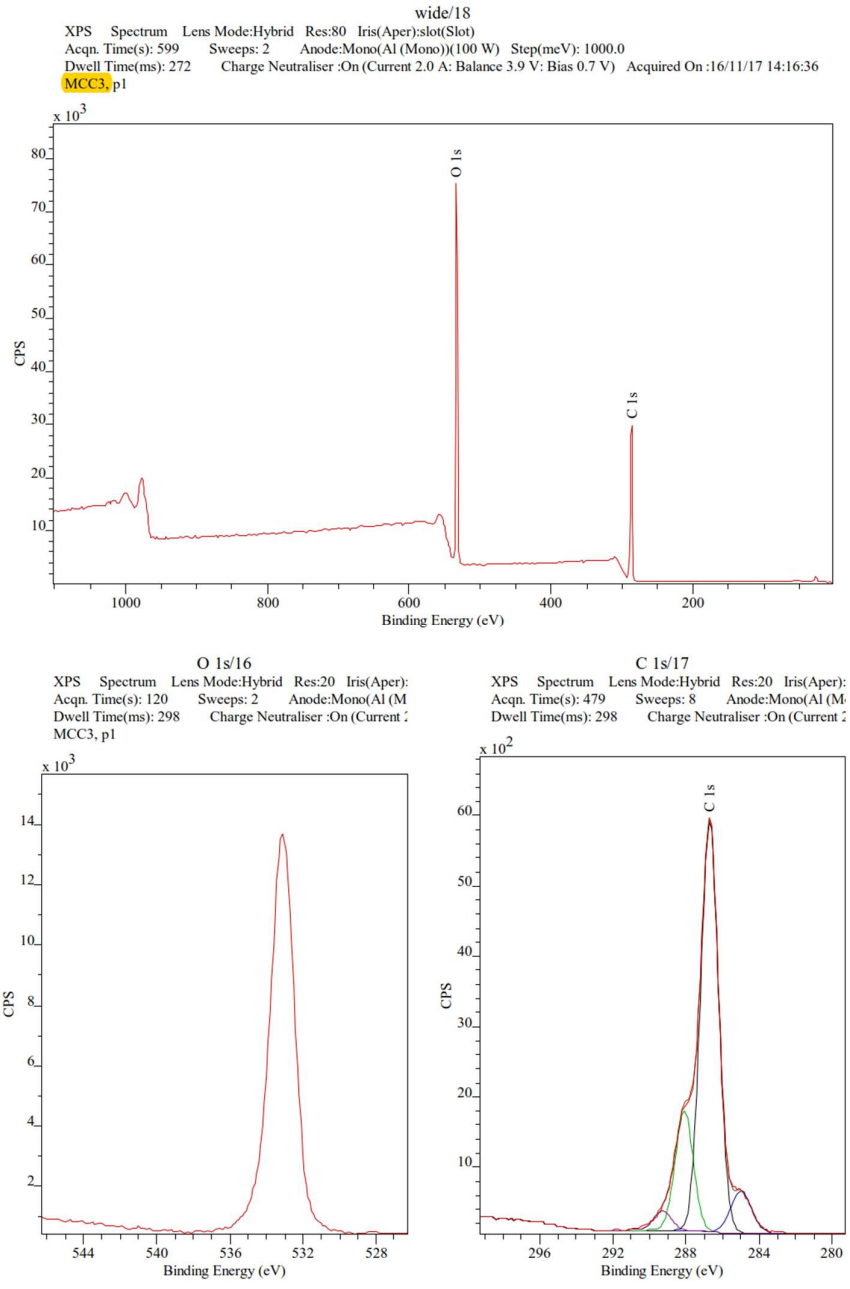

AXIS Ultra and CasaXPS at Aalto PUU

Appendix 22: The XPS results for Whatman paper.

[Page 4 of 4] O:\Projects\T10402_Rojas\XPS_data\Vamas\2016\2016-11-17-jenna.vms
Date printed: 12/05/16 11:20:04

wide/2
XPS Spectrum Lens Mode:Hybrid Res:160 Iris(Aper):slot(Slot)
Acqn. Time(s): 120 Sweeps: 1 Anode:Mono(Al (Mono))(100 W) Step(meV): 1000.0
Dwell Time(ms): 109 Charge Neutraliser :On (Current 2.0 A: Balance 3.9 V: Bias 0.7 V) Acquired On :16/11/17 11:55:57
What

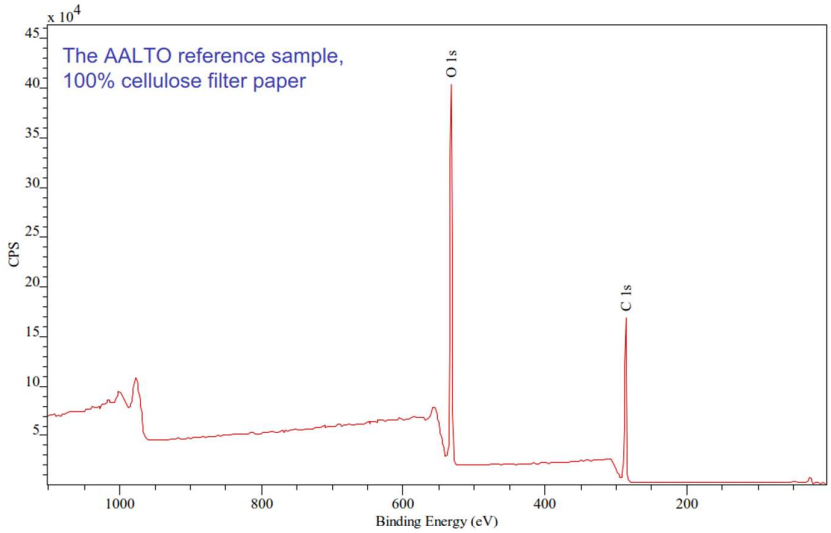

O 1s/3
XPS Spectrum Lens Mode:Hybrid Res:20 Iris(Aper):
Acqn. Time(s): 60 Sweeps: 1 Anode:Mono(Al (Mc
Dwell Time(ms): 298 Charge Neutraliser :On (Current
What

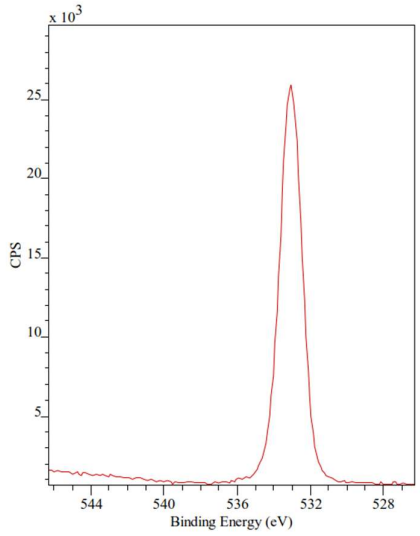

C 1s/4
XPS Spectrum Lens Mode:Hybrid Res:20 Iris(Aper):
Acqn. Time(s): 60 Sweeps: 1 Anode:Mono(Al (Mc
Dwell Time(ms): 298 Charge Neutraliser :On (Current

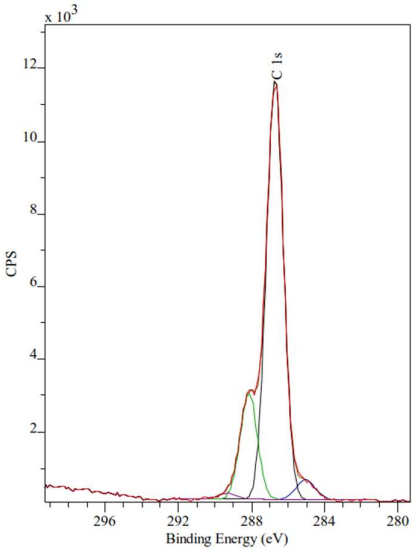

AXIS Ultra and CasaXPS at Aalto PUU

Appendix 23: The wide atomic concentrations of the MCC samples.

MCC	Sample	C 1 s	O 1 s
MCC1	1	60,36 %	39,64 %
MCC1	2	59,26 %	40,74 %
MCC2	1	62,56 %	37,44 %
MCC2	2	62,16 %	37,84 %
MCC3	1	61,21 %	38,79 %
MCC3	2	60,80 %	39,20 %
MCC3 (charged)	3	62,37 %	37,63 %
Whatman	1	59,01 %	40,99 %
Whatman	2	59,33 %	40,67 %

Appendix 24: The atomic concentrations of the functional group components.

MCC	Sample	CC	CO	COO	COOO
MCC1	1	4,67 %	72,35 %	20,57 %	2,41 %
MCC1	2	4,58 %	74,10 %	19,34 %	1,98 %
MCC2	1	10,35 %	68,56 %	18,42 %	2,67 %
MCC2	2	10,68 %	68,77 %	18,00 %	2,55 %
MCC3	1	8,15 %	68,46 %	20,12 %	3,27 %
MCC3	2	7,86 %	71,06 %	18,80 %	2,29 %
MCC3 (charged)	3	7,60 %	64,25 %	21,78 %	6,37 %
Whatman	1	4,24 %	75,60 %	19,08 %	1,08 %
Whatman	2	4,51 %	74,81 %	18,91 %	1,77 %

Appendix 25: Determination of surface lignin content of the MCC samples.

Sample	CC	CC-baseline	Surface lignin	Average
MCC 1	4,67 %	0,43	0,86	
MCC 1	4,58 %	0,34	0,68	0,77
MCC 2	10,35 %	6,11	12,22	
MCC 2	10,68 %	6,44	12,88	12,55
MCC 3	8,15 %	3,91	7,82	
MCC 3	7,86 %	3,62	7,24	7,53
Whatman	4,24 %	**baseline**		

The calculation for surface lignin coverage of MCC1 is presented in Equation 26:

$$Average\ (1.mcc) = \frac{(4{,}67\ \% - 4{,}24\ \%)\cdot 2 + (4{,}58\ \% - 4{,}24\ \%)\cdot 2}{2} \approx 0{,}77, \qquad 26.$$

where the results of CC-baseline are multiplied by 2, since half of lignin´s carbons are presented in the CC-component in the high resolution carbon C 1 s signal. The baseline value was taken from the value of Whatman sample 1, since it had better vacuum conditions than the sample 2.

Appendix 26: Determination of the uncertainty of mass.

		mass	g		
		1. taring	2.taring	3.taring	
	1	3,7142	3,7146	3,7147	
	2	3,7146	3,7145	3,7145	
	3	3,7146	3,7141	3,7146	
	4	3,7143	3,7144	3,7146	
	5	3,7142	3,7145	3,7142	
	6	3,7146	3,7145	3,7143	
	7	3,7142	3,7145	3,7144	
	8	3,7144	3,7145	3,7145	
	9	3,7145	3,7147	3,7141	
	10	3,7144	3,7144	3,7146	
					combined
min		3,7142	3,7141	3,7141	3,7141
max		3,7146	3,7147	3,7147	3,7147
mean		3,7144	3,71447	3,71445	3,71444
stdev		0,000169967	0,000156702	0,000195789	0,0001714
95% confidence interval		0,000333136	0,000307136	0,000383746	0,00033595
99% confidence interval		0,000438516	0,000404291	0,000505136	0,00044222

The uncertainty of the mass on the scale (Sartorius Weighing Technology GmbH) was determined to be 0,0001714 g ≈ 0,0002 g by weighting the same mass ten times.

Appendix 27: Determination of dry masses of the microcrystalline celluloses.

Watch glass empty		times/m (g)		
mcc	1	2	3	
1	33,2822	33,2821	33,2800	
2	38,2937	38,2960	38,2927	
3	37,5377	37,5358	37,5373	
			m (empty)	
	4	5	average from 3-5	
1	33,2806	33,2806	33,2804	
2	38,2938	38,2929	38,2931	
3	37,5370	37,5368	37,5370	
Watch glass full		m(full) wet		
mcc	m (g)	m-m(empty)		
1	38,9473	5,6669		
2	43,2454	4,9523		
3	44,2202	6,6832		
taring times	m1	1.Δm= m-m(empty)	m2	2. Δm= m-m(empty)
1	35,8391	2,5587	35,8436	2,5632
2	40,1583	1,8652	40,1630	1,8699
3	39,3624	1,8254	39,3611	1,8241
			m(full) dry	
	m3	3. Δm= m-m(empty)	average from 1-3. Δm	
1	35,8408	2,5604	2,5608	
2	40,1594	1,8663	1,8671	
3	39,3725	1,8355	1,8283	
	r= (m(full) wet - m(full) dry)/m(full) wet			
mcc	r wet	r dry	r dry %	
1	0,5481	0,4519	45,1881	
2	0,6230	0,3770	37,7019	
3	0,7264	0,2736	27,3568	

Taring times are marked as *m1-m3*. The determination of the dry mass for MCC1 is shown in Eq. 27:

$$r\ (1.mcc)\ dry\ \% = \frac{2{,}5608\ g}{5{,}6669\ g} \cdot 100\ \ \% \ \approx 45{,}19\ \%. \qquad 27.$$

The uncertainties of the dry mass ($\delta r\ dry$) are calculated in Table 8 by using Eq. 13.

Table 8: The uncertainties of the dry mass calculations

Parameter	Function
$m(full)$ $dry\ average$	$\frac{m1+m2+m3}{3} - m(empty)\ average$
$\delta m(full)$ $dry\ average$	$\sqrt{\frac{2}{3}}\delta m$
$m(empty)$ $average$	$\frac{m(3)+m(4)+m(5)}{3}$
$\delta m(empty)$ $average$	$\frac{1}{\sqrt{3}}\delta m$
$m(full)$ wet	$m(g) - m(empty)\ average$
$\delta m(full)$ wet	$\sqrt{\frac{4}{3}}\delta m$
$r\ dry$	$\frac{m(full)\ dry\ average}{m(full)\ wet}$
$\delta r\ dry$	$\delta m \sqrt{\frac{2}{3}\left(\frac{1}{m(full)\ wet}\right)^2 + \frac{4}{3}\left(\frac{m(full)\ dry\ average}{m(full)\ wet^2}\right)^2}$

The parameter δm equals to the same value as the uncertainty of the mass in the scale (0,0002 g) (Appendix 26). According to the equations based on Table 8, the dry masses and their uncertainties are presented on Table 9.

Table 9: The dry masses with uncertainties

MCC	Dry mass content (%)
MCC1	$45 \pm 4 \cdot 10^3$
MCC2	$38 \pm 4 \cdot 10^3$
MCC3	$28 \pm 3 \cdot 10^3$

The uncertainty for each weighted wet microcrystalline cellulose sample can be also derived from Eq.13 as

$$m(mcc) = m \cdot r\ dry,$$
$$\delta m(mcc) = \sqrt{(r\ dry \cdot \delta m)^2 + (m \cdot \delta r\ dry)^2}, \quad 28.$$

where $m(mcc)$ is the weighted MCC mass and $r\ dry$ is the dry mass content of the certain MCC and parameters $\delta m(mcc)$ and $\delta r\ dry$ are their uncertainties, respectively.

Appendix 28: The results of the 3-day pre-test on ^{57}Co.

	Sample masses (wet) (mg)				
Sample	1	2	3	4	5
1.MCC	40,00	39,90	40,00	79,80	200,20
2.MCC	40,01	40,10	39,90	79,80	200,00
3.MCC	39,80	40,10	40,10	79,80	200,20
	Sample masses (dry) (mg)				
Sample	1	2	3	4	5
1.MCC	18,08	18,03	18,08	36,06	90,47
2.MCC	15,08	15,12	15,04	30,09	75,40
3.MCC	10,89	10,97	10,97	21,83	54,77
V(traced solution) = 10 ml					
	cpm				
Sample	1	2	3	4	5
1.MCC	10879,40	10880,70	10838,30	10766,70	10451,10
2.MCC	9917,20	9911,60	9967,40	9234,50	7189,20
3.MCC	8874,70	8873,00	8945,70	7667,90	5505,00
	cpm				
Background			Standards		
1	28,40		1	11025,20	
2	26,70		2	11041,60	
3	27,90				
Background average			Standards average		
27,67			11033,40		
	KD				
Sample	1	2	3	4	5
1.MCC	7,85	7,80	9,98	6,89	6,18
2.MCC	74,82	75,07	71,29	64,94	71,19
3.MCC	224,10	222,64	213,40	201,78	184,29
	logKD				
Sample	1	2	3	4	5
1.MCC	0,89	0,89	1,00	0,84	0,79
2.MCC	1,87	1,88	1,85	1,81	1,85
3.MCC	2,35	2,35	2,33	2,30	2,27
	pH	after equilibrium			
Sample	1	2	3	4	5
1.MCC	6,88	6,86	6,86	6,87	6,85
2.MCC	6,86	6,89	6,87	6,88	6,87
3.MCC	6,81	6,92	6,89	6,89	6,87
The pH of traced solution:			6,81		

Appendix 29: The measurement data of the experiment 2, 3 and 9 for ^{57}Co.

R_s0	R_std0	BF	Kd	d_Kd	t (h)	pH	method	name
176.12	178.22	499.56	5.96	4.48	336.00	7.07	M1	14 d MCC1 sample 1
175.96	178.22	497.74	6.39	4.47	336.00	7.08	M1	14 d MCC1 sample 2
158.59	178.22	498.63	61.73	5.00	336.00	7.09	M1	14 d MCC2 sample 1
157.87	178.22	500.95	64.57	5.05	336.00	7.03	M1	14 d MCC2 sample 2
135.11	178.22	500.03	59.55	6.00	336.00	7.03	M1	14 d MCC3 sample 1
135.38	178.22	500.29	58.35	5.99	336.00	6.97	M1	14 d MCC3 sample 2
183.72	183.64	497.60	-0.23	4.41	24.00	6.98	M1	1 d MCC1 sample 1
184.16	183.64	500.45	-1.43	4.43	24.00	6.96	M1	1 d MCC1 sample 2
168.42	183.64	500.82	45.24	4.86	24.00	6.91	M1	1 d MCC2 sample 1
169.19	183.64	500.35	42.74	4.83	24.00	6.93	M1	1 d MCC2 sample 2
142.08	183.64	499.77	46.17	5.87	24.00	6.93	M1	1 d MCC3 sample 1
139.41	183.64	500.42	158.75	6.01	24.00	6.95	M1	1 d MCC3 sample 2
183.14	184.52	498.51	3.73	4.46	48.00	7.07	M1	2 d MCC1 sample 1
182.27	184.52	501.13	6.16	4.50	48.00	7.10	M1	2 d MCC1 sample 2
167.44	184.52	498.86	50.86	4.90	48.00	7.04	M1	2 d MCC2 sample 1
167.68	184.52	500.09	50.21	4.90	48.00	7.07	M1	2 d MCC2 sample 2
139.22	184.52	500.76	62.92	6.05	48.00	7.05	M1	2 d MCC3 sample 1
141.00	184.52	501.72	54.84	5.98	48.00	7.05	M1	2 d MCC3 sample 2
181.83	184.52	500.85	7.40	4.51	72.00	7.07	M1	3 d MCC1 sample 1
181.31	184.52	500.32	8.84	4.52	72.00	7.07	M1	3 d MCC1 sample 2
165.39	184.52	502.97	58.18	5.01	72.00	7.03	M1	3 d MCC2 sample 1
166.66	184.52	498.00	53.37	4.92	72.00	7.04	M1	3 d MCC2 sample 2
140.03	184.52	501.87	59.43	6.02	72.00	7.02	M1	3 d MCC3 sample 1
139.02	184.52	499.40	63.41	6.05	72.00	7.01	M1	3 d MCC3 sample 2
178.47	182.95	499.86	12.54	4.55	168.00	7.04	M1	7d MCC1 1.sample
179.10	182.95	500.58	10.77	4.54	168.00	7.00	M1	7d MCC1 2.sample
164.06	182.95	501.58	57.74	4.99	168.00	7.06	M1	7d MCC2 1.sample
164.27	182.95	498.17	56.66	4.95	168.00	7.02	M1	7d MCC2 2.sample
137.83	182.95	499.55	63.53	6.05	168.00	7.02	M1	7d MCC3 1.sample
137.83	182.95	500.23	63.77	6.06	168.00	7.01	M1	7d MCC3 2.sample
172.66	173.74	476.07	3.00	4.25	0.08	7.03	M2	5 min MCC1 sample 1
172.22	173.74	476.07	4.21	4.26	0.08	6.98	M2	5 min MCC1 sample 2
171.92	173.74	476.07	5.05	4.27	0.25	6.96	M2	15 min MCC1 sample 1
171.07	173.74	476.07	7.45	4.29	0.25	6.99	M2	15 min MCC1 sample 2
172.03	173.74	476.07	4.73	4.26	0.50	6.99	M2	30 min MCC1 sample 1
171.31	173.74	476.07	6.76	4.28	0.50	6.98	M2	30 min MCC1 sample 2
171.22	173.74	476.07	7.03	4.28	1.00	7.00	M2	1 h MCC1 sample 1
171.80	173.74	476.07	5.38	4.27	1.00	6.98	M2	1 h MCC1 sample 2
171.55	173.74	476.07	6.09	4.28	2.00	7.03	M2	2 h MCC1 sample 1
172.05	173.74	476.07	4.69	4.26	2.00	7.01	M2	2 h MCC1 sample 2
174.70	173.74	476.07	-2.60	4.20	4.00	7.05	M2	4 h MCC1 sample 1
176.11	173.74	476.07	-6.41	4.17	4.00	7.06	M2	4 h MCC1 sample 2
178.45	173.74	476.07	-12.56	4.11	24.00	7.00	M2	24 h MCC1 sample 1

178.59	173.74	476.07	-12.91	4.11	24.00	6.99	M2	24 h MCC1 sample 2
164.01	173.74	475.76	28.23	4.48	0.08	7.00	M2	5 min MCC2 sample 1
164.56	173.74	475.76	26.56	4.46	0.08	6.98	M2	5 min MCC2 sample 2
161.60	173.74	475.76	35.74	4.55	0.25	6.98	M2	15 min MCC2 sample 1
162.02	173.74	475.76	34.42	4.53	0.25	6.98	M2	15 min MCC2 sample 2
160.19	173.74	475.76	40.25	4.59	0.50	6.98	M2	30 min MCC2 sample 1
158.21	173.74	475.76	46.71	4.65	0.50	6.99	M2	30 min MCC2 sample 2
158.05	173.74	475.76	47.26	4.65	1.00	6.98	M2	1 h MCC2 sample 1
157.35	173.74	475.76	49.58	4.68	1.00	7.01	M2	1 h MCC2 sample 2
156.97	173.74	475.76	50.84	4.69	2.00	6.94	M2	2 h MCC2 sample 1
157.07	173.74	475.76	50.52	4.68	2.00	6.96	M2	2 h MCC2 sample 2
160.94	173.74	475.76	37.86	4.57	4.00	6.98	M2	4 h MCC2 sample 1
159.73	173.74	475.76	41.74	4.60	4.00	6.98	M2	4 h MCC2 sample 2
162.85	173.74	475.76	31.84	4.51	24.00	6.98	M2	24 h MCC2 sample 1
164.56	173.74	475.76	26.56	4.46	24.00	6.99	M2	24 h MCC2 sample 2
151.16	173.74	473.03	70.68	4.86	0.08	7.05	M2	5 min MCC3 sample 1
152.65	173.74	473.03	65.35	4.80	0.08	7.03	M2	5 min MCC3 sample 2
140.37	173.74	473.03	12.47	5.27	0.25	7.04	M2	15 min MCC3 sample 1
143.51	173.74	473.03	99.65	5.14	0.25	7.02	M2	15 min MCC3 sample 2
133.75	173.74	473.03	41.43	5.57	0.50	7.00	M2	30 min MCC3 sample 1
135.21	173.74	473.03	34.81	5.50	0.50	7.00	M2	30 min MCC3 sample 2
130.21	173.74	473.03	58.17	5.74	1.00	7.02	M2	1 h MCC3 sample 1
129.42	173.74	473.03	62.03	5.78	1.00	7.02	M2	1 h MCC3 sample 2
129.74	173.74	473.03	60.46	5.76	2.00	6.99	M2	2 h MCC3 sample 1
128.05	173.74	473.03	68.78	5.85	2.00	6.99	M2	2 h MCC3 sample 2
130.98	173.74	473.03	154.42	5.70	4.00	6.96	M2	4 h MCC3 sample 1
131.60	173.74	473.03	151.49	5.67	4.00	6.95	M2	4 h MCC3 sample 2
141.95	173.74	473.03	105.97	5.20	24.00	6.96	M2	24 h MCC3 sample 1
142.40	173.74	473.03	104.11	5.19	24.00	6.97	M2	24 h MCC3 sample 2
20.40	22.58	503.76	53.73	6.28	24.00	6.95	M1	1.sample
20.19	22.58	500.61	59.20	6.32	24.00	6.95	M1	2.sample
20.47	22.58	499.46	51.34	6.20	24.00	6.99	M1	3.sample
20.25	22.58	501.50	57.79	6.31	24.00	6.97	M1	4.sample

Appendix 30: The measurement data of the experiment 4 to 8 with MCC2.

R_s0	R_std0	BF	Kd	d_Kd	t (h)	pH	method	name
4.91	5.95	605.86	128.91	14.26	17.00	0.96	Cs-134 M3	pH 1
5.03	5.95	610.02	111.05	13.79	17.00	1.91	Cs-134 M3	pH 2
5.02	5.95	581.59	107.70	13.06	17.00	2.96	Cs-134 M3	pH 3
5.69	5.95	526.00	23.60	9.78	17.00	4.04	Cs-134 M3	pH 4
5.79	5.95	504.72	13.76	9.17	17.00	4.94	Cs-134 M3	pH 5
5.65	5.95	518.69	27.10	9.73	17.00	6.06	Cs-134 M3	pH 6
6.13	5.95	504.89	-14.93	8.53	17.00	6.46	Cs-134 M3	pH 7
5.47	5.95	537.06	47.00	10.54	17.00	7.15	Cs-134 M3	pH 8
5.61	5.95	506.31	30.73	9.60	17.00	7.31	Cs-134 M3	pH 9
16.62	16.88	502.26	7.76	6.15	20.00	2.02	Cs-134 M4	pH 2 sample 1
16.43	16.88	500.30	13.65	6.21	20.00	2.01	Cs-134 M4	pH 2 sample 2
16.43	16.88	503.91	13.62	6.25	20.00	4.92	Cs-134 M4	pH 5 sample 1
16.38	16.88	503.25	15.18	6.27	20.00	5.11	Cs-134 M4	pH 5 sample 2
16.35	16.88	506.27	16.36	6.32	20.00	7.10	Cs-134 M4	pH 8 sample 1
16.64	16.88	499.74	7.11	6.11	20.00	6.95	Cs-134 M4	pH 8 sample 2
63.75	64.15	509.85	3.18	4.69	20.00	1.04	Sr-85 M4	pH 1
65.34	64.15	500.69	-9.11	4.48	20.00	2.07	Sr-85 M4	pH 2
64.38	64.15	499.41	-1.78	4.54	20.00	2.99	Sr-85 M4	pH 3
63.62	64.15	500.70	4.21	4.62	20.00	4.10	Sr-85 M4	pH 4
62.56	64.15	501.90	12.78	4.71	20.00	4.83	Sr-85 M4	pH 5
58.64	64.15	501.95	47.16	5.07	20.00	5.29	Sr-85 M4	pH 6
46.61	64.15	503.80	189.62	6.80	20.00	6.73	Sr-85 M4	pH 7
30.23	64.15	505.28	567.01	12.00	20.00	7.41	Sr-85 M4	pH 8
27.34	64.15	505.25	680.48	13.83	20.00	7.59	Sr-85 M4	pH 9
19.15	19.47	507.33	8.30	5.94	18.00	1.15	Co-57 M4	pH 1
19.47	19.47	501.26	-0.02	5.76	18.00	2.16	Co-57 M4	pH 2
19.55	19.47	498.03	-2.17	5.70	18.00	3.06	Co-57 M4	pH 3
19.25	19.47	502.05	5.56	5.85	18.00	4.01	Co-57 M4	pH 4
19.44	19.47	498.40	0.73	5.74	18.00	4.97	Co-57 M4	pH 5
19.04	19.47	503.45	11.30	5.94	18.00	5.57	Co-57 M4	pH 6
19.13	19.47	510.73	9.08	5.99	18.00	6.58	Co-57 M4	pH 7
19.11	19.47	499.30	9.43	5.87	18.00	6.93	Co-57 M4	pH 8
19.53	19.47	501.16	-1.63	5.74	18.00	7.38	Co-57 M4	pH 9
19.92	20.76	510.24	21.50	6.05	19.00	6.18	Co-57 M3	pH 7 sample 1
20.47	20.76	507.93	7.24	5.83	19.00	6.49	Co-57 M3	pH 7 sample 2

Appendix 31: The measurement data of the experiment 10 for ^{57}Co with MCC2.

R_s0	R_std0	BF	Kd	d_Kd	t (h)	pH	method	name
22.20	24.55	498.75	52.64	5.21	24.00	6.49	M1	$NaNO_3$ 1 M sample 1
22.42	24.55	497.12	47.23	5.13	24.00	6.52	M1	$NaNO_3$ 1 M sample 2
22.18	24.55	501.52	53.66	5.25	24.00	6.51	M1	$NaNO_3$ 1 M sample 3
24.32	24.55	496.49	4.61	4.62	24.00	4.78	M1	$NaNO_3$ 0.1 M sample 1
24.22	24.55	490.60	6.65	4.59	24.00	4.86	M1	$NaNO_3$ 0.1 M sample 2
24.50	24.55	488.98	0.93	4.51	24.00	4.91	M1	$NaNO_3$ 0.1 M sample 3
23.53	24.55	503.10	21.68	4.88	24.00	4.77	M1	$NaNO_3$ 0.01 M sample 1
23.19	24.55	499.69	29.33	4.94	24.00	4.68	M1	$NaNO_3$ 0.01 M sample 2
23.01	24.55	501.34	33.44	5.00	24.00	4.64	M1	$NaNO_3$ 0.01 M sample 3
22.20	24.55	497.71	52.63	5.20	24.00	4.67	M1	$NaClO_4$ 0.01 M sample 1
22.07	24.55	499.83	56.07	5.27	24.00	4.69	M1	$NaClO_4$ 0.01 M sample 2
22.15	24.55	499.83	54.14	5.24	24.00	4.67	M1	$NaClO_4$ 0.01 M sample 3
24.50	24.55	496.33	1.01	4.58	24.00	4.59	M1	$NaClO_4$ 0.1 M sample 1
24.44	24.55	496.65	2.12	4.60	24.00	4.64	M1	$NaClO_4$ 0.1 M sample 2
24.72	24.55	497.39	-3.55	4.54	24.00	4.62	M1	$NaClO_4$ 0.1 M sample 3
24.51	24.55	497.86	0.76	4.59	24.00	4.57	M1	$NaClO_4$ 1 M sample 1
24.52	24.55	497.68	0.63	4.59	24.00	4.48	M1	$NaClO_4$ 1 M sample 2
24.33	24.55	501.15	4.39	4.66	24.00	4.50	M1	$NaClO_4$ 1 M sample 3

Appendix 32: The measurement data of the experiment 11 for ^{57}Co with MCC2.

R_s0	R_std0	BF	Kd	d_Kd	t (h)	pH	method	name
26.55	26.74	498.19	3.69	5.34	24.00	3.13	M1	1 M pH 3 sample 1
26.52	26.74	496.77	4.15	5.33	24.00	3.12	M1	1 M pH 3 sample 2
26.55	26.74	501.04	3.65	5.37	24.00	3.12	M1	1 M pH 3 sample 3
23.63	23.96	499.07	6.94	5.53	24.00	3.30	M1	0.1 M pH 3 sample 1
23.90	23.96	485.91	1.26	5.31	24.00	3.29	M1	0.1 M pH 3 sample 2
23.79	23.96	495.83	3.52	5.45	24.00	3.30	M1	0.1 M pH 3 sample 3
23.73	24.29	496.47	11.71	5.54	24.00	3.62	M1	0.01 M pH 3 sample 1
23.72	24.29	499.47	12.15	5.58	24.00	3.61	M1	0.01 M pH 3 sample 2
23.76	24.29	491.80	11.01	5.48	24.00	3.61	M1	0.01 M pH 3 sample 3
29.36	31.92	498.19	43.37	5.62	24.00	7.16	M1	1 M pH 7 sample 1
29.75	31.92	471.51	34.38	5.24	24.00	7.16	M1	1 M pH 7 sample 2
29.50	31.92	499.25	40.94	5.60	24.00	7.15	M1	1 M pH 7 sample 3
19.94	23.35	500.15	85.44	6.64	24.00	7.40	M1	0.1 M pH 7 sample 1
20.16	23.35	497.37	78.52	6.51	24.00	7.40	M1	0.1 M pH 7 sample 2
19.89	23.35	482.54	83.83	6.43	24.00	7.40	M1	0.1 M pH 7 sample 3
5.47	27.77	494.87	2017.57	43.68	24.00	7.60	M1	0.01 M pH 7 sample 1
5.30	27.77	496.24	2106.41	45.77	24.00	7.60	M1	0.01 M pH 7 sample 2
5.17	27.77	496.83	2171.04	47.31	24.00	7.60	M1	0.01 M pH 7 sample 3